

AD-780 192

FIREBALL ENTRAINMENT STUDY

David D. Mantrom, et al

TRW Systems Group

Prepared for:

Defense Nuclear Agency
Advanced Research Projects Agency

30 September 1973

DISTRIBUTED BY:

NTIS

National Technical Information Service
U. S. DEPARTMENT OF COMMERCE
5285 Port Royal Road, Springfield Va. 22151

Unclassified

SECURITY CLASSIFICATION OF THIS PAGE (When Data Entered)

AI 780 192

REPORT DOCUMENTATION PAGE		READ INSTRUCTIONS BEFORE COMPLETING FORM
1. REPORT NUMBER DNA 3248F	2. GOVT ACCESSION NO.	3. RECIPIENT'S CATALOG NUMBER
4. TITLE (and Subtitle) Fireball Entrainment Study		5. TYPE OF REPORT & PERIOD COVERED Final Report 18 August 1971-30 September 1973
		6. PERFORMING ORG. REPORT NUMBER 18895-6004-RU-00
7. AUTHOR(s) David D. Mantrom and Wayne W. Haigh		8. CONTRACT OR GRANT NUMBER(s) DNA001-72-C-0019
9. PERFORMING ORGANIZATION NAME AND ADDRESS TRW Systems Group One Space Park Redondo Beach, California 90278		10. PROGRAM ELEMENT PROJECT, TASK AREA & WORK UNIT NUMBERS ARPA Order No. 1433 Subtask No. ZL433 Work Unit No. 08
11. CONTROLLING OFFICE NAME AND ADDRESS Director Defense Advanced Research Projects Agency Washington, D. C. 20301		12. REPORT DATE 30 September 1973
		13. NUMBER OF PAGES XX 111
14. MONITORING AGENCY NAME & ADDRESS (if different from Controlling Office) Director Defense Nuclear Agency Washington, D. C. 20305		15. SECURITY CLASS (of this report) Unclassified
		15a. DECLASSIFICATION DOWNGRADING SCHEDULE
16. DISTRIBUTION STATEMENT (of this Report) Approved for public release; distribution unlimited.		
17. DISTRIBUTION STATEMENT (of the abstract entered in Block 20, if different from Report)		
18. SUPPLEMENTARY NOTES This work was supported by the Defense Nuclear Agency under Subtask HC061-08.		
19. KEY WORDS (Continue on reverse side if necessary and identify by block number) Entrainment Fireballs Turbulent Mixing Holographic Interferometry Vortex Flow Reproduced by NATIONAL TECHNICAL INFORMATION SERVICE U S Department of Commerce Springfield VA 22151		
20. ABSTRACT (Continue on reverse side if necessary and identify by block number) An experimental program to study the development and entrainment processes of fireballs is described. The high pressure test facility and diagnostic equipment developed for this subscale laboratory study are discussed. Data acquisition, interpretation, and reduction techniques are outlined. Turbulent and laminar mean size/rise data and particle tracking photographs are compared and results reflect marked differences between these two flow regimes. Properly scaled turbulent dimensional data compare favorably with those of a low yield, low altitude nuclear event. Averaged mass concentration results obtained from		

DD FORM 1 JAN 73 1473

EDITION OF 1 NOV 55 IS OBSOLETE

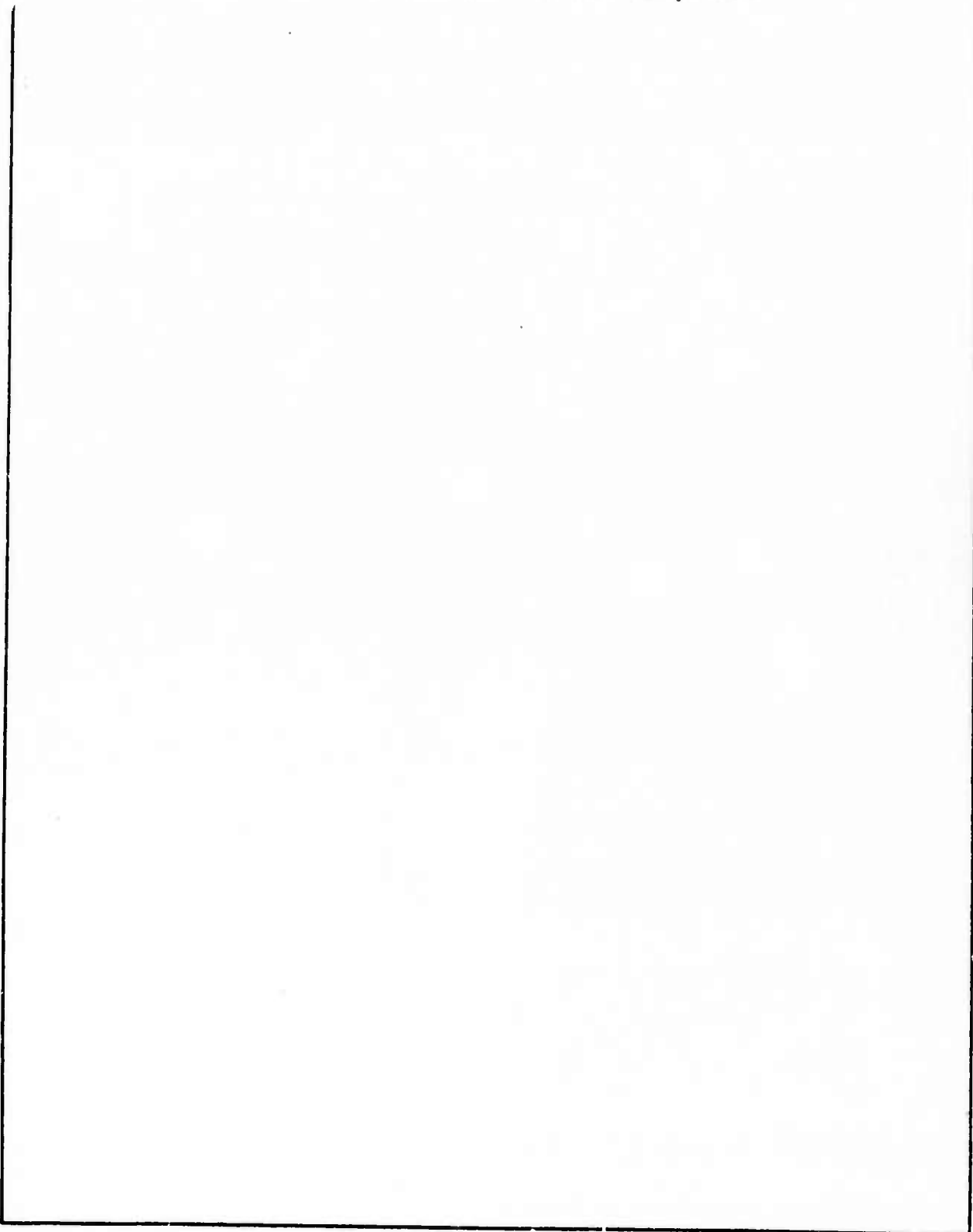
Unclassified

SECURITY CLASSIFICATION OF THIS PAGE (When Data Entered)

Unclassified

SECURITY CLASSIFICATION OF THIS PAGE(When Data Entered)

holographic interferometry data for a range of Reynolds numbers and rise positions are discussed. These profiles are shown to remain geometrically similar after torus formation has occurred. One particular set of turbulent interferometry data was extensively analyzed and a composite iso-concentration picture constructed. This figure provides a complete spatial distribution of the concentration of the low density gas in a laboratory event.



Unclassified

SECURITY CLASSIFICATION OF THIS PAGE(When Data Entered)

FOREWORD

This research was supported by the Advanced Research Projects Agency and was monitored by the Defense Nuclear Agency, under ARPA Order No. 1433 and Contract DNA001-72-C-0019.

The views and conclusions contained in this document are those of the authors and should not be interpreted as necessarily representing the official policies, either expressed or implied, of the Advanced Research Projects Agency or the U. S. Government.

ACKNOWLEDGEMENTS

The authors are deeply indebted to Mr. Ken Beach of TRW and to Dr. John Lewis of Techmate, Inc. for their valuable contributions throughout the entirety of the study. To Mr. Beach go many thanks for his creative thoughts and boundless energy during the facility development and data acquisition phases of the experiment. Dr. Lewis conceived the original idea for the experiment, and his many stimulating and helpful discussions during its execution were greatly appreciated.

TABLE OF CONTENTS

	Page
1. INTRODUCTION	7
2. EXPERIMENTAL FACILITY	9
2.1 High Pressure Tank and Auxiliary Equipment.	9
2.2 Diagnostic Equipment.	11
2.2.1 Holographic Interferometer	12
2.2.2 Particle Tracking Apparatus.	15
2.2.2.1 Particulate Seeded Bubbles.	15
2.2.2.2 Camera/Flash System	15
2.2.3 Shadowgraph System	16
3. DATA ACQUISITION AND INTERPRETATION	17
3.1 Acquisition of Interferometry Data.	17
3.2 Interpretation of Holographic Interferograms.	18
3.2.1 Infinite Fringe Interferograms	18
3.2.2 Finite Fringe Interferograms	21
3.2.3 Advantages/Disadvantages of Infinite Fringe/ Finite Fringe.	21
4. DATA REDUCTION.	24
4.1 Holographic Interferometry Data	24
4.1.1 Averaging Radial Fringe Shift Distributions.	25
4.1.1.1 Establishment of Coordinates on Individual Interferograms	25
4.1.1.2 Obtaining Fringe Profiles from Individual Interferograms	29
4.1.1.3 Data Averaging.	30
4.1.2 Calculation of Density and Mass Concentration Fields	32
4.1.2.1 Abel Inversion of Fringe Shift Equation.	33
4.1.2.2 Bimolecular Mixing Flow Relations	34
4.1.3 Fireball Wake Interferometry Data Reduction.	37
4.2 Size/Rise Data.	38

TABLE OF CONTENTS (Continued)

	Page
5. EXPERIMENTAL RESULTS.	41
5.1 Vortex Size and Rise Results.	41
5.2 Comparison of Turbulent Laboratory Data with Full Scale Event	48
5.3 Laboratory Fireball Mass Concentration Results. . . .	52
5.3.1 Results of Data Averaging.	52
5.3.2 Effect of Reynolds Number on Averaged Mass Concentration Profiles	53
5.3.3 Effect of Rise Position (or Time) on Mass Concentration.	56
5.3.4 Laboratory Fireball Wake Results	61
5.4 Composite Iso-concentration Picture for a Turbulent Vortex.	63
6. CONCLUSIONS	66
7. RECOMMENDATIONS	68
8. REFERENCES.	70
APPENDICES	
A CHARACTERIZATION OF PARTICLE PATH DEPENDENCE.	74
B ABEL INVERSION OF THE AXISYMMETRIC FRINGE SHIFT EQUATION.	77
C EFFECT OF ERROR IN $\frac{dS}{dr}$ NEAR THE SINGULARITY IN THE ABEL INVERSION OF THE FRINGE SHIFT EQUATION	80
D CALCULATION OF MASS IN LABORATORY FIREBALLS	83
E TABULATED MEAN CONCENTRATION DATA	88

ILLUSTRATIONS

		Page
1.	High Pressure Test Facility, Holocamera, and Support Equipment.	10
2.	Schematic Diagram of Holocamera.	13
3.	Infinite Fringe Interferogram of Helium Filled Soap Bubble	19
4.	Typical Laminar Infinite Fringe Interferogram.	20
5.	Typical Turbulent Infinite Fringe Interferogram.	20
6.	Typical Laminar Finite Fringe Interferogram.	22
7.	Typical Turbulent Finite Fringe Interferogram.	22
8.	Schematic of Interferometry Data Reduction - Infinite Fringe	27
9.	Schematic of Interferometry Data Reduction - Finite Fringe	28
10.	Nomenclature and Axes for Shadowgraph Data Reduction	39
11.	Mean Laboratory Size/Rise Data	42
12.	Laboratory Fireball Rise History	46
13.	Multiple Exposure Photograph of Particulate Seeded Laminar Fireball	47
14.	Multiple Exposure Photograph of Particulate Seeded Turbulent Fireball	49
15.	Comparison of Laboratory and Full Scale Fireball Size/Rise Data.	50
16.	Comparison of Laboratory and Full Scale Fireball Size History Data	51
17.	Averaged and a Typical Radial Fringe Shift Distribution.	54
18.	Mean Radial Mass Concentrations; Laminar and Turbulent Data at Same Rise Position ($\sim 6 D_0$).	55

ILLUSTRATIONS (Continued)

	Page
19. Averaged Radial Mass Concentration at Various Rise Positions; Turbulent Results	58
20. Normalized Mass Concentration Distributions; Turbulent Data at Various Rise Positions	59
21. Normalized Mass Concentration Distributions; Laminar Data at Two Rise Positions	60
22. Averaged Wake Mass Concentration Distributions; Laminar and Turbulent Data	62
23. Iso-concentration Profiles for a Turbulent Vortex.	64
A-1. Particulate Path Dependence on Parameter λ_0	75

1. INTRODUCTION

The prediction of radar and optical signatures resulting from atmospheric nuclear detonations requires reliable fireball entrainment and mixing models. Essential to these predictions is a sound knowledge of the temperature, chemical species, and velocity fields which are not provided by available data from nuclear tests. The objective of this program was to investigate turbulent mixing and entrainment of air in fireballs by means of a subscale laboratory simulation and to provide a data base to support the development and evaluation of theoretical fireball models and codes.

The development of fireballs from low yield (<100 kt) bursts at low altitudes (<30 km) will be dominated by buoyancy forces. The initial stage of these fireballs resulting from large energy release within the atmosphere is characterized by spherical symmetry, the domination of radiative energy transport, and the propagation of a strong spherical shock wave. On the order of a second after detonation, the fireball comes to pressure equilibrium with the ambient air and because of its low density, begins to rise. As the fireball rises, circulation causes a toroid to be formed. This series of laboratory experiments which have been performed were designed to simulate these "buoyant rise" fireballs after pressure equilibration.

This report provides a complete summary of this experimental test program which was conducted during the period from August 1971 through September 1973. Although the emphasis in this report is on the experimental results and conclusions drawn from those results, descriptions of the test facility and discussions of the data acquisition, interpretation and reduction procedures are also included.

Several topics were investigated during the course of this experiment and many interesting results are discussed in detail. Mean size/rise characteristics and particle tracking photographs are presented to illustrate gross flow features. Laboratory turbulent results were compared to dimensional data from a full scale nuclear event (through proper scaling) and showed very good agreement. Results obtained during this study

illustrated a marked difference between turbulent and laminar flow regimes, and thus the emphasis in this report is placed on the turbulent results. Averaged mass concentration profiles across the center of the vortex as well as through the laboratory fireball wake are discussed. An iso-concentration picture which provides the complete averaged spatial distribution of the low density gas in a turbulent laboratory event is presented. Much of the data acquired during the course of this study is discussed, but for completeness, all acquired data was tabulated and is included in Appendix E.

2. EXPERIMENTAL FACILITY

A test facility consisting of several primary components including a high pressure test tank with optical ports, equipment for the remote formation, sensing, and controlled bursting of soap bubbles filled with low density gas, and the necessary diagnostic equipment to obtain density field measurements and flow visualization photographs of the internal and external vortex flow were designed, developed, and utilized in the performance of this experimental study.

2.1 HIGH PRESSURE TANK AND AUXILIARY EQUIPMENT

The high pressure tank is an ASME pressure vessel with a diameter of 54 inches and a length of 14 feet. A photograph of the test tank installed in the TRW Fluid Mechanics Laboratory is shown in Figure 1. This facility was designed to operate in a pressure range from vacuum conditions to 10 atmospheres.

A system was designed and developed to remotely form soap bubbles filled with low density gas (relative to the ambient higher density gas) in the high pressure test tank. Helium was used as this low density gas when air was used as an ambient medium, while nitrogen-filled bubbles were used in the higher Reynolds number SF_6 tests. Positive displacement pistons and a valving system were used to meter the amount of low density gas and soap solution to the bubble tube to accurately control the bubble size.

A small electrode spaced about 20 mils from the bubble tube with a 200 microfarad capacitor discharge system was initially used to burst the bubbles. As a result of early asymmetries present in vortices generated by this initial electrical discharge bubble breaking system, a mechanical breaking technique was developed which repeatedly produced a symmetric helium release. This technique consisted of remotely dropping a 125 mil stainless steel sphere from an electromagnet mounted inside the tank through the top center of the bubble. Tests with no bubble have shown that no more than 1/16" dispersion from the target ever existed and interferograms taken just milliseconds after arrival of the sphere at all test pressures indicated that this system provided a symmetric helium release.

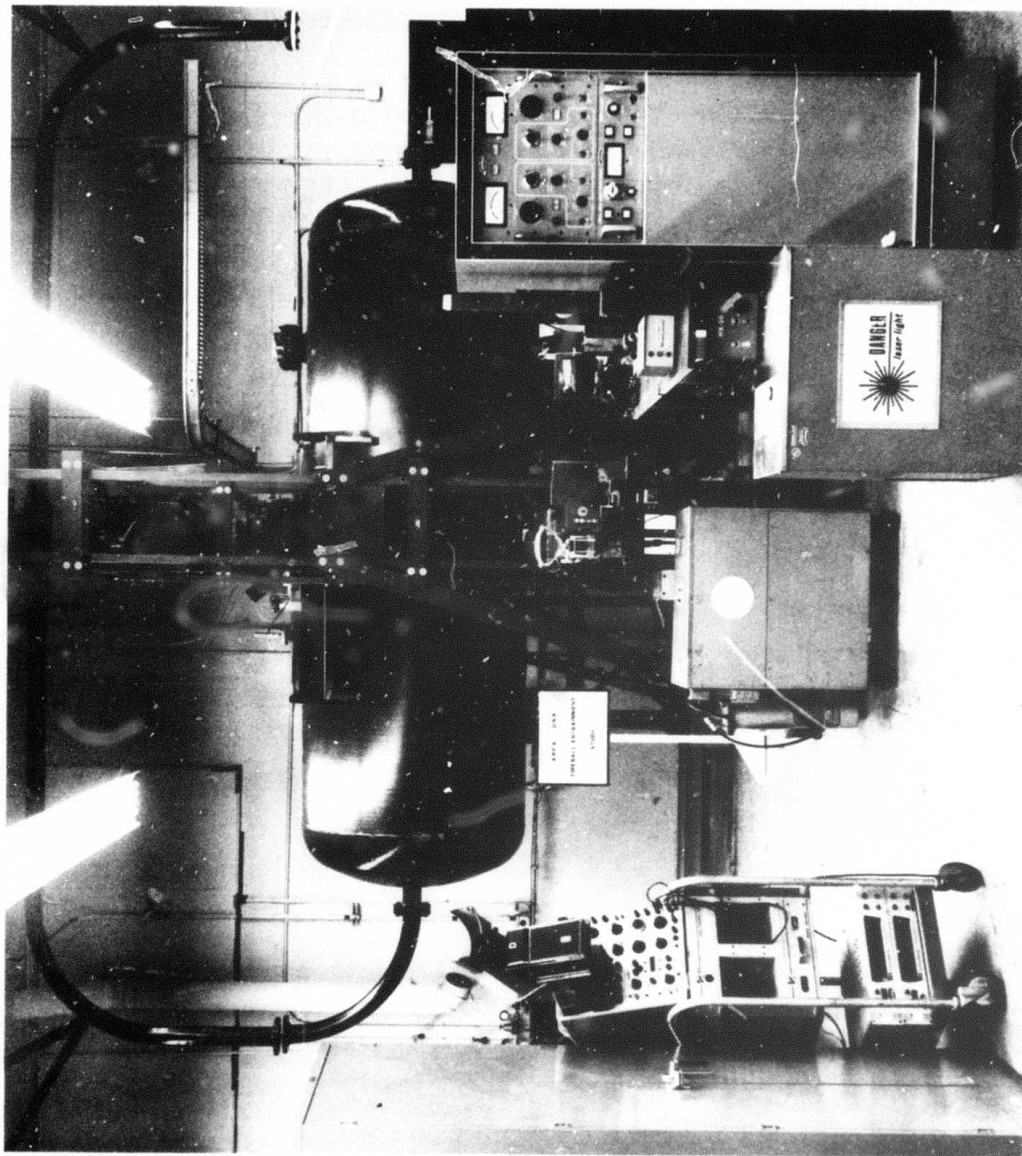


Figure 1. High Pressure Test Facility, Holocamera, and Support Equipment

The bubble formation head and electrode breaker/sensor were designed as an integral unit so they could be traversed vertically within the tank through a 1-inch diameter access flange and seal. The bubble tube position could be varied from the center to 30 inches below the horizontal viewing ports. As a result of the complexity of the optical instrumentation, and in particular the interferometry apparatus, it was essential that they remained fixed relative to the tank viewing ports which necessitated the vertical relocation of the event initialization point in order to provide data at the various desired rise positions.

2.2 DIAGNOSTIC EQUIPMENT

In order to completely specify the fluid state and motion, the following must be known for a non-reacting gas: two thermodynamic variables, such as pressure and temperature; a variable of the motion, such as velocity, and the composition of the field. Measurements of the tank pressure and temperature, outside the induced flow, specified the pressure and temperature of the field since the induced fluid motion was incompressible (i.e., low velocity and adiabatic). Of the remaining two unknowns, the density or composition field was measured optically using holographic interferometry and although the velocity field was not measured directly, an optical particle tracking technique was used to provide information on the internal unsteady flow structure. In addition, a shadowgraph system was used to provide data on the external shape and position of the events as a function of time. Optical techniques were adopted for this study because of three primary difficulties involved with flowfield probes. First, interpretation of data obtained from probes in a highly three-dimensional flow is almost impossible. Also, probe interference effects are sizable in an incompressible flow such as this, and finally the cost and time consumed in reconstructing a time dependent flowfield from local measurements was prohibitive.

2.2.1 Holographic Interferometer

Pulsed laser holographic interferometry was used to measure the mean density field of the rising toroids. The laser holograph* used in this program was similar in design to one used in previous fluid mechanic studies at TRW but was considerably larger in size to accommodate the large high pressure tank. The main feature of the holocamera is that it records orthogonal views simultaneously across the tank test section. Consequently, this system is capable of recording any transmission subject in an 8-inch diameter area in line with the 4- by 5-inch photographic plates and the large 18-inch objective lens at the opposite ports. The advantages of using this holographic interferometer as compared to the standard Mach Zehnder interferometer include the three-dimensional viewing and depth focusing properties of holographic interferograms, and the fact that precision optics and accurate alignment are not required with holographic interferometry since a common optical path is used for both the scene and comparison beams. A schematic of the complete holocamera identifying all primary optical components is presented in Figure 2. A photograph of the holocamera together with the test tank was shown in Figure 1.

In this holocamera the primary beam from the laser is split into a reference and a scene beam. The scene beam is directed through the event to the plates whereas the reference beam is directed on the plates without passing through the disturbance. The prism plate and lenses shown in Figure 2 are used to spatially and temporally match the scene and reference beams over the plates. A Q-switched solid state ruby laser with an energy of about 1 joule and pulse length of about 100 nanoseconds was used to expose both the vertical and horizontal beam holograms which were recorded on Agfa-Gavaert 8E75 plates.

*The term laser holograph pertains to both the laser cavity or oscillator, and all other optical components which comprise the holocamera.

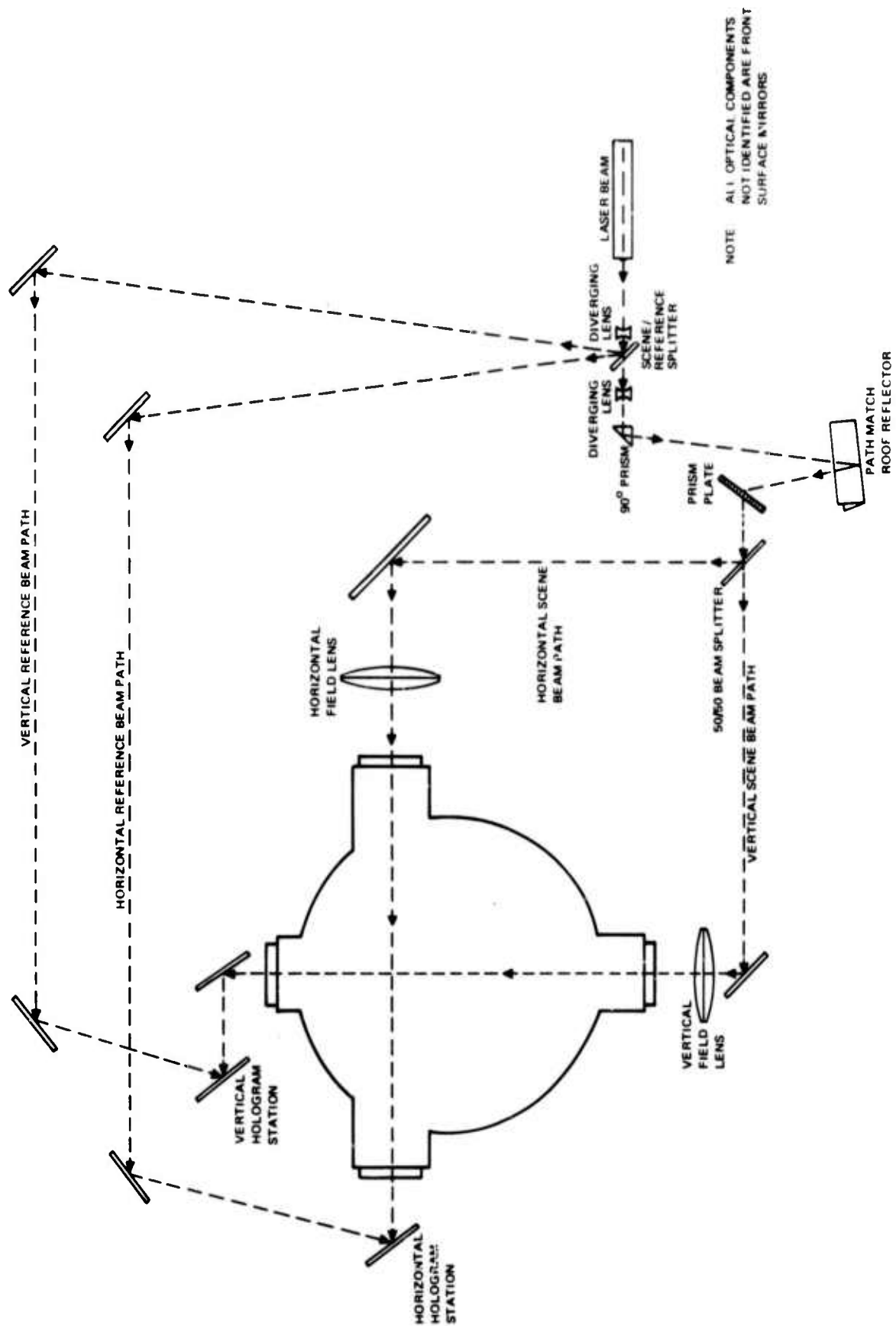


Figure 2. Schematic Diagram of Holocamera

Interferograms were obtained in this common path interferometer by sequentially recording the comparison and scene beams on the same plates. The double exposure of the plates by the two pulses, the one of the undisturbed volume and the other of the same volume with the test scene introduced, produced the interferograms. The principle of operation of any interferometer is that optical interference occurs between two coherent beams passing through media of different density. When optical paths differ by an integral multiple of the wavelength of the monochromatic light source, λ , ($\Delta L = n\lambda$, $n = 0, 1, 2, 3 \dots$) the beams reinforce one another. Conversely, when the optical paths differ by odd multiples of $\lambda/2$ ($\Delta L = \lambda/2, 3\lambda/2, 5\lambda/2 \dots$), complete interference occurs. Reinforcement shows up as light fringes on the holographic plate whereas complete interference creates dark fringes.

When the finite fringe technique is used, the plate holder and its adjacent mirror are rotated between event and comparison exposures in such a manner that the optical paths of the scene and reference beams change uniformly over the entire plane of the holographic plate, creating a raster of parallel fringes. The spacing of these fringes is dependent on the amount of rotation of the plate holder and mirror. The more the mirror and plate holder are displaced, the greater is the path mismatch, and consequently, the interference fringes become narrower. Whatever additional shift is caused by the test disturbance shows up as fringes displaced from the uniform raster. When the infinite fringe technique is implemented, no optical components are rotated between exposures. Only the disturbance in a blank background appears, hence the name infinite fringe. Various examples of finite and infinite fringe interferograms were presented in References 1 and 2 and appear in this report in Figures 3 through 7. A further discussion of the acquisition and interpretation of both finite and infinite fringe interferograms and the advantages and disadvantages of each is included in Section 3.

2.2.2 Particle Tracking Apparatus

Equipment providing the capability of obtaining multiple exposure photographs of a rising vortex with its initial bubble seeded with a particulate tracer was developed and used to provide data on the internal vortex structure.

2.2.2.1 Particulate-Seeded Bubbles

Several different types of flow tracers were tested, such as talcum powder, fine aluminum flakes, smoke, and hollow epoxy microspheres. Smoke was discarded since it could not be generated at the high operating pressures, talcum powder could not be photographed, and aluminum flakes prohibited repeatable bubble formation. Consequently, epoxy microspheres from 10 to 250 microns in diameter were incorporated as the tracing particulate. It was found that these microspheres were both a good tracer and were sufficiently visible when illuminated to be photographed. An analysis presented in Appendix A confirms the effectiveness of these particles as fluid tracers.

2.2.2.2 Camera/Flash System

A 35 mm Nikon F with motor drive having an f5.6 macro lens was selected as the optimum available camera to acquire the particle tracking photographs. Kodak Tri-X Pan (ASA 400) was chosen for film, and a special processing technique using Acufine developer was incorporated which effectively increased the speed of the film to ASA 1250, noticeably enhancing the resolution above that obtainable using standard developers.

A 7.5kV power supply operating at an energy level of about 50 joules was developed to rapidly charge a 2.5 μ F capacitor bank which when discharged, ignited an EG&G FX98C-3 (3" length, 70mm diameter) flash lamp. The capacitor discharge was triggered by a standard square wave signal generator at the desired frequency. An oscilloscope sweep triggered by the release of the bubble breaking sphere from the electromagnet facilitated accurate monitoring of the flash, enabling the time at which each exposure was taken after bubble breaking to be accurately known. The flash was masked except for two aligned slits to provide a pulsed vertical sheet of light directly above the bubble tube and normal to the line of sight of the camera. This

illumination system permitted particulate to be visible in only a cross-sectional slice (less than 1/2" wide) through each event allowing detailed visualization of the internal flow structure.

2.2.3 Shadowgraph System

In general, any light ray passing through a region whose index of refraction varies is displaced, deflected, and changed in phase relative to the path it would have taken if the index of refraction were to have been constant. If a collimated light beam is passed through a disturbed region, the image one sees on a screen on the other side of the light source from the disturbance becomes a shadowgraph. Using the approximation of small deflections, for most gases it may be shown that the change in light intensity on the screen due to the disturbance is proportional to the second derivative of the density within the disturbed region (see Reference 3 for example).

The shadowgraph system used in this study utilized a point light source (500 watt Mercury arc lamp) to the right of the large lens adjacent to the tank window in Figure 2. The lens collimated the beam and a translucent vellum screen was placed on the left tank window. A 16 mm Bell and Howell movie camera with a wide-angle lens using Eastman 4-X movie film (ASA 500) at 24 frames/second was used to record the events.

3. DATA ACQUISITION AND INTERPRETATION

The purpose of this section is to discuss both the procedure for obtaining infinite fringe and finite fringe holographic interferograms and the physical interpretation of these forms of data. As well, the acquisition and interpretation of particle tracking photographs and the acquisition of shadowgraph data are discussed.

3.1 ACQUISITION OF INTERFEROMETRY DATA

The procedure which was used to obtain a set of infinite fringe interferograms of a simulated fireball consisted of the following primary steps:

- 1) Plate holders containing the special fine grain, low speed photographic plates were loaded in the horizontal and vertical plate holder receptacles.
- 2) The slides covering the plates were drawn after the laser and bubble blowing apparatus had been checked and all sources of illumination in the test area had been eliminated.
- 3) The laser power supply was charged and a soap bubble filled with low density gas was blown to a predetermined size.
- 4) About five seconds after its formation, the bubble was burst.
- 5) Simultaneous with the bubble bursting, an electrical signal, first sent through a time delay circuit, activated the laser firing mechanism which recorded the test scene on the plates. The time delay was adjusted to allow the helium cloud to rise a predetermined amount.
- 6) A comparison scene was recorded on the plates by firing the laser a second time about 30 seconds after the event scene. This delay ensured that the disturbance was well outside of the viewing region resulting in a uniform, constant density comparison scene.
- 7) The photographic plates were removed and developed using special photographic developing agents.
- 8) The holograms were reconstructed, i.e., observed and photographed by illuminating the holograms with a CW laser.
- 9) Large scale working photographs were then produced for use in the data reduction phase as described in Section 4.1.

A horizontal view finite fringe interferogram was obtained by following the exact procedure as outlined above except for the addition of one step. This consisted of rotating the horizontal beam plate holder and adjacent mirror a small precise amount between steps 5 and 6 above, i.e., between recording the test and the comparison scenes on the plate. The amount of this rotation determines the spacing of the undisturbed fringes.

3.2 INTERPRETATION OF HOLOGRAPHIC INTERFEROGRAMS

Interpretation of both infinite fringe and finite fringe interferograms are included in this section since both types of data were acquired and analyzed during the course of this study.

3.2.1 Infinite Fringe Interferograms

An example of an infinite fringe interferogram is presented in Figure 3. This horizontal view hologram was obtained with an unbroken one-inch diameter helium bubble at a tank pressure of one atmosphere. Each fringe in this type of interferogram corresponds to a locus of constant optical path so interpretation for data reduction purposes consists of numbering and locating the fringes along any plane of interest through the fireball. These fringe numbers and locations can directly be used to determine the integrated density or helium concentration change through the fireball along that optical path. Details of the computational procedure required to obtain concentration profiles from these fringe number data are presented in Section 4.1. In the sample infinite fringe interferogram presented, the density is constant inside the bubble and lower than the constant density region outside the bubble by about a factor of 7. Consequently, the interference fringes which consist of concentric circles with decreasing spacing as their radii increase depict only changes in optical path length through the helium sphere.

Another example of an infinite fringe interferogram is shown in Figure 4. This interferogram shows a laminar vortex formed from an initial one-inch diameter helium bubble at one atmosphere pressure after a rise of about 4 initial bubble diameters. The fringe pattern in this figure is more typical of that expected in this study in that the fringe geometry and spacing result from a toroidal cloud containing a mixture of helium and air.

Reproduced from
best available copy.

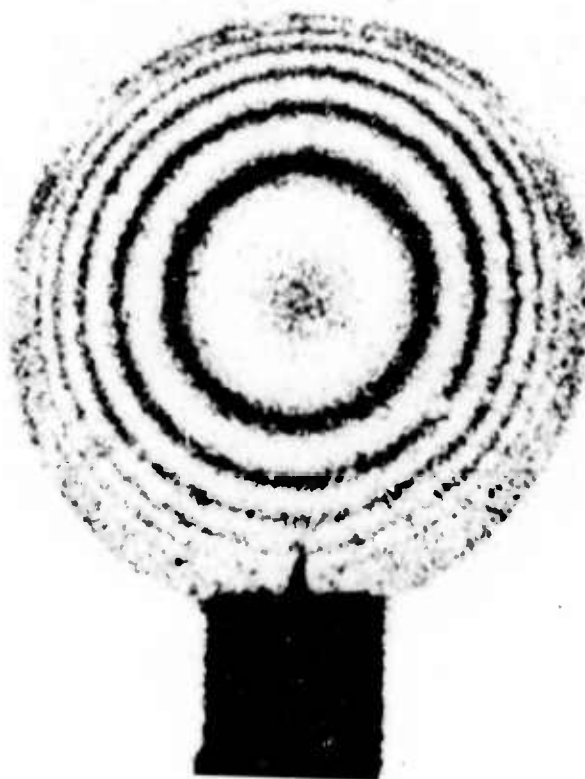


Figure 3. Infinite Fringe Interferogram of Helium Filled Soap Bubble

Reproduced from
best available copy.

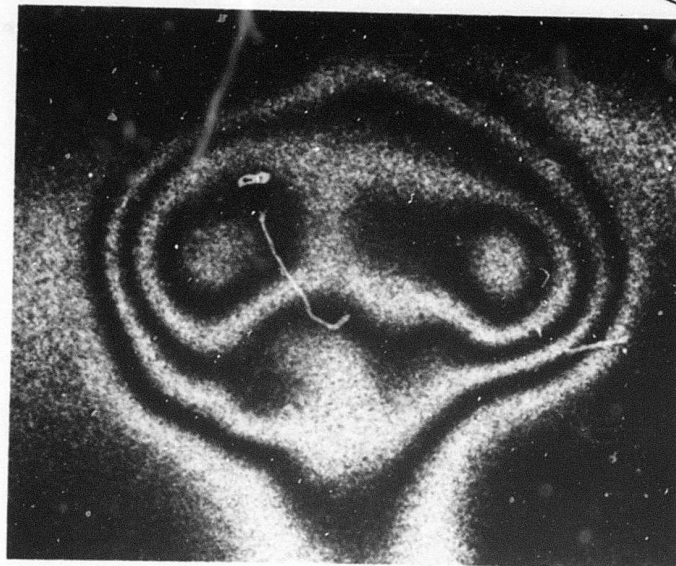


Figure 4. Typical Laminar Infinite Fringe Interogram

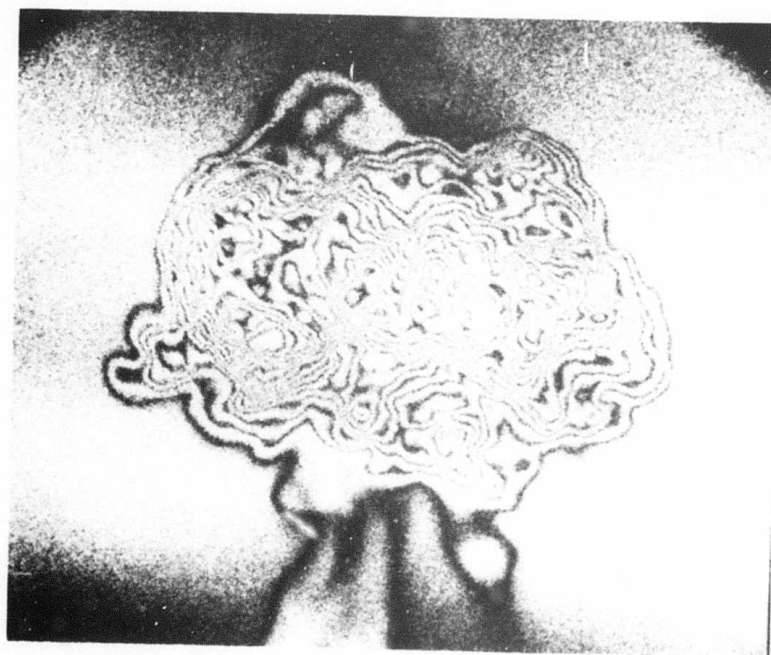


Figure 5. Typical Turbulent Infinite Fringe Interferogram

A turbulent vortex, typical of the higher Reynolds number results in this study, is shown in Figure 5 as a third example of an infinite fringe interferogram. This event was formed from an initial one-inch diameter helium bubble at eight atmospheres pressure after a rise of about 5 initial bubble diameters (Reynolds number a factor of 8 larger than the event in Figure 4). It is obvious by comparing this event with the lower Reynolds number hologram in Figure 4 that the higher Reynolds number fireball contains small scale turbulent structure, not present in the laminar case.

3.2.2 Finite Fringe Interferograms

An example of a finite fringe interferogram is presented in Figure 6. This interferogram was obtained at the same test conditions as the infinite fringe interferogram in Figure 4 but at a higher rise position (6 initial bubble diameters). In this type of hologram, the test disturbance causes a displacement or shift in the fringes relative to the undisturbed portion of the test section. An increase in optical path is shifted in the opposite direction to a decrease in optical path. Consequently, no ambiguity can occur in regard to the fringe shift direction. The magnitude of the fringe shift in this type of hologram can be directly related to fringe number in an infinite fringe hologram and therefore to an integrated change in density or concentration along the optical path.

A second example of a finite fringe interferogram is presented in Figure 7. This hologram of a turbulent vortex was obtained at the same conditions as the infinite fringe interferogram of Figure 5 but at a slightly higher rise position of 6 initial bubble diameters. As demonstrated by this example, finite fringe holograms with easier-to-reduce continuous fringes can be obtained in small events with high helium concentrations by increasing the amount of mirror and plate rotation between recording the test scene and comparison scene on the hologram plates.

3.2.3 Advantages/Disadvantages of Infinite Fringe/Finite Fringe

The advantages of the infinite fringe arrangement are twofold. First, the overall setup and care of the optics is much simpler since path matching of the two beams is not altogether critical. Secondly, the infinite

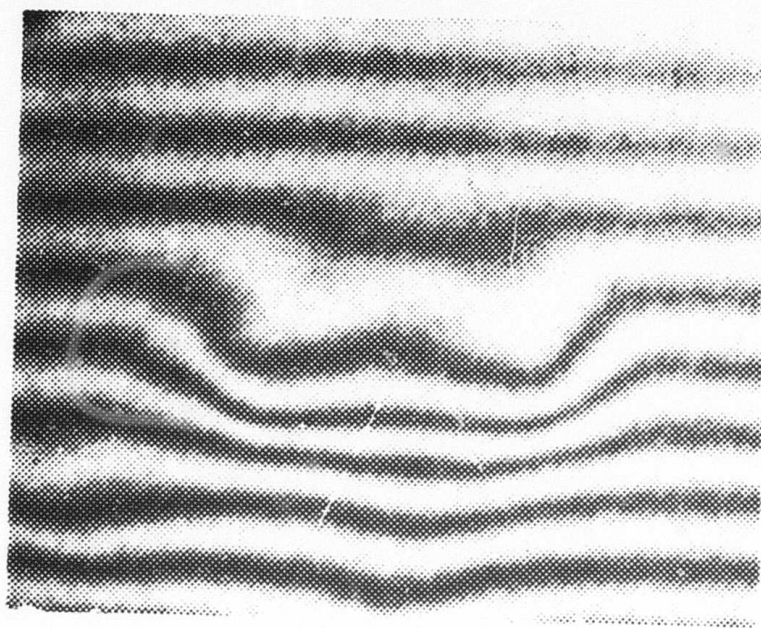


Figure 6. Typical Laminar Finite Fringe Interferogram

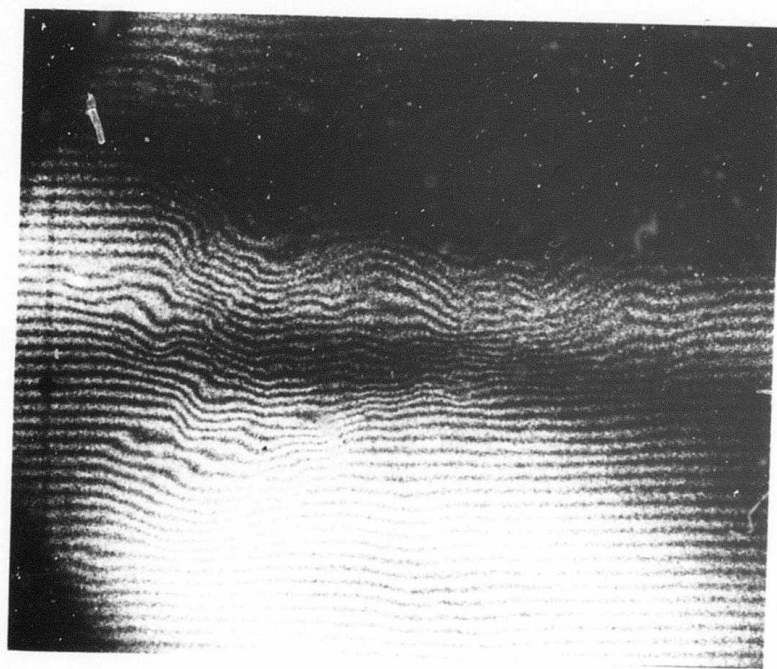


Figure 7. Typical Turbulent Finite Fringe Interferogram

fringe interferogram provides an excellent outline of the test event and a clear physical picture of the internal flowfield.

However, the advantages of the finite fringe technique, especially in providing a wide range of test conditions, outweigh for the most part the merits of the infinite fringe technique. When there exist relatively large density gradients in the flow (i.e., very many fringes of shift along a small length), and when the flow is turbulent, the fringes tend to be very irregular in shape and difficult to delineate in an infinite fringe interferogram. Also, it is not known internally whether a fringe shift means an increase or decrease in density. Consequently, an *a priori* knowledge of the flowfield is a prerequisite to use that technique. Even though the infinite fringe approach is more simple and provides better visual insight to the flow, the flexibility of the finite fringe technique (rotating elements in an amount commensurate with the character of the flow) proved to be most advantageous. Without its implementation, the wide range of Reynolds number variation at identical stages of vortex development and especially the acquisition of high Reynolds number data could not have been accomplished.

4. DATA REDUCTION

The objective of this section is to describe in detail techniques which were used in reducing holographic interferometry data (both infinite fringe and finite fringe) and shadowgraph data as they applied to this study.

4.1 HOLOGRAPHIC INTERFEROMETRY DATA

The process of achieving the final result, namely determining the mean density and mass concentration fields from the holographic records consisted of two primary steps. The first step consisted of fringe interpretation, determination, and averaging. Once an average fringe distribution was determined for a large set of repeat data, computer reduction of the density and mass concentration fields was able to be accomplished. This basic approach has been used in a number of former studies at TRW (References 4, 5 and 6) but the averaging technique is unique to this study.

The fringe shift S measured from the interferograms is related to the index of refraction n (from which density and mass concentration are determined) according to the following integral equation:

$$S = \frac{1}{\lambda} \int_{-\infty}^{\infty} (n - n_{\infty}) ds$$

where λ = wavelength of light in vacuum

ds = differential path length along light ray

and subscript ∞ corresponds to undisturbed conditions.

The problem reduces to solving this integral equation for the change in index of refraction, $(n - n_{\infty})$, as a function of fringe shift, S . The mechanics of inverting the integral will be discussed in detail in Appendix B.

This solution is accomplished by restricting consideration to an axisymmetric geometry. Naturally, to use this technique to produce results that are meaningful, the input fringe data must originate from an axisymmetric event. To obtain an axisymmetric event, some type of average of repeat sets of fringe distributions must be obtained. One could take an average

in such a way to yield a probability-type result for density at a specified location in space, i.e., a tank-fixed approach. This would result in a very smeared out* vortex which in no way would resemble a typical vortex. Instead, an approach was developed whereby a coordinate system was established for each individual vortex based on the location of three points common to all vortices, but located in general differently from event to event. This approach retained the important physical features of the flow and produced a symmetric vortex which was a representative average vortex rather than a smeared out vortex average. This averaged fringe distribution forms the topic for the next section.

4.1.1 Averaging Radial Fringe Shift Distributions

To obtain an averaged radial fringe distribution for a particular set of repeat interferograms, several basic steps were undertaken. First, coordinates were established on the interferograms, and individual fringe profiles were constructed. The data were then all collapsed about points characteristic to all vortices in general. Once this had been accomplished, an average $S(r)$ distribution was calculated, and being satisfactorily symmetric, was then used as the input to the density field and mass concentration field calculations.

4.1.1.1 Establishment of Coordinates on Individual Interferograms

An infinite fringe interferogram was visually examined to determine the position of the saddle point by counting fringes inward from the edge of the vortex. In this connotation, the saddle point is defined as the point where the fringe number (see Section 4.1.1.2) simultaneously attains a maximum value in an axial direction and a minimum value in the radial direction. Two fringe maxima positions (generally having different fringe numbers) were determined in the same manner and an x-axis was drawn through them. The y-axis was then drawn orthogonal to the x-axis and through the saddle point. The point where the x- and y-axes intersected defined the

*In the sense that the averaged event would be much larger than any individual vortex and the important edge gradients would be reduced.

vortex coordinate origin, or for the sake of brevity, simply the origin. Reference to Figure 8 shows that:

- x_{LE} = distance from origin to first dark fringe on left side
- x_{LM} = distance from origin to fringe maximum on left side
- x_{RM} = distance from origin to fringe maximum on right side
- x_{RE} = distance from origin to first dark fringe on right side
- y_{sp} = distance from origin to saddle point

Tank-fixed parameters of purely statistical interest are:

- η = rotation of x-axis from true horizontal
- z_0 = vertical rise distance of origin from top of bubble tube
- x_0 = horizontal distance from origin to center of bubble tube

Figure 9 represents a schematic diagram of a finite fringe interferogram which illustrates the placement of coordinates. Note that locating the maxima and saddle point was not accomplished by counting fringes inward from the edges, but by determining relative displacements of fringes from their undisturbed positions. These features do not become immediately obvious as was the case with finite fringe interferograms, and to identify them correctly requires some hunting. Once these three points have been correctly determined, all coordinates become established in an identical fashion to the infinite fringe coordinates.

One set of finite fringe interferograms in particular was more thoroughly analyzed for the purpose of constructing a map of the entire vortex vortex field. For this set (10 atmospheres pressure, N_2 bubbles in an SF_6 environment, 10.4 initial bubble diameters rise, and an initial bubble diameter of 1/2 inch), four additional cuts through the vortex as well as three cuts through the fireball wake were made. The vertical positions of the four additional vortex cuts parallel to the central cut were normalized with respect to where the top of the vortex intersected the y-axis, y_t , and where the bottom of the vortex intersected the y-axis, y_b . These cuts were made at $1/3 y_t$, $2/3 y_t$, $1/3 y_b$, and $2/3 y_b$. For the $1/3 y_t$ and $1/3 y_b$ cuts, the two maxima and central minimum were identified in an

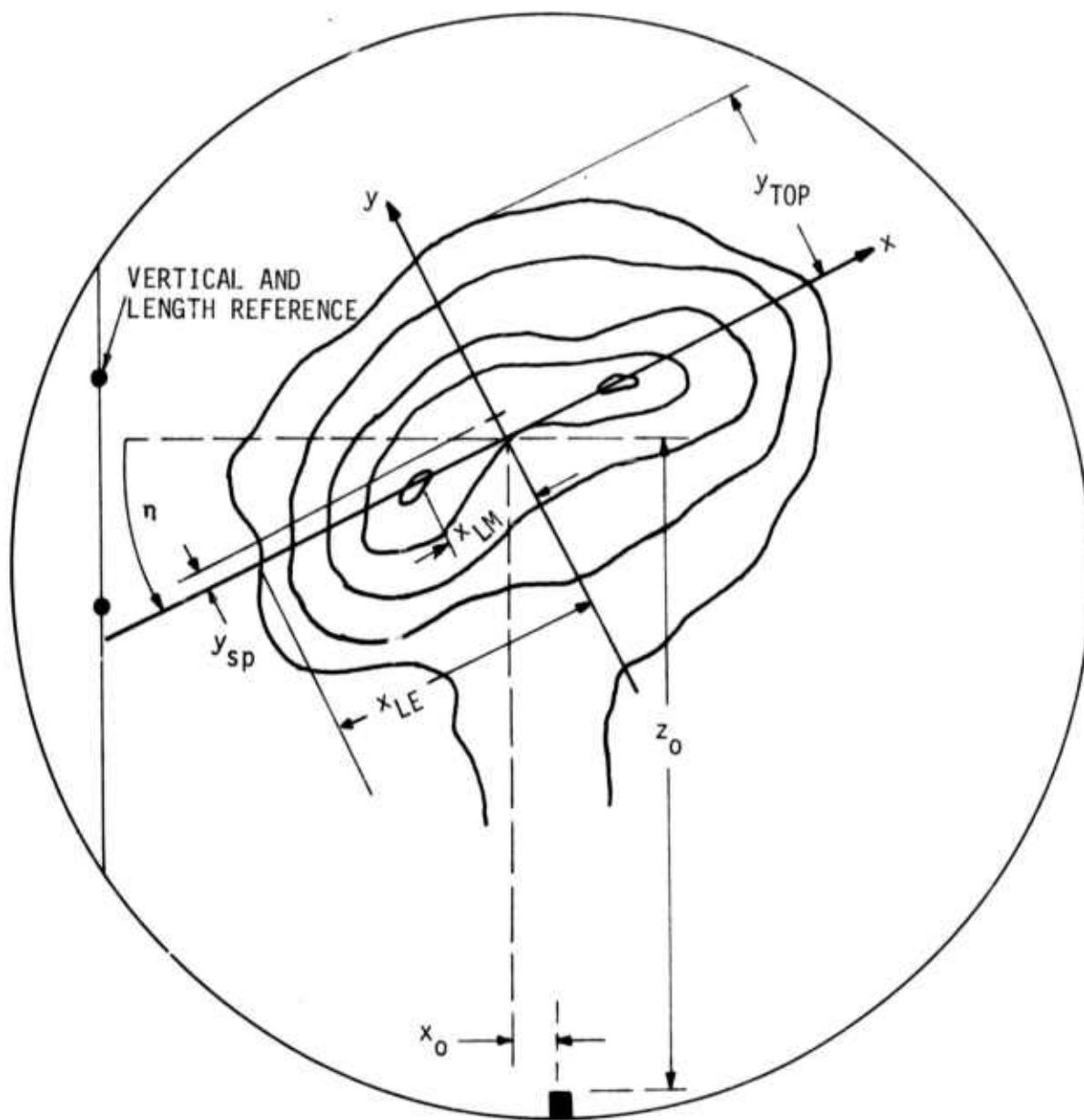
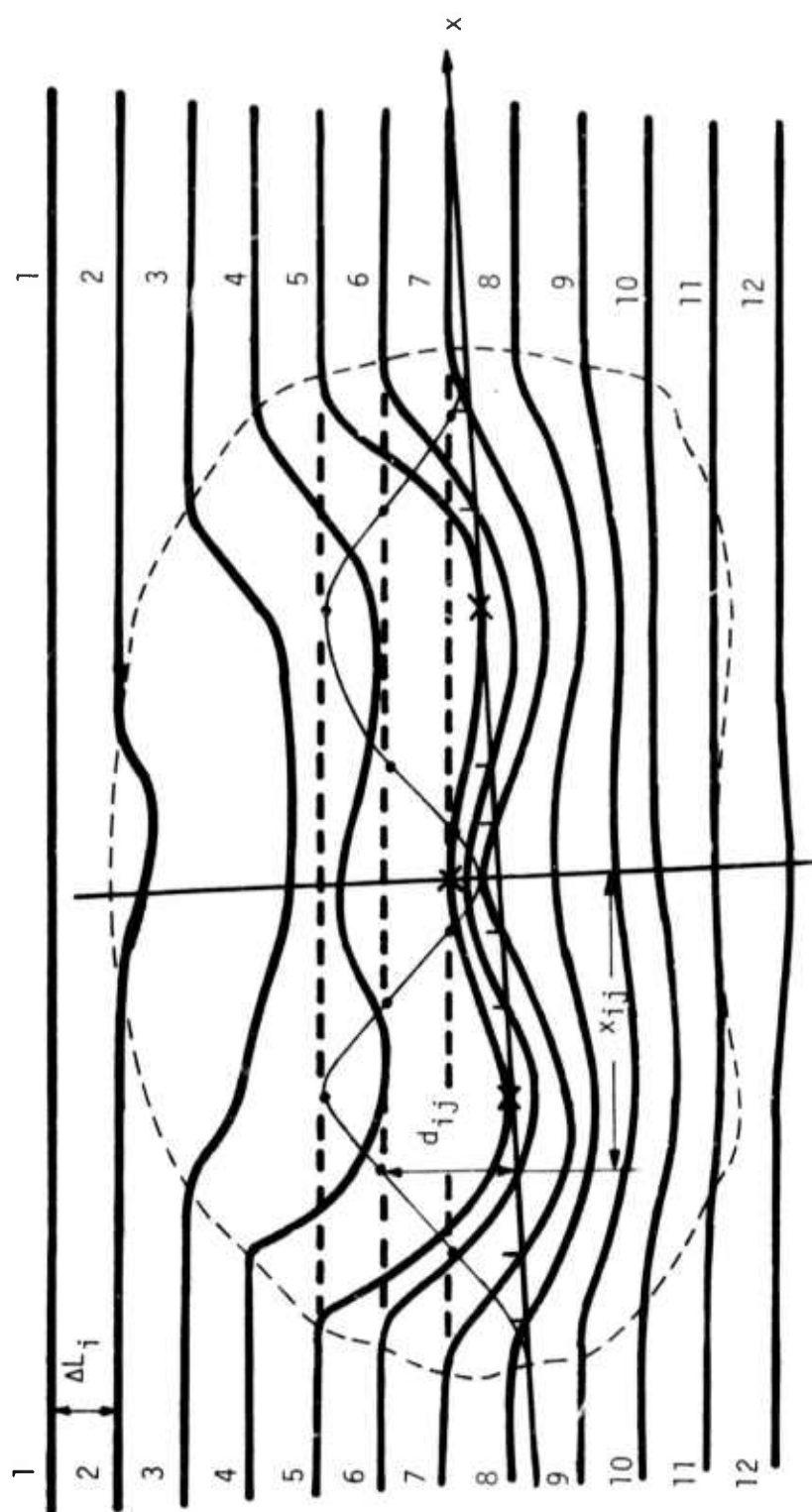


Figure 8. Schematic of Interferometry Data Reduction - Infinite Fringe



$$S_{ij} = \frac{d_{ij}}{\Delta L_i}$$

Figure 9. Schematic of Interferometry Data Reduction - Finite Fringe

identical fashion to the central cut. For the $2/3 y_t$ and $2/3 y_b$ cuts, more often than not maxima could not be detected and consequently the central minimum became the only criterion for coordinate selection. No bias from the central cut was placed on locating the central minimum or the maxima to again preserve the physical flow features. The motivation behind allowing these coordinates to float was that in the mean, averaged over a sufficient number of events, they would coincide with those of the central cut (results show that they did indeed).

4.1.1.2 Obtaining Fringe Profiles from Individual Interferograms

For infinite fringe interferograms, the center of each fringe was located and numbered where it intersected the x-axis defined in the previous section. The numbering started with $S = 1/2$ for the outermost dark fringe (corresponding to the half-wavelength shift in optical path discussed earlier), $S = 1$ for the next inward light fringe, and so on, increasing by $1/2$ each time a new fringe was encountered. Care had to be taken to give the same fringe the same number when it intersected the x-axis more than once. What resulted were m ordered pairs (x_{ij}, S_{ij}) $j = 1, 2, \dots, m$ for every i^{th} interferogram, $i = 1, 2, \dots, n$.

Because of the nature of the finite fringe interferogram, this step in the data reduction procedure was considerably different than the above for infinite fringe data. Reference again to Figure 9 shows that all fringes were first identified by number (not to be confused with $S = 1/2, 1, 1 1/2$, etc. for infinite) in the undisturbed regions both to the left and to the right of the event. A mark was made wherever the center of any fringe intersected the x-axis, and each mark was identified by its fringe identification number by following its fringe into the undisturbed region where it was numbered. Then, the distance normal to the parallel fringes from the disturbed fringe to where its undisturbed fringe would be if there were no disturbance, d_{ij} , was measured, and divided by the fringe spacing, ΔL_i , to give S in terms of number of fringes of shift. This S was completely analogous to the S obtained by counting fringes inward from the edge for infinite fringe interferograms.

It should be noted that all that follows in the remainder of Section 4.1 applies equally to both infinite and finite fringe data.

4.1.1.3 Data Averaging

In the process of establishing an average vortex, it was essential to preserve the important physical features by normalizing the characteristic dimensions of each individual vortex. The dimensions selected for this purpose were the locations of the fringe maxima and the left and right edges relative to the origin.

To transform each event into a system of coordinates whereby maxima collapsed onto the mean maxima and edges collapsed onto the mean edges, the general linear transformation $\bar{x}_{ij} = ax_{ij} + b$ was used. First, the average locations of the edges and the maxima were computed using

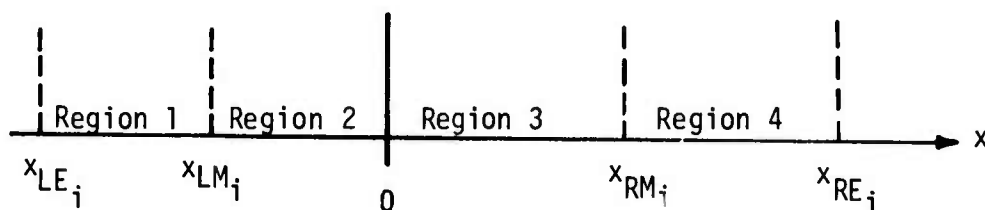
$$\bar{x}_{LE} = \frac{1}{n} \sum_{i=1}^n x_{LE_i}$$

$$\bar{x}_{LM} = \frac{1}{n} \sum_{i=1}^n x_{LM_i}$$

$$\bar{x}_{RM} = \frac{1}{n} \sum_{i=1}^n x_{RM_i}$$

$$\bar{x}_{RE} = \frac{1}{n} \sum_{i=1}^n x_{RE_i}$$

The event was then divided into four regions as shown below and the normalization was accomplished separately within each region.



The constants for a and b in the general linear transformation were determined by matching the endpoints within each region to the averaged endpoints. For example, in region 1, at

$$x_{ij} = x_{LE_i}, \bar{x}_{ij} = \bar{x}_{LE_i}; \text{ and, at } x_{ij} = x_{LM_i}, \bar{x}_{ij} = \bar{x}_{LM_i}$$

For the j^{th} data point on the i^{th} interferogram, the new coordinates \bar{x}_{ij} were:

In region 1,

$$x_{LE_i} \leq x_{ij} \leq x_{LM_i}$$

$$\bar{x}_{ij} = \frac{\bar{x}_{LE} - \bar{x}_{LM}}{x_{LE_i} - x_{LM_i}} x_{ij} + \bar{x}_{LM} - \frac{\bar{x}_{LE} - \bar{x}_{LM}}{x_{LE_i} - x_{LM_i}} x_{LM_i}$$

In region 2,

$$x_{LM_i} \leq x_{ij} \leq 0$$

$$\bar{x}_{ij} = \frac{\bar{x}_{LM}}{x_{LM_i}} x_{ij}$$

In region 3,

$$0 \leq x_{ij} \leq x_{RM_i}$$

$$\bar{x}_{ij} = \frac{\bar{x}_{RM}}{x_{RM_i}} x_{ij}$$

In region 4,

$$x_{RM_i} \leq x_{ij} \leq x_{RE_i}$$

$$\bar{x}_{ij} = \frac{\bar{x}_{RE} - \bar{x}_{RM}}{x_{RE_i} - x_{RM_i}} x_{ij} + \bar{x}_{RM} - \frac{\bar{x}_{RE} - \bar{x}_{RM}}{x_{RE_i} - x_{RM_i}} x_{RM_i}$$

In cuts where normalization was accomplished only with respect to the edges e.g., $(2/3 y_t, 2/3 y_B, \text{wake cuts, etc.})$, the transformations were

for the left side,

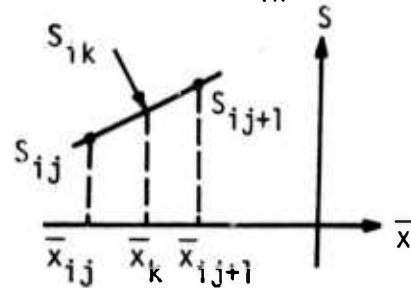
$$\bar{x}_{ij} = \frac{\bar{x}_{LE}}{x_{LE_i}} x_{ij}$$

and for the right side,

$$\bar{x}_{ij} = \frac{\bar{x}_{RE}}{x_{RE_i}} x_{ij}$$

Once all (x_{ij}, S_{ij}) had been transformed to (\bar{x}_{ij}, S_{ij}) , there existed n S_{ij} vs. \bar{x}_{ij} profiles with all edges occurring at \bar{x}_{LE} and \bar{x}_{RE} , all maxima at \bar{x}_{LM} and \bar{x}_{RM} , and the central minimum at $\bar{x} = 0$. These profiles had to be averaged with respect to S at constant \bar{x} to yield a mean \bar{S} vs. \bar{x} profile. Since every i^{th} distribution did not have a discrete value of S at the same \bar{x} , convenient x_k were chosen to be used for each i^{th} event (say $\bar{x}_k = \frac{k}{L} \bar{x}_{LE}$, $k = 1, 2, \dots, L$) and linear interpolation for S_{ik} was used between (\bar{x}_{ij}, S_{ij}) and $(\bar{x}_{ij+1}, S_{ij+1})$.

$$S_{ik} = \frac{S_{ij+1} - S_{ij}}{\bar{x}_{ij+1} - \bar{x}_{ij}} (\bar{x}_k - \bar{x}_{ij}) + S_{ij}$$



The input fringe numbers to the Abel inversion data reduction routine for an axisymmetric average vortex were simply $\bar{S}_k = \frac{1}{n} \sum_{i=1}^n S_{ik}$ for $k = 1, 2, \dots, L$. The \bar{S} vs. \bar{x} for both the left and right sides were then computed. For all practical purposes, the two sides coincided (see Figure 17 for a typical example) when the number of events averaged was sufficiently large.

4.1.2 Calculation of Density and Mass Concentration Fields

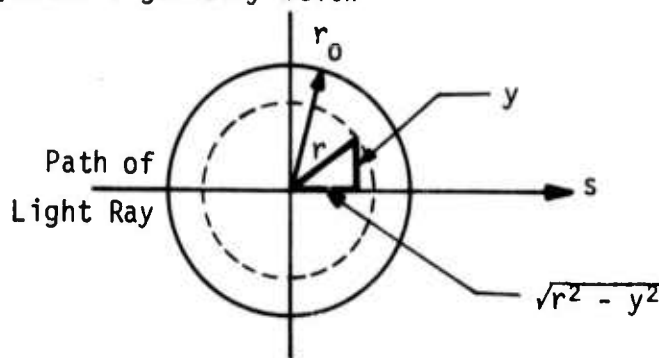
Given the fringe distribution for an axisymmetric event, it is a straightforward matter to calculate a density and mass concentration distribution along the same cut.

4.1.2.1 Abel Inversion of Fringe Shift Equation

Recall the general equation for fringe shift

$$S = \frac{1}{\lambda} \int_{-\infty}^{\infty} (n - n_{\infty}) ds$$

Assuming the axisymmetric geometry below



it is seen that the incremental path length ds becomes $d[\sqrt{r^2 - y^2}]$, and since $n = n_{\infty}$ for all $r > r_0$ and that the event consists of two equal halves, the fringe shift equation for an axisymmetric event becomes

$$S(y) = \frac{2}{\lambda} \int_y^{r_0} (n - n_{\infty}) \frac{r dr}{(r^2 - y^2)^{1/2}} \quad (1)$$

To solve for $n - n_{\infty}$, one notes that this equation is the same as Volterra's integral equation of the first kind, with the exception that the limits of integration are different. The details of the solution (Reference 7) are rather lengthy and are presented in Appendix B. It becomes

$$(n - n_{\infty})_{r=y} = -\frac{\lambda}{\pi} \int_y^{r_0} \frac{\frac{dS}{dr} dr}{(r^2 - y^2)^{1/2}} \quad (2)$$

Break this up into n integrals over n intervals

$$(n - n_{\infty})_{r=y_i} = -\frac{\lambda}{\pi} \sum_{k=1}^{n-1} \int_{r_k}^{r_{k+1}} \frac{\left(\frac{dS}{dr}\right)_k dr}{(r^2 - y_i^2)^{1/2}} \quad i = 0, 1, 2, 3 \dots$$

Assume that in each k^{th} zone $\left(\frac{dS}{dr}\right)_k$ is constant. Then,

$$n - n_{\infty})_{r=y} = \frac{-\lambda}{\pi} \sum_{k=i}^{n-1} \left(\frac{dS}{dr} \right)_k \int_{r_k}^{r_{k+1}} \frac{dr}{(r^2 - r_i^2)^{1/2}}$$

$$= \frac{-\lambda}{\pi} \sum_{k=i}^{n-1} \frac{S_{k+1} - S_k}{r_{k+1} - r_k} \log \left| \frac{r_{k+1} + \sqrt{r_{k+1}^2 - r_i^2}}{r_k + \sqrt{r_k^2 - r_i^2}} \right|$$

Let the zone width (i.e., step size) = Δr and let $i = 0, 1, 2 \dots N-1$ (zone).
Then

$$r_{k+1}^2 = [(k+1)\Delta r]^2$$

$$r_k^2 = (k\Delta r)^2$$

$$r_i^2 = (i\Delta r)^2$$

Thus

$$n - n_{\infty})_{r=y} = \frac{-\lambda}{\pi \Delta r} \sum_{k=i}^{N-1} (S_{k+1} - S_k) \log \left| \frac{(k+1) + [(k+1)^2 - i^2]^{1/2}}{k + (k^2 - i^2)^{1/2}} \right| \quad (3)$$

4.1.2.2 Bimolecular Mixing Flow Relations

This section describes how density and mass concentration fields were calculated from knowledge of the index of refraction field.

For a multi-component gas case, the index of refraction becomes,

$$n - 1 = \sum K_i \rho_i = \rho \sum K_i C_i$$

where K = Gladstone-Dale constant

C = mass concentration or mass fraction

ρ = density

subscript

i = pure species i

For helium and air (subscripts H and A, respectively)

$$n - 1 = \rho \{ K_A C_A + K_H C_H \}$$

and because by definition

$$C_A + C_H = 1$$

$$\frac{n - n_\infty}{\rho_\infty K_\infty} = \frac{\rho K_A}{\rho_\infty K_\infty} \left[C_H \left(\frac{K_H}{K_A} - 1 \right) + 1 \right] - 1 \quad (1)$$

From the perfect gas law the density ratio, ρ/ρ_∞ , may be obtained as

$$\frac{\rho}{\rho_\infty} = \frac{p}{p_\infty} \frac{T_\infty}{T} \frac{\bar{M}}{\bar{M}_\infty}$$

where T = temperature

p = pressure

M = molecular weight

superscript

-- = mean quantity

A simplifying assumption, which in any event is non-crucial to the final results, is that $p = p_\infty$ and $T = T_\infty$, i.e., the pressure and temperature of the comparison and test scenes are the same. Then, $\rho/\rho_\infty = \bar{M}/\bar{M}_\infty$.

From Dalton's Law of partial pressures,

$$p = T \sum \rho_i R_i = \rho T R \sum \frac{C_i}{M_i} = \rho T \frac{R}{\bar{M}}$$

where R = gas constant per unit mass

R = gas constant per mole

and by definition \bar{M} is

$$\frac{1}{\bar{M}} = \sum \frac{C_i}{M_i}$$

For helium and air,

$$\frac{1}{\bar{M}} = C_H \left(\frac{1}{M_H} - \frac{1}{M_A} \right) + \frac{1}{M_A}$$

Consequently the density ratio becomes

$$\frac{\rho}{\rho_\infty} = \frac{1}{C_H \left(\frac{M_\infty}{M_H} - \frac{M_\infty}{M_A} \right) + \frac{M_\infty}{M_A}}$$

The case here is for a comparison scene (sub ∞) comprised of air, thus

$$M_\infty = M_A \text{ and } K_\infty = K_A$$

and

$$\frac{\rho}{\rho_\infty} = \frac{1}{C_H \left(\frac{M_A}{M_H} - 1 \right) + 1} \quad (2)$$

Eliminating ρ/ρ_∞ from equations (1) and (2) one obtains, after some algebra,

$$C_H = \frac{\frac{(n_\infty - n)}{\rho_\infty K_\infty}}{\left[\frac{(n - n_\infty)}{\rho_\infty K_\infty} + 1 \right] \left(\frac{M_A}{M_H} - 1 \right) - \left(\frac{K_H}{K_A} - 1 \right)} \quad (3)$$

The quantity $K_\infty \rho_\infty$ in equation (3) is linearly dependent on pressure, and only slightly dependent on temperature and the wavelength of light used. A formula established by Biot and Arago expressing these dependencies and confirmed by more recent experiments (Reference 8) is

$$\rho_{\infty} K_{\infty} = n_{\infty} - 1 = \frac{n_0 - 1}{1 + \alpha_{\infty} T_{\infty}} p_{\infty}$$

where n_0 is the index of refraction at $T_{\infty} = 0^{\circ}\text{C}$, $p_{\infty} = 1 \text{ atm}$

α_{∞} is the coefficient of thermal expansion of the ambient gas in $^{\circ}\text{C}^{-1}$

T_{∞} is the ambient temperature in $^{\circ}\text{C}$

p_{∞} is the ambient pressure in atmospheres

Values of n_0 and α_{∞} required for this study were obtained from tables in Reference 8.

The above analysis pertains to an air/helium mixture. When N_2 bubbles are studied in an SF_6 environment, the subscripts H and A are simply replaced with subscripts N and S, respectively, and subscript ∞ and subscript S are identical. Values of all constants used are tabulated below.

Gases	P	M_A/M_H or M_S/M_N	α_{∞}	K_H/K_A or K_N/K_S	$\rho_{\infty} K_{\infty}$
Air/He	1/2	7.25	1.092	0.893	$1.33 \cdot 10^{-4}$
	1	7.25	1.092	0.893	$2.67 \cdot 10^{-4}$
	4	7.25	1.092	0.893	$1.068 \cdot 10^{-3}$
	8	7.25	1.092	0.893	$2.136 \cdot 10^{-3}$
	10	7.25	1.092	0.893	$2.67 \cdot 10^{-3}$
SF_6/N_2	10	5.22	1.092	1.98	$7.15 \cdot 10^{-3}$

4.1.3 Fireball Wake Interferometry Data Reduction

In addition to mean radial helium concentrations through the core of the vortex, radial helium concentrations at various positions through the fireball wake were extracted from the interferometry data. A free coordinate system and normalization only with respect to the wake edges were selected for averaging the wake data, commensurate with the approach used in the analysis of the data in the vortex body. The same procedure applied to both infinite fringe and finite fringe interferograms.

The coordinates were established in the following manner. An axis approximating the center of the wake was determined by eye and drawn longitudinally through the core of the vortex. The wake coordinate origin became defined by a line drawn normal to the wake axis through the vortex coordinate origin (where it was defined in Section 4.1.1.1). All cuts through the wake were parallel to this line (normal to the wake axis) and their locations were based on fractions of vortex diameter D below the wake origin.

Fringe numbers along these cuts were recorded in the same manner as described in Section 4.1.1.2. The fringe profiles for the same cuts were averaged over n interferograms using the edges and center as normalizing parameters, which resulted in symmetric averaged fringe profiles when n was sufficiently large. Since the axial symmetry condition was then satisfied, the previously discussed Abel inversion of the fringe shift equation could be applied to calculate radial mass concentrations.

4.2 SIZE/RISE DATA

Shadowgraph movies were utilized in this investigation primarily to study gross motions of the rising vortex such as size and rise. Only a limited amount of this information could be obtained with interferometry since that diagnostic is limited to obtaining data at one instant of time in each event. After acquisition and processing, each shadowgraph film was projected on a large sheet of paper where the outline of the vortex was traced frame by frame until the vortex disappeared from the field of view. Since only gross flow features appear on a shadowgraph frame (change of illumination proportional to the second derivative of density rather than directly with density as is the case with interferometry), distinct features such as saddle point and maxima could not be distinguished, but the outline of the edge could accurately be identified. While viewing the shadowgraph movies, it was possible to quite accurately establish a radial axis visually through the center of each event. The averaging of this size/rise data is outlined below:

Referring to Figure 10, one may define for the j^{th} frame of the i^{th} event

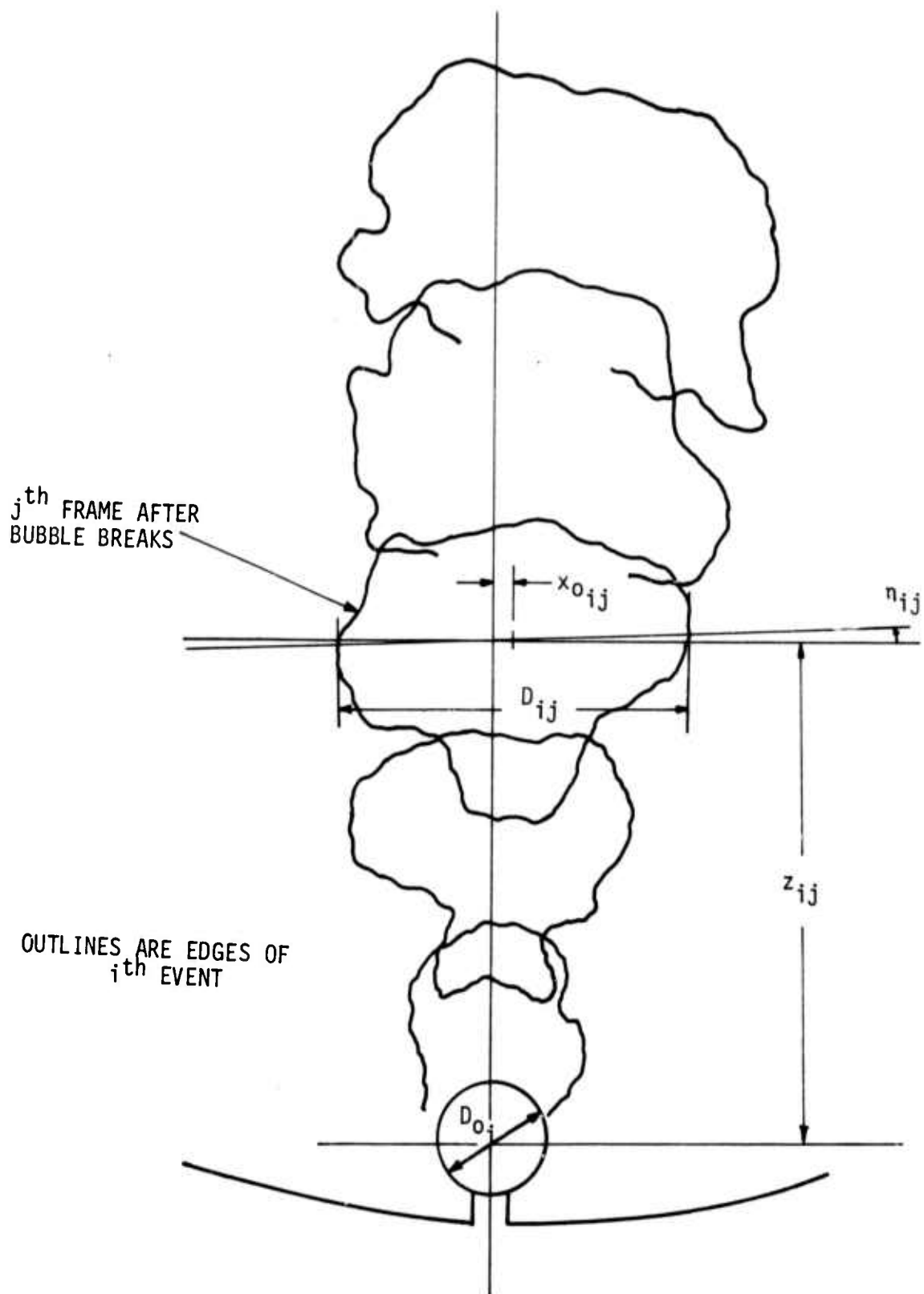


Figure 10. Nomenclature and Axes for Shadowgraph Data Reduction

z_{ij} = rise height from top of bubble tube

D_{ij} = diameter of center of vortex

η_{ij} = inclination of diameter to horizontal

x_{0ij} = horizontal displacement of center of vortex from center of bubble tube

D_{0i} = initial bubble diameter

$j = 1$ is the first frame after the bubble is broken

The following physical parameters are averaged over n events to yield average quantities for every j^{th} frame:

$$\left(\frac{\overline{z}}{\overline{D}_0}\right)_j = \frac{1}{n} \sum_{i=1}^n \frac{z_{ij}}{D_{0i}} \quad \text{mean normalized rise height}$$

$$\left(\frac{\overline{D}}{\overline{D}_0}\right)_j = \frac{1}{n} \sum_{i=1}^n \frac{D_{ij}}{D_{0i}} \quad \text{mean normalized diameter}$$

$$\overline{\eta}_j = \frac{1}{n} \sum_{i=1}^n \eta_{ij} \quad \text{mean rotation}$$

$$\left(\frac{\overline{x_0}}{\overline{D}_0}\right)_j = \frac{1}{n} \sum_{i=1}^n \frac{x_{0ij}}{D_{0i}} \quad \text{mean normalized translation of center of vortex from bubble tube axis}$$

Again, for a symmetric event, $\overline{\eta}_j$ and $\left(\frac{\overline{x_0}}{\overline{D}_0}\right)_j$ should approach zero as a check.

In addition, standard deviations, σ are computed for each parameter where σ for some parameter P is defined as

$$\sigma_{P_j} = \left[\frac{1}{n} \sum_{i=1}^n (P_{ij} - \overline{P}_j)^2 \right]^{1/2}$$

where

$$\overline{P}_j = \frac{1}{n} \sum_{i=1}^n P_{ij}$$

These same relationships applied equally well to the interferometry data and enabled data to be averaged at one point in time.

5. EXPERIMENTAL RESULTS

A discussion of results obtained in this subscale experimental study are presented in the following sections. These results include vortex size/rise comparisons from both interferometry and shadowgraph data, qualitative comparisons of the internal structure between laminar and turbulent vortices based on particle tracking photographs, selected mass concentration profiles from interferometry data, and a composite iso-concentration picture which presents the spatial distribution of low density gas within an averaged turbulent laboratory event.

5.1 VORTEX SIZE AND RISE RESULTS

Figure 11 presents vortex size/rise data obtained at eight different test conditions which provide over a factor of forty (40) variation in Reynolds number*. The vortex rise position, z , (given by the center of the cloud relative to the center of the initial bubble) is presented as a function of the vortex diameter, D . The results presented have been averaged over each data set at a given test condition (see Section 4.2 for the averaging technique used for calculating size/rise information) and made nondimensional using a characteristic length equal to the initial bubble diameter, D_0 .

The shadowgraph data (shown in solid symbols) provide results up to a rise position of about 5 bubble diameters since delineation of the vortex edge beyond a few bubble diameters, especially in laminar cases, was impossible. Additional data points are provided at higher rise positions by sets of averaged interferometry data (shown in open symbols). The results show a consistent trend with Reynolds number, namely, the higher Reynolds number data display a greater diameter at a given rise position. Of particular significance is that the size/rise data fall within two distinct bands; one corresponding to a high Reynolds number or "turbulent" group of data and the other to a low Reynolds number or "laminar" group.

*Reynolds number is defined as $Re = \rho_{\infty} u_T D_0 / \mu_{\infty}$ where u_T is the terminal velocity of a non-entraining sphere, D_0 is the initial bubble diameter, and ρ_{∞} and μ_{∞} are the ambient density and dynamic viscosity, respectively.

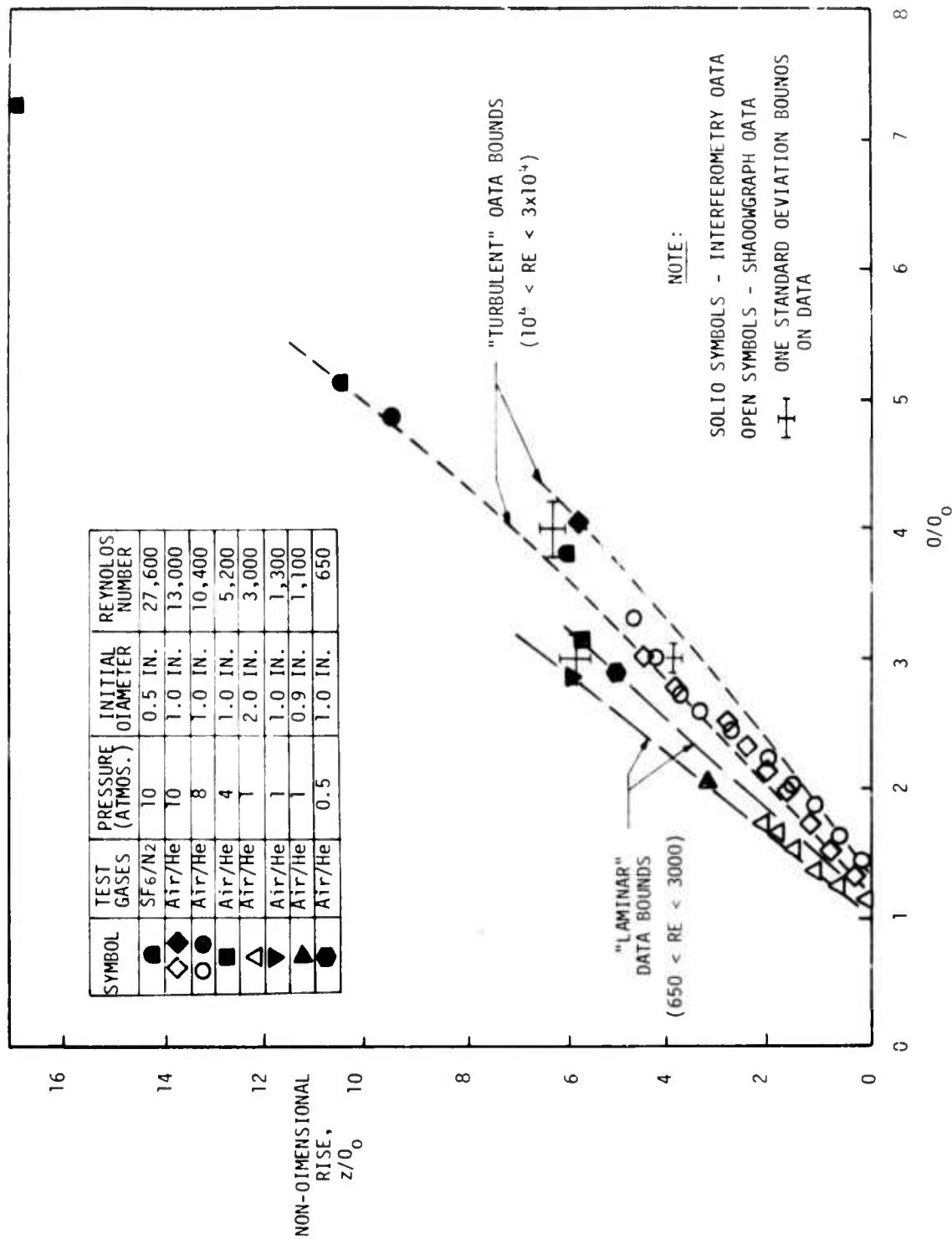


Figure 11. Mean Laboratory Size/Rise Data

The turbulent data band includes all data acquired with helium in air at tank pressures of 8 and 10 atmospheres and with nitrogen in sulfur hexafluoride (SF_6) at 10 atmospheres covering a range of Reynolds numbers from 10,400 to 27,600. The laminar data band encompasses all data acquired with helium releases in air at 1/2 and 1 atmosphere pressure and for initial bubble diameters ranging from 0.9 to 2 inches which provides Reynolds numbers ranging from 650 to 3000. Additional data were acquired at an intermediate Reynolds number of 5200 using a helium release in air at a tank pressure of 4 atmospheres. These data tended to fall between the laminar and turbulent bands and consequently were not added to the figure (except for an interferometry data point) to improve its clarity. These data are, however, tabulated with the other size/rise results in Table I. Mean rotational and translational data (η and x_0) at all test conditions were found to be negligible, as expected.

Also shown in Figure 11 are bars on the laminar and turbulent data which represent the standard deviations in the size and rise data at that stage of development. A complete summary of the size/rise standard deviations for both the shadowgraph and interferometry data are presented in Table II. These results are given for each set of averaged interferometry data and for the averaged shadowgraph data at rise heights of 2, 3, and 4 bubble diameters. In analyzing these variational data, it was found that there were no consistent trends with Reynolds number or stage of vortex development. Instead, all data showed a variation from the mean of 10 percent \pm 5 percent with few exceptions. In the exceptional cases, (shadowgraph data at 8 atmospheres and interferometry data at 1/2 and 1 atmosphere pressure) the standard deviations were within 20 percent of the mean. It should be emphasized that the standard deviations presented are for size and rise dimensions only, and in general, standard deviations of internal vortex characteristics such as the maximum fringe shift from the interferometry data tended to be somewhat larger.

In thoroughly reviewing the interferometry data, it was found that consistent variations in the configuration of the vortices (as viewed from the horizontal) were present as a function of Reynolds number. An additional subjective* dimension beyond those described in Section 4.1 was

*Subjective in that the base (bottom) of the vortex is in some cases difficult to establish because of the presence of the wake.

obtained from each interferogram to provide an estimate of the height (top to bottom dimension) of the vortex, not including the wake. An average vortex diameter-to-height ratio was then obtained for four individual sets of interferometry data to provide a first order means of determining the additional entrainment which occurred in the turbulent events relative to the laminar than would be indicated by only their respective diameters. These ratios are presented in the table below.

Average Diameter-to-Height Ratios of Events at Different Test Conditions

Test Condition	Reynolds Number	Diameter-to-Height Ratio
SF ₆ /N ₂ , 10 Atmospheres, D ₀ = 1/2 Inch	27,600	1.22
Air/He, 10 Atmospheres, D ₀ = 1 Inch	13,000	1.24
Air/He, 4 Atmospheres, D ₀ = 1 Inch	5,200	1.68
Air/He, 1 Atmosphere, D ₀ = 1 Inch	1,300	1.48

The results in the table indicate that the average diameter-to-height ratio for the turbulent events is about 20 percent less than for the laminar events or that the average volume of the turbulent events is about 20 percent greater than the volume of the laminar events for a given diameter. This difference in configuration results in a greater difference in entrainment between the laminar and turbulent results than indicated by their respective size/rise characteristics in Figure 11. In terms of an entrainment coefficient, $\alpha = \frac{dr}{dz}$, the rate of change of vortex radius with rise height (see discussion in Section 2 of Reference 1 for example) the difference between the turbulent and laminar data would be increased by about 6 percent.

A surprising result is the much greater flattening, or larger diameter-to-height ratios of the events in the 4 atmosphere group of data. This change in configuration could possibly be associated with the transitional nature of the flow since it is well known that many dramatic effects can occur in flow fields that are undergoing transition from a laminar to a turbulent condition. The net effect is that on a volume entrainment basis the 4 atmosphere set of data tends to shift and collapse with the laminar data.

Averaged laboratory fireball rise history data are presented in Figure 12. The same nondimensional rise position, Z/D_0 as presented in Figure 11 is plotted as a function of a nondimensional time parameter, $\tau = \sqrt{\frac{g}{D_0}} t$ where:

t is the fixed time for the events to reach an average rise height from the time the bubbles were broken

g is the gravitational acceleration

D_0 is the initial bubble diameter

Again it can be seen that low Reynolds number or laminar data fall within one group and the turbulent higher Reynolds number data fall into a distinctly different lower rise rate pattern. Curve fits to both the laminar and turbulent data are shown in the figure to better illustrate the more rapid rise rate of the laminar data. This faster rise rate exhibited by the laminar vortices results from a less pronounced entrainment of air in these events than in the turbulent events which is consistent with the size/rise and configuration data presented earlier.

Again the intermediate Reynolds number shadowgraph data acquired at 4 atmospheres pressure were not plotted to improve the clarity of the figure. In general, these data fall above but close to the turbulent data curve fit. In addition, three turbulent interferometry data points (two with SF_6/N_2 at 10 atmospheres and one with Air/He at 8 atmospheres pressure) at high rise positions were not shown so the scale of the plot could be expanded. These results follow the same trend as the turbulent data presented.

Further evidence of the marked differences in the structure and nature of the laboratory laminar and turbulent vortices beyond that already presented in terms of size, rise, and shape characteristics is displayed in two typical particle tracking photographs in Figures 13 and 14. These multiple exposure photographs of evolving particulate seeded vortices are presented for comparison purposes to illustrate dramatically the effect of turbulence on toroid structure. Figure 13 represents a laminar vortex taken at a pressure of one atmosphere with an initial bubble diameter of one inch corresponding to a Reynolds number of approximately 1300. The flash

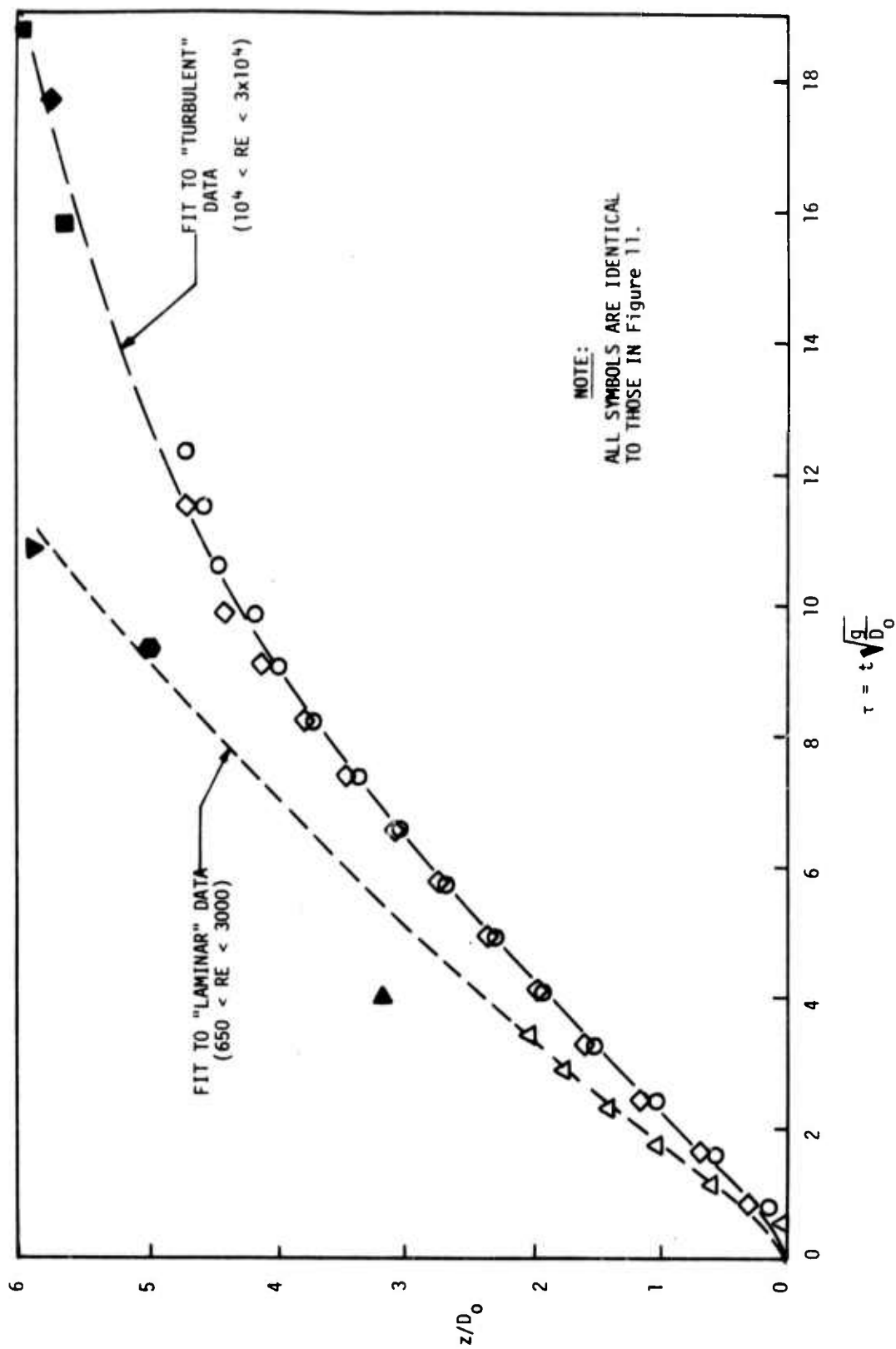


Figure 12. Laboratory Fireball Rise History

Reproduced from
best available copy.

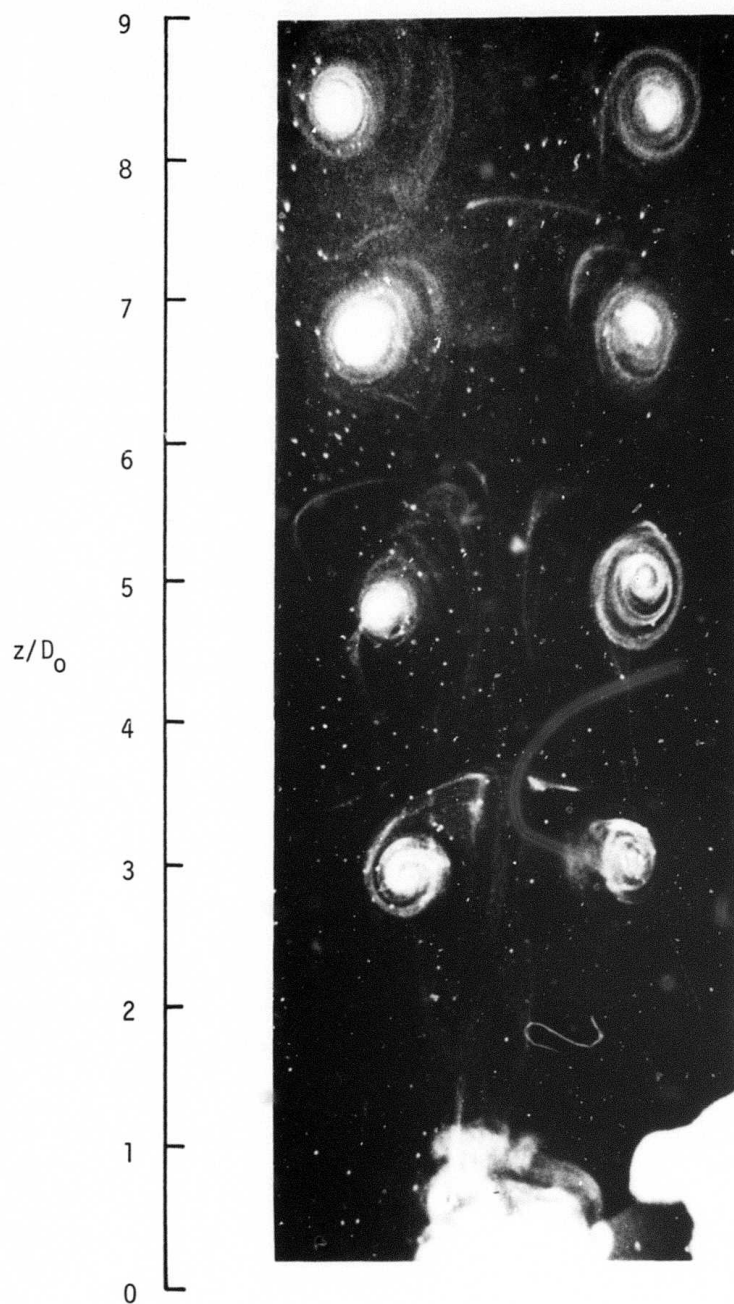


Figure 13. Multiple Exposure Photograph of Particulate Seeded Laminar Fireball

rate was 5.0 flashes per second. The important feature of this photograph is the distinct toroid "jelly-roll" structure apparent throughout the entire rise.

Figure 14 displays a turbulent event acquired at a pressure of eight atmospheres with the remaining test parameters identical to the one atmosphere photograph. The Reynolds number for this particular event was about 10,400. In this case, turbulent mixing has completely overwhelmed all internal structure evident in the laminar event. It is apparent from these and similar vortex structure photographs that a "jelly-roll" structure as such is strictly associated with a laminar event and will not exist in a full scale detonation.

5.2 COMPARISON OF TURBULENT LABORATORY DATA WITH FULL SCALE EVENT

It has been concluded that the higher Reynolds number ($Re \geq 10^4$) laboratory data are indeed turbulent. Since turbulent flows usually exhibit a weak dependence on Reynolds number, one would hope to find that the laboratory data could be scaled directly to full scale atmospheric events. Only two characteristic lengths present themselves; 1) the initial diameter of the fireball and 2) the atmospheric scale height. Since the laboratory experiments are not expected to be sensitive functions of the latter, one might hope that the initial diameter, D_0 , is sufficient for scaling. Figure 15 shows rise versus size data nondimensional with D_0 . The laboratory data which have factors of 2 variation in the initial size are nicely collapsed into a single curve as are the data of the full scale event whose initial diameter is approximately 10 times as large as the laboratory simulation. The results would appear to confirm that D_0 is the only important characteristic length and that the Reynolds number variation between full scale and laboratory conditions is not critical at least insofar as this type of gross dimensional data is concerned.

For the time dependence, the only obvious scaling is through the gravitational constant, g , which when coupled with the initial diameter, D_0 , can be made into a characteristic time. Figure 16 shows D/D_0 plotted against a nondimensional time $\tau = \sqrt{\frac{\rho_0}{\rho}} \sqrt{\frac{g}{D_0}} t$. The square root of the density

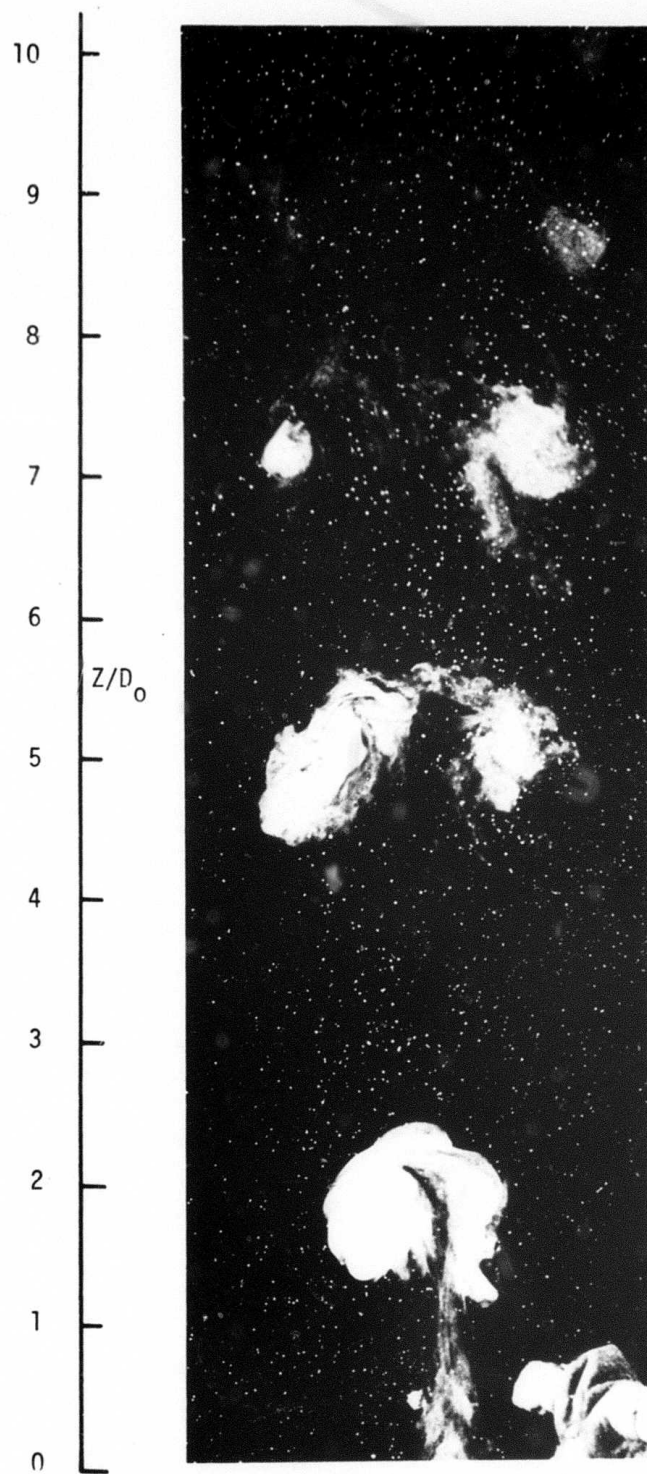


Figure 14. Multiple Exposure Photograph of Particulate Seeded Turbulent Fireball

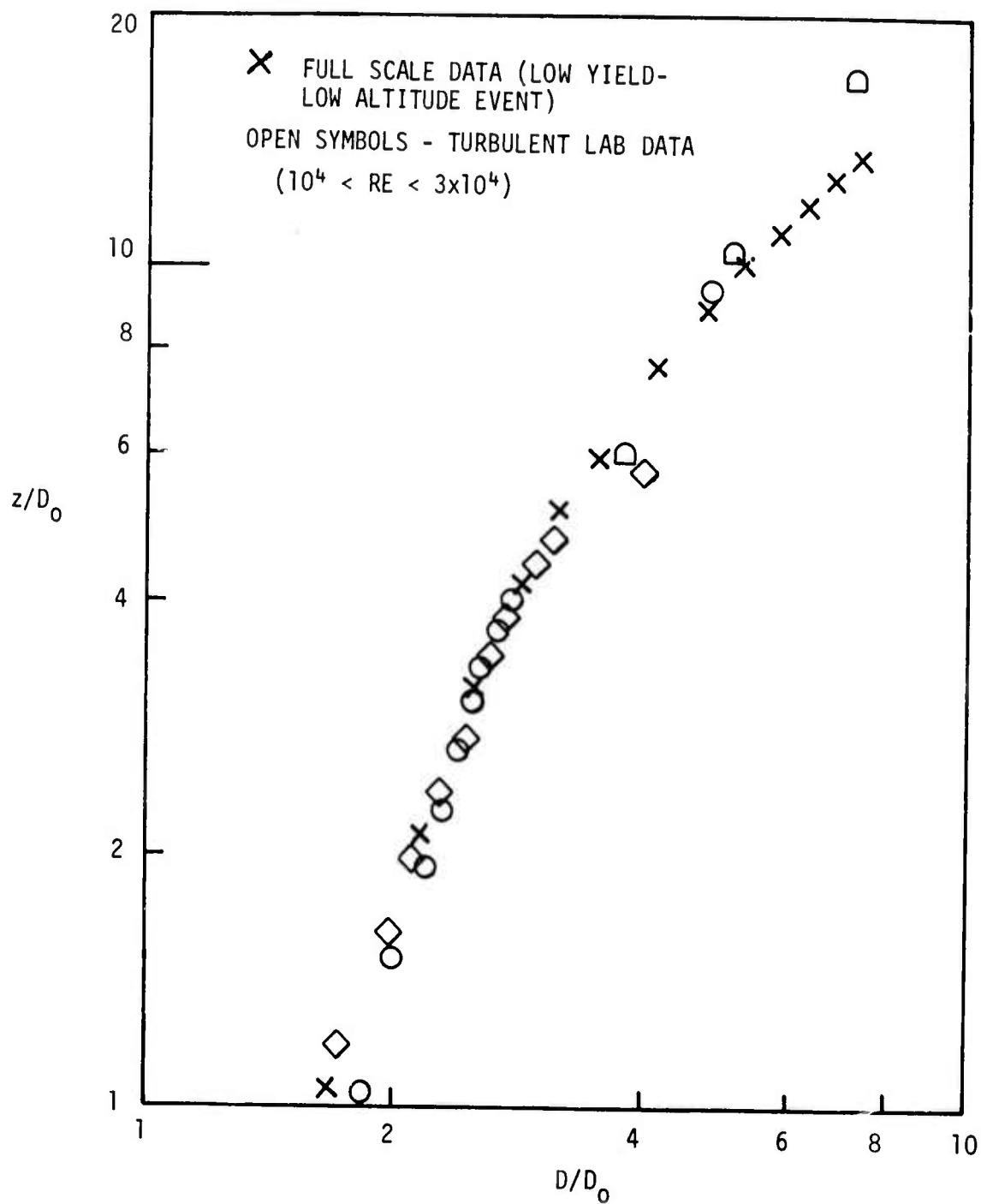


Figure 15. Comparison of Laboratory and Full Scale Fireball Size/Rise Data

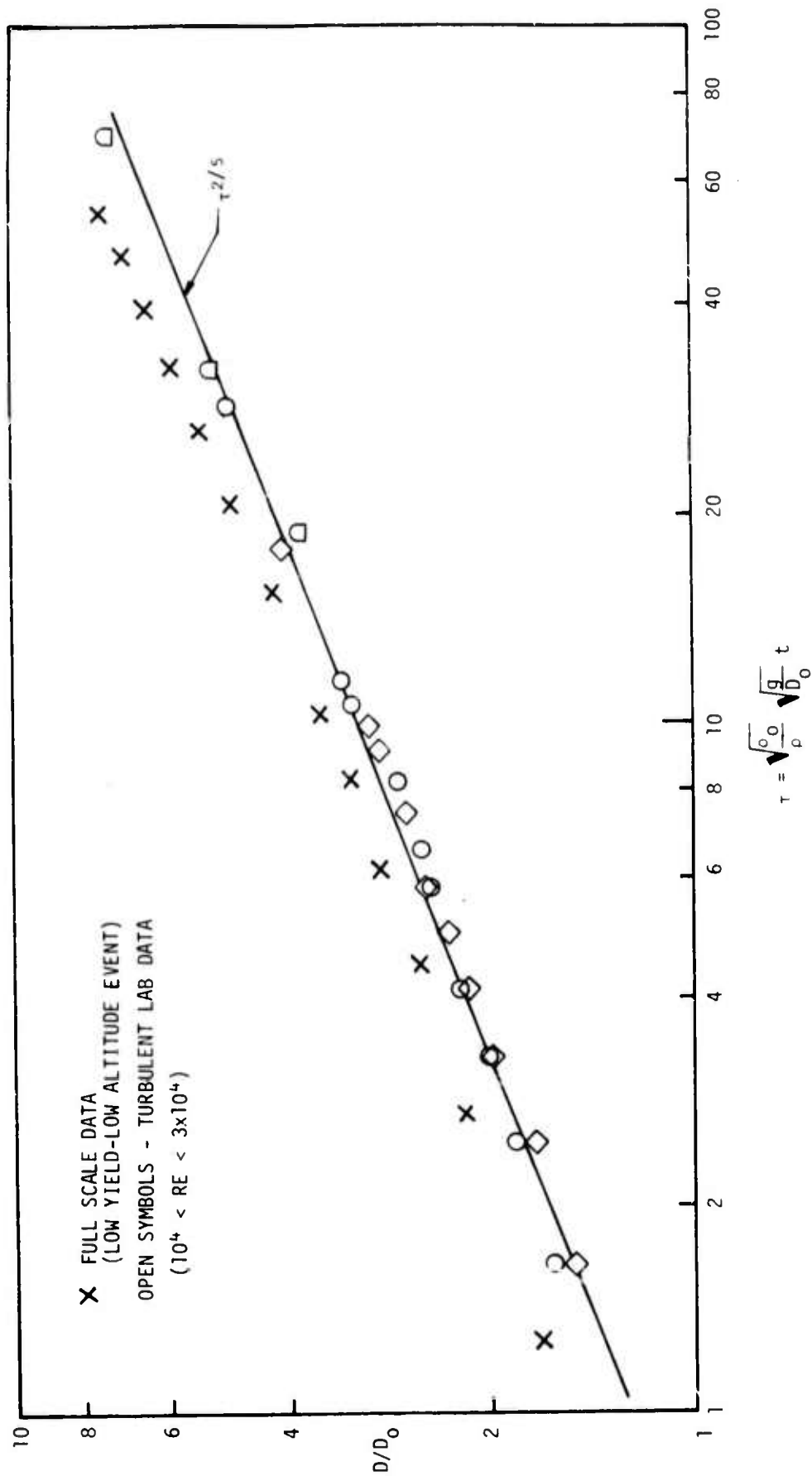


Figure 16. Comparison of Laboratory and Full Scale Fireball Size History Data

ratio has been included to account for the density variation resulting from the altitude change that the full scale event experiences (Reference 9). This ratio is identically 1 for all the laboratory data. All of the laboratory data are nicely correlated with these parameters and while the full scale data is slightly ($\sim 10\%$) displaced, nevertheless the trend is well established. In addition to agreeing with one another, all of the data are well represented by the formula $D/D_0 \sim \tau^{2/5}$ which can be shown to be a result of turbulent entrainment and the slowly varying toroidal geometry of the phenomena (Reference 9).

It is concluded that the laboratory data, when viewed in the proper nondimensional frame of reference are representative of a full scale atmospheric event, and reasonable credence can be placed in the concentration fields thus determined which are discussed in the subsequent sections.

5.3 LABORATORY FIREBALL MASS CONCENTRATION RESULTS

Four main topics are discussed in this subsection. A typical averaged fringe shift distribution is described which satisfies the axisymmetry requirement imposed by the data reduction method. Though Reynolds number dependence on mass concentration was not a primary objective of this study, a brief comparison between laminar and turbulent results is shown. Next, concentration distribution dependence on rise position (or equivalently, time after bubble bursting) and the geometric similarity that results are discussed in detail. Finally, mass concentration results within the laboratory fireball wake are discussed.

5.3.1 Results of Data Averaging

In Section 4.1.1, the technique used in this study to obtain a composite symmetric event by ensemble averaging a number of typically asymmetric fringe shift distributions was described. The mean distribution so obtained must satisfy the inherent requirement present in the data reduction of axisymmetry before it may be used to compute the density and mass concentration fields.

A representative mean fringe distribution obtained using the aforementioned averaging technique appears in Figure 17. The solid curve corresponds to the averaged left hand side, and the dashed curve to the mean right hand side. The particular test conditions at which these data were acquired were as follows: tank pressure of 10 atmospheres, 0.5 inch diameter initial N_2 bubble in an SF_6 environment, and a 10.4 initial bubble diameter rise 1.175 seconds after bubble breaking. The curves result from cuts taken through the center of the vortices.

It is seen by comparing the two curves that the averaged event is indeed reasonably axisymmetric. Edge radii and the radial locations of the fringe maxima deviate by less than 2 percent. The relative deviation in the fringe shift, S , is less than 10 percent at most. Prior to computing mass concentration profiles through an averaged event, the left and right hand side fringe shift distributions were averaged together to provide even a better representation of a symmetric event.

The discrete points appearing on Figure 17 correspond to raw fringe data taken directly from one of the twenty-nine interferograms which compose this particular set of data. These points are indicative of the asymmetries present in individual events and the necessary utilization of an averaging technique. It becomes readily evident from the differences between the two sides that an Abel inversion of fringe data from single events would produce misleading results.

5.3.2 Effect of Reynolds Number on Averaged Mass Concentration Profiles

Figure 18 compares a laminar mass concentration profile with one that is turbulent. Both profiles were reduced from data acquired at a common rise position and have their radial coordinates nondimensionalized with the initial bubble radii for comparison purposes. The laminar curve evolves from data recorded at test conditions of one atmosphere pressure, a one inch initial diameter helium bubble in an air environment, and at 0.55 seconds after bubble bursting. The turbulent data were acquired at 10 atmospheres pressure, using SF_6/N_2 as the gases, a 1/2 inch diameter initial bubble, and a time after bursting of 1.175 seconds. Both data

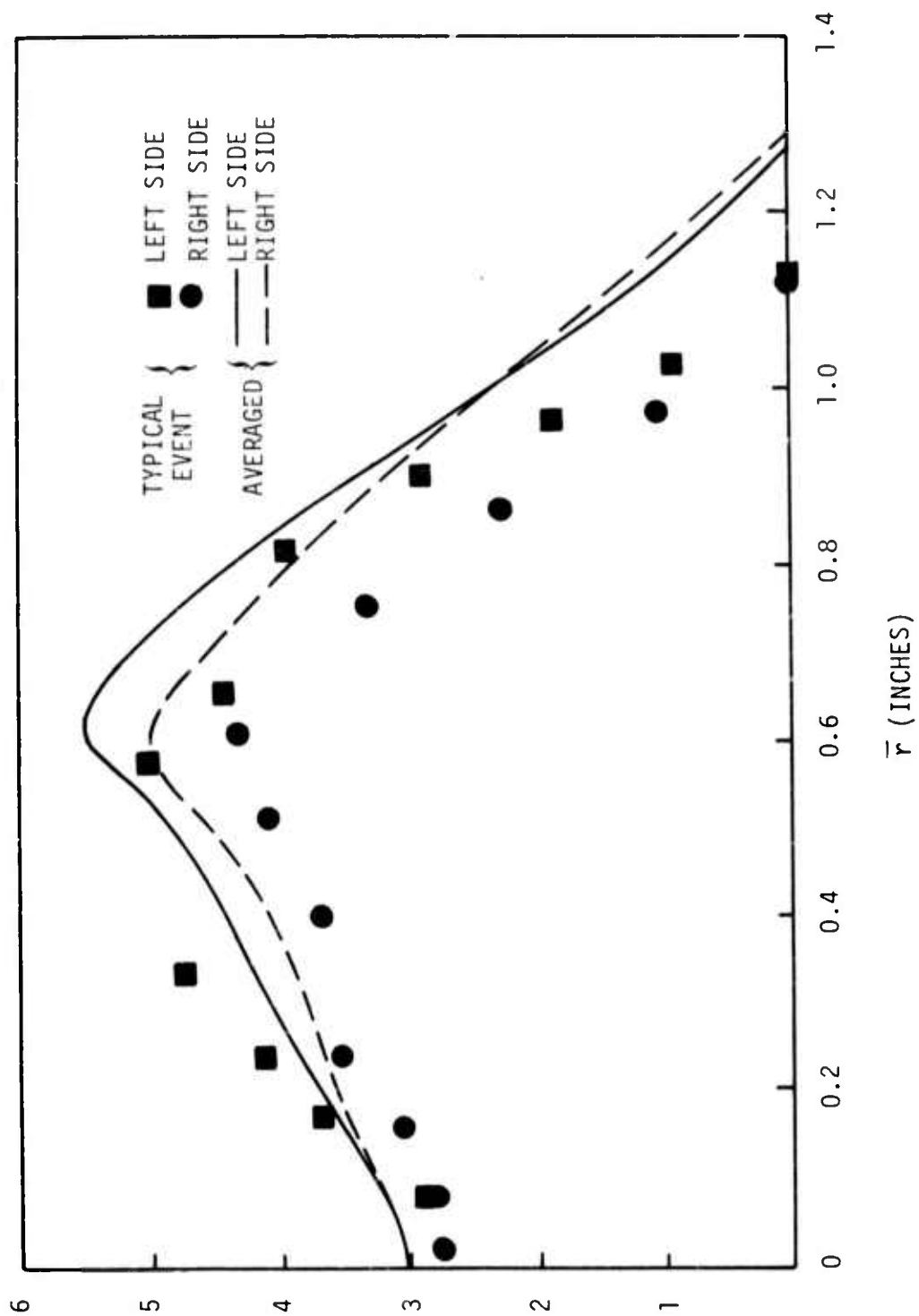


Figure 17. Averaged and a Typical Radial Fringe Shift Distribution

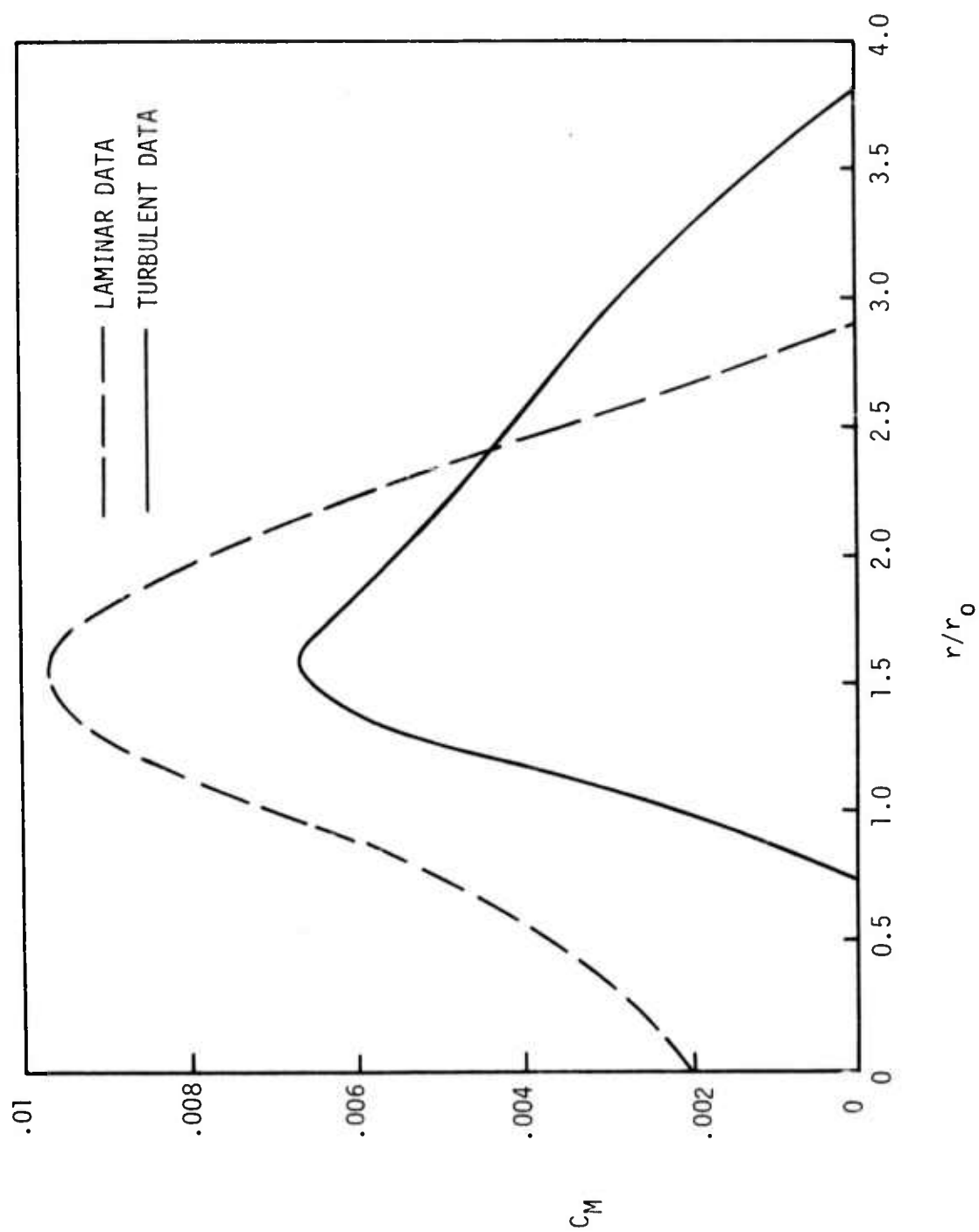


Figure 18. Mean Radial Mass Concentrations; Laminar and Turbulent Data at Same Rise Position ($\sim 6 D_0$)

sets were acquired at a rise position of approximately 6 initial bubble diameters. The Reynolds number of the turbulent data (27,600) is approximately 20 times that of the laminar (1300).

Two main features become evident from Figure 18. First is that the average laminar vortex is relatively smaller than that of the turbulent. Secondly, the stage of toroidal development of the turbulent case appears more advanced than that of the laminar. This is evidenced by the presence of a hole at the center of the turbulent vortex (see Appendix C). The turbulent toroid also exhibits more steep concentration gradients near the inner edge.

The fact that the turbulent profile has a lower peak mass concentration than the laminar is inconclusive. One cannot make a direct, one-to-one comparison between magnitudes since the initial density ratio of the laminar data (ratio of the density of pure helium to pure air) is 0.138 whereas that of the turbulent data is 0.192. These initial conditions, if anything, would tend to reduce the differences in the peak magnitudes.

For the sake of completeness, this comparison of laminar and turbulent mass concentration profiles was presented and discussed. Strong evidence that the turbulent data more closely resemble the full scale event, at least in structure and gross size/rise character (Section 5.2), motivates placing most of the emphasis in the remainder of Section 5 on the turbulent results, and only when additional insight may be gained will laminar results also be presented. To be complete, all data acquired during the course of the experiment appears in tabular form in Appendix E.

5.3.3 Effect of Rise Position (or Time) on Mass Concentration

A more conclusive comparison of mass concentration data than that presented in Section 5.3.2 results from data acquired at the same Reynolds number but at different rise positions (i.e., or different times). Three large repeat sets of SF_6/N_2 10 atmosphere data were acquired for this purpose at 6.0, 10.4, and 16.9 initial bubble diameters rise, or 0.625, 1.175, and 2.50 seconds after bubble bursting, respectively.

Figure 19 displays central cut mass concentration results for the data sets mentioned above. The radii have been nondimensionalized with the initial bubble radius, and all three curves have been plotted to the same radial scale so that relative vortex growth is illustrated. No attempt was made to locate vertical position of each plot to the scale of the horizontal dimension.

In this figure, the outer radius of the torus grows with rise position at a decreasing rate as rise position or time increases. This feature was evidenced in the size/rise discussions and need not be amplified here. More importantly, the peak concentrations decrease from 0.66 percent to 0.37 percent to 0.21 percent, their peaks become flatter, and their inner and outer concentration gradients decrease with increasing rise. Data pertaining to the growth of the inner torus radius (i.e., the hole in the center) is inconclusive, because what defines "hole" is somewhat ambiguous since the data reduction accuracy decreases with radius (see Appendix C).

Figure 20 compares the same data which appeared in Figure 19 but in a slightly different manner. Each mass concentration profile has been normalized to its own maximum concentration, and the radial coordinate has been normalized to the individual edge radius. In this manner, all three curves begin with a zero concentration ratio, increase to a ratio of one at its maximum, and decrease to zero at $r/r_{\text{edge}} = 1$. Figure 21 presents two different sets of laminar data in an identical fashion. These particular laminar data were acquired at one atmosphere pressure, with air/helium as gases, and at rise positions of 3.1 and 5.9 initial bubble diameters, respectively.

A comparison of the three curves in Figure 20 shows that there is very little difference at all between them, which is indeed a most interesting finding. This indicates that for all practical purposes, the mass concentration distribution in the torus remains geometrically similar after torus formation has been established for this range of rise positions. In the laminar case (Figure 21), though only two sets of data were analyzed and at comparatively lower rise positions, the same results bear credence.

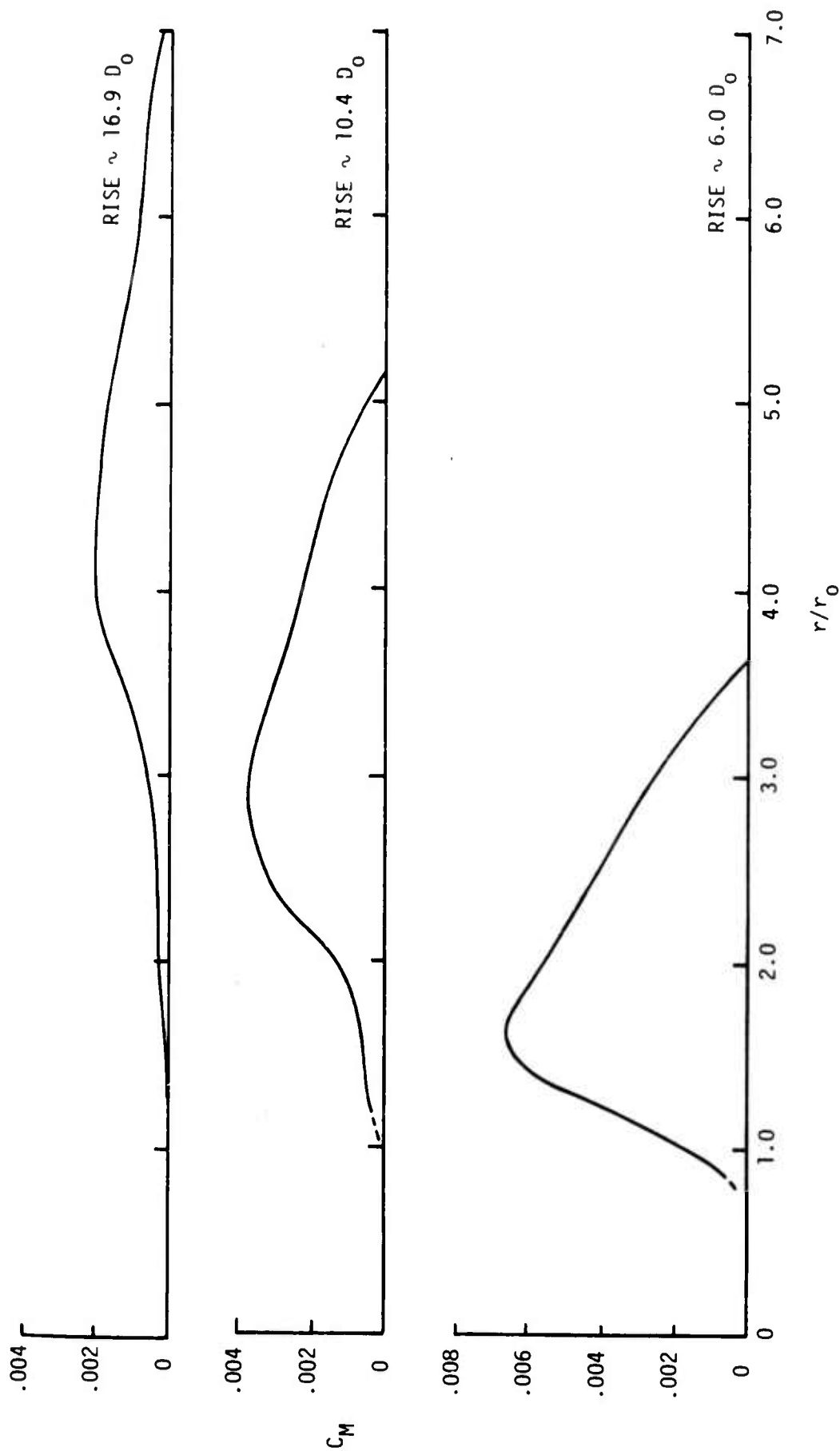


Figure 19. Averaged Radial Mass Concentration at Various Rise Positions; Turbulent Results

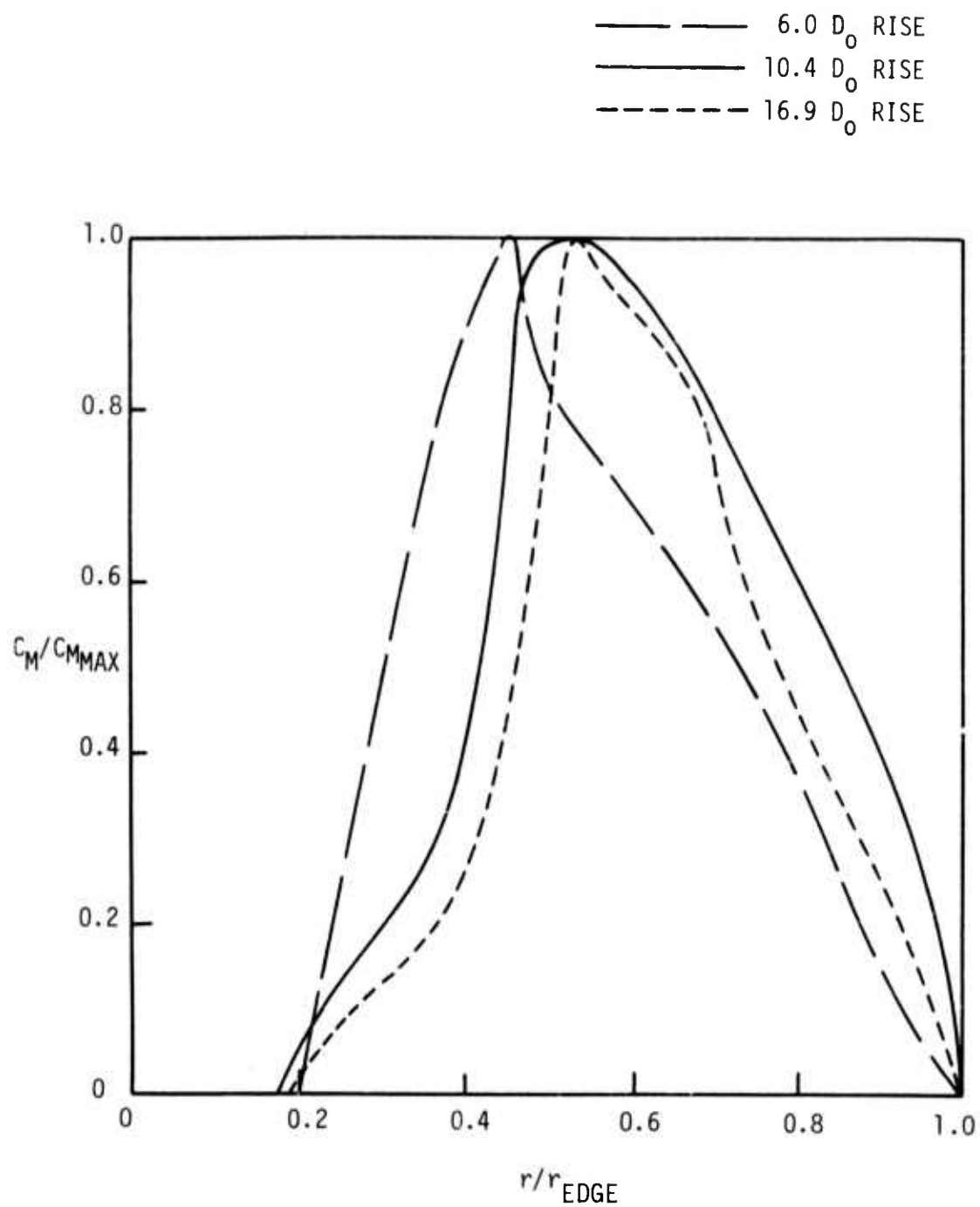


Figure 20. Normalized Mass Concentration Distributions;
Turbulent Data at Various Rise Positions

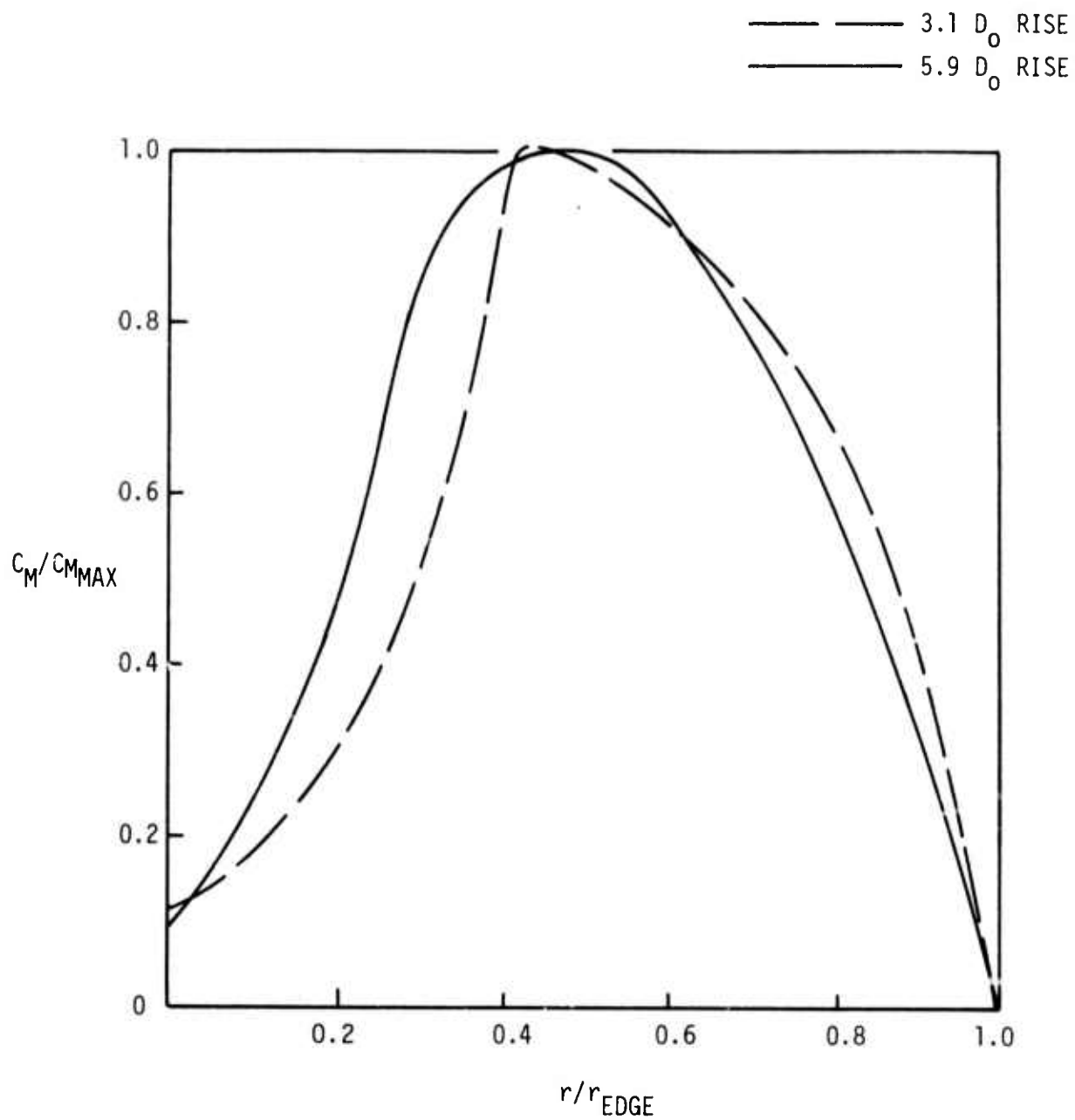


Figure 21. Normalized Mass Concentration Distributions;
Laminar Data at Two Rise Positions

5.3.4 Laboratory Fireball Wake Results

Two sets of data, one turbulent and one laminar, were analyzed to investigate the character of the laboratory fireball wake and to provide insight as to the significance of the wake in relation to the main vortex flow field.

An averaged, 10 atmosphere SF_6/N_2 vortex which rose 10.4 initial bubble diameters provided the data base for the turbulent wake calculations. Three cuts were made through the wake in the fashion outlined in Section 4.1.3 at $3/10 D$, $1/2 D$, and $3/4 D$ below the defined fireball coordinate origin. A physical constraint, namely the format size of the interferogram, precluded any analysis of data below $3/4 D$. The laminar wake results were ascertained from an averaged, one atmosphere, air/He set of interferograms. Since the laminar vortices were smaller than the turbulent ones, results were calculated along cuts at $1/2 D$, $3/4 D$, and D normal to the "wake axis."

Figure 22 provides nondimensional comparison between the turbulent results and those of the laminar. Mass concentrations along the various cuts through the wake, C_w , are divided by the maximum concentration along the central cut of its corresponding average vortex, $C_{v_{\max}}$. The radial position along the wake cut, r_w , is nondimensionalized by the initial bubble radius r_0 to suppress the effects of different initial bubble sizes (0.5 inch diameter for the turbulent, 0.4 inch for the laminar).

There are several wake characteristics that are illustrated in Figure 22 worthy of note. First, the turbulent wake, both relative to the initial bubble size and to its corresponding vortex size, is considerably wider than the laminar wake. Secondly, the peak wake concentration of the turbulent case is far less than that of the laminar, and remains reasonably constant throughout much of the width of the wake whereas the concentration of the low density gas in the laminar wake decreases rather steeply from its maximum to the edge.

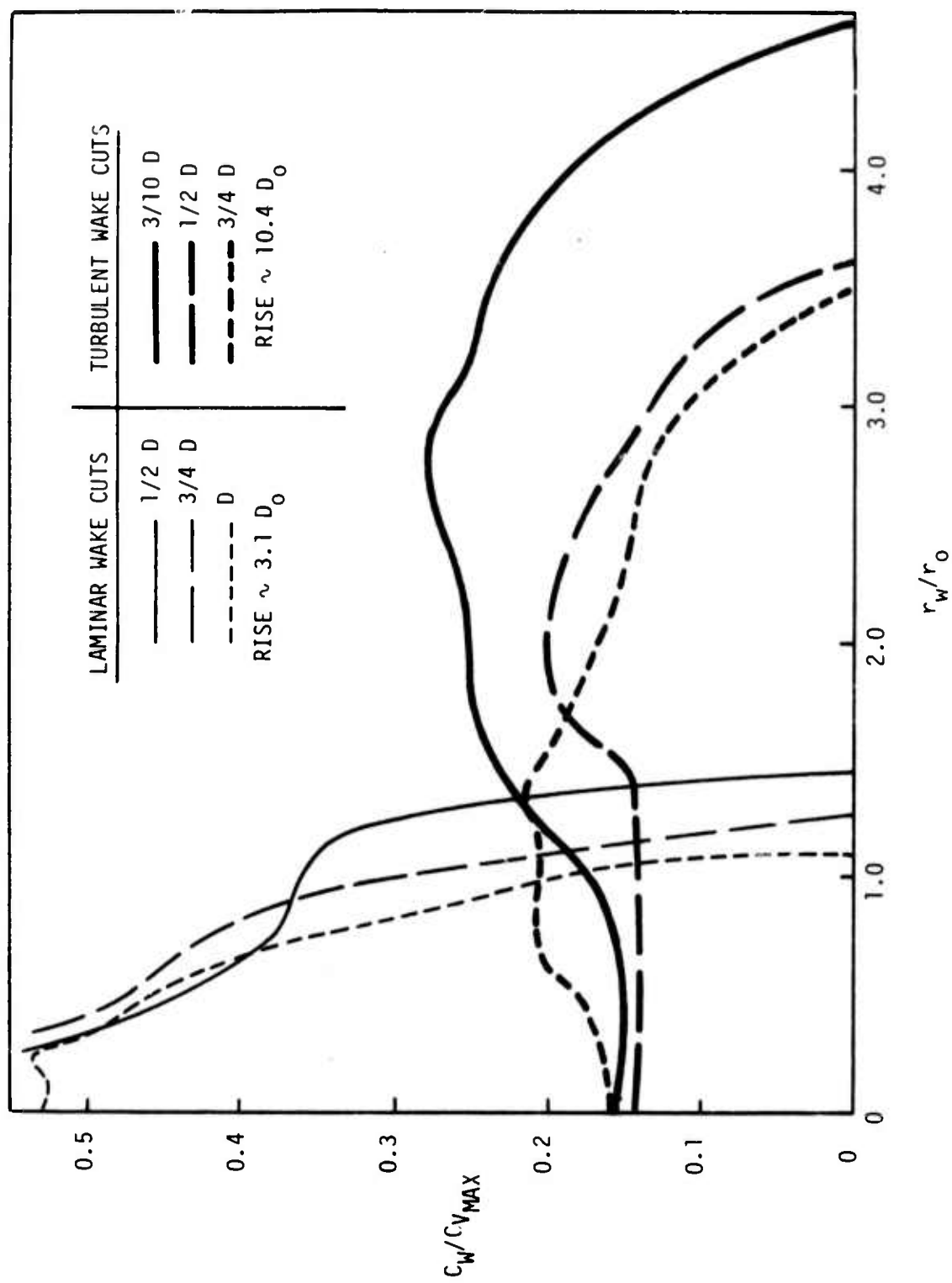


Figure 22. Averaged Wake Mass Concentration Distributions;
Laminar and Turbulent Data

A calculation presented in Appendix D and discussed more thoroughly in the following section indicates that slightly less than 10 percent of the nitrogen present in the vortex flow field is contained in the wake. To the degree of accuracy of the calculation made, this indicates that most of the initial mass does indeed remain in the vortex after torus formation has been established. One could reasonably extrapolate this result to a full scale nuclear event and conclude that the assumption that all weapon and carrier debris remains in the torus would appear to be, in the first approximation, valid.

5.4 COMPOSITE ISO-CONCENTRATION PICTURE FOR A TURBULENT VORTEX

Iso-concentration profiles for a turbulent vortex were derived from a series of averaged concentration profiles and are presented in Figure 23. The set of interferometry data which was used in preparation of this figure was obtained with an N_2 release in SF_6 at 10 atmospheres pressure after the center of the events rose a distance of 10.4 initial bubble diameters. The individual concentration profiles through the vortex body and wake are presented in Appendix E since they may be more useful in that form for comparison to code results. The concentration level corresponding to each iso-concentration profile is shown in Figure 23. The grid marks shown along the axes are 0.25 inches apart which corresponds to the initial bubble radius of this averaged event.

A calculation of the mass of nitrogen in the portion of the event shown was made (see Appendix D for details) which yielded a result equal to about 87 percent of the original N_2 in the unbroken soap bubble. It should not be inferred that 13 percent of the original mass is necessarily in the wake below the averaged event shown since the number of profiles used and the averaging necessary in the integration technique was only accurate to within about 10 percent. It was found that slightly over 90 percent of the calculated mass of N_2 was located in the vortex body or less than 10 percent of the total was located in the wake shown in Figure 23.

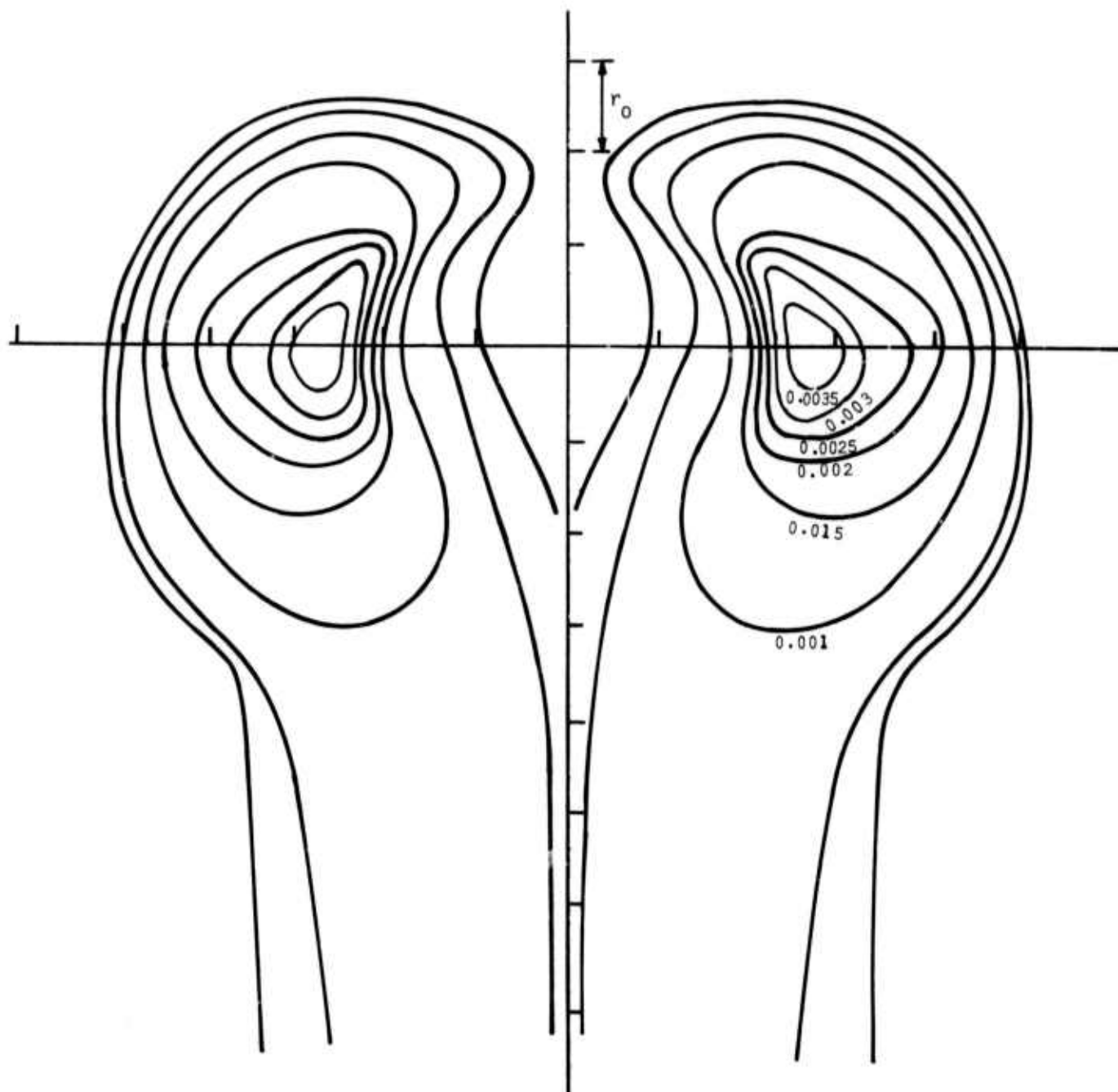
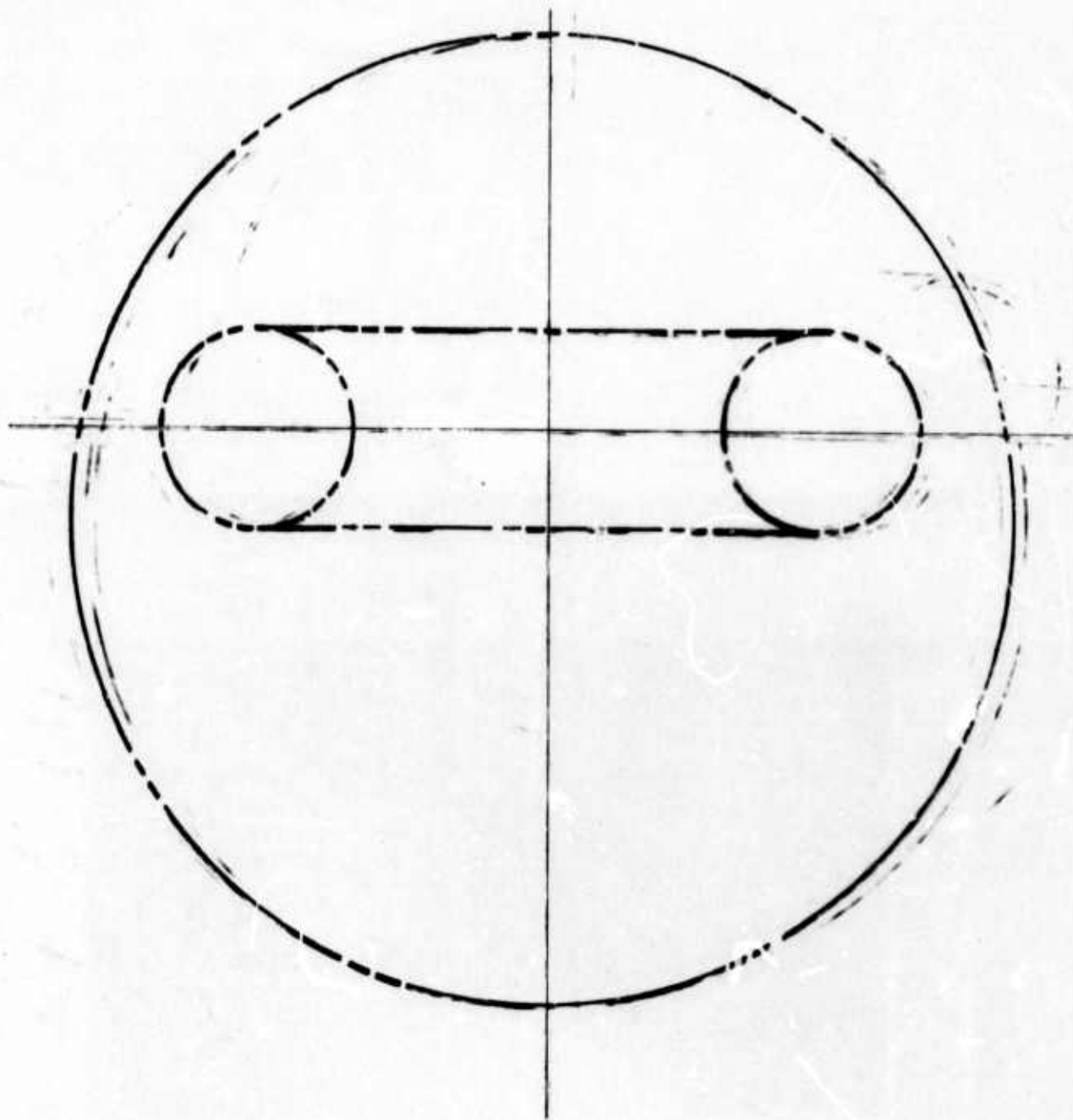


Figure 23. Iso-concentration Profiles for a Turbulent Vortex



64a

In rising over 10 bubble diameters the averaged vortex shown has entrained a mass of SF_6 more than 600 times greater than the mass of N_2 (Appendix D). As a result of this entrainment the iso-concentration lines range from a peak of slightly over 0.35 percent at the center of the vortex core to zero at the edge. It should be noted that the edge profile shown as a zero concentration line is an estimate only since defining the exact location of zero fringe shift is impossible. It is also interesting to note that the region defined by concentrations above 0.1 percent consists of a toroid with a kidney-shaped cross-section.

The largest mean concentration gradients can be seen to be on the outside top and sides of the vortex and on the inside of the torus near the core. Again it should be noted that the mean concentration profiles presented here have resulted from the averaging of 29 events and consequently instantaneous gradients at the edge of a single turbulent event would undoubtedly be greater.

A transparent overlay shows both a sphere which encompasses the bulk of the averaged event and a torus which provides a reasonable fit to the higher concentration level torus core. It can be seen that a sphere does provide a rough but fairly good representation of the volume contained in the vortex flow field with the primary exceptions being the depression and hole in the top and the wake structure aft of the torus. The torus shown in the overlay is geometrically similar to that described by geometric data from the same low yield-low altitude detonation discussed earlier in connection with Figures 15 and 16.

6. CONCLUSIONS

Listed below are the conclusions considered significant based upon results presented in Section 5.

1. Mean size/rise characteristics of turbulent and laminar events are distinctly different and fall into two well-defined bands. The turbulent data display a greater size for a given rise distance.
2. The larger diameter and different shape of the turbulent events reflect an increased rate of entrainment over that which exists in the laminar cases.
3. As a result of a decreased rate of entrainment, the laminar data exhibit a greater rise rate than the turbulent data.
4. Particle tracking photographs show a "jelly-roll" structure in toroids at low Reynolds number laminar conditions. Turbulent mixing and large scale turbulent structure completely overwhelm any wrap-up structure at the higher Reynolds number test conditions.
5. Laboratory turbulent size/rise data are in excellent agreement with data from a full scale detonation when results are viewed in the appropriate nondimensional frame of reference.
6. A nondimensional time parameter ($\tau = \sqrt{\frac{\rho_0}{\rho}} \sqrt{\frac{g}{D_0}} t$) has been shown to correlate laboratory and full scale fireball growth rate data. These data show that the fireball diameter is proportional to $\tau^{2/5}$.
7. Comparison of events at an identical Reynolds number but at different rise positions indicates that the peak concentration levels decrease, the peaks become less pronounced, and the concentration gradients decrease with increasing rise distance.
8. Concentration distributions in a rising vortex have for all practical purposes been shown to be geometrically similar after the toroid has become established (for a range of rise positions from 6 to 17 initial diameters).
9. A distinct wake is present below a rising toroid. However, it was found that at a high Reynolds number condition, less than 10 percent of the total mass was in the wake, or over 90 percent was present in the vortex body.

10. At the same high Reynolds number condition, it was found that a vortex entrained more than 600 times its original mass in rising a distance of about 10 initial bubble diameters.
11. The largest mean concentration gradients in an averaged turbulent vortex were found to be on the outside top and sides of the vortex and on the inside of the toroid near the core.
12. It has been found that for the same high Reynolds number condition that the higher concentration levels were located in a small kidney-shaped core.

7. RECOMMENDATIONS

The laboratory fireball data described in this report have provided for the first time a quantitative data base in terms of mean mass concentration and mean density field distributions for use in the checkout of hydrodynamic codes. Mean shadowgraph data along with interferometry data were ensemble averaged to provide laboratory size/rise characteristics. The high Reynolds number turbulent laboratory size/rise data are in very good agreement with data from a low yield, low altitude nuclear event which demonstrates that this experimental technique does simulate the important physics that controls fireball hydrodynamics. Strong evidence that the simulation is credible coupled with the need for quantitative data to support code calculations indicate that further subscale laboratory studies are justified. Data similar to that presented in this report could be produced in a very straightforward manner using the existing experimental facility and data analysis techniques. Direct turbulence measurements could be made through the addition of two primary diagnostic instruments.

Additional mean concentration/density data could be obtained without facility modification or development of new data analysis techniques. If further support is required for comparison to code results, more iso-concentration pictures (e.g., Figure 23) could be generated for various stages of vortex development. In addition, these pictures would provide better physical insight into the flow. These unique data, quantitative in nature, could be generated at either laminar or turbulent conditions, depending on the code development requirements.

An extension of the study would provide quantitative turbulence measurements, necessary to guide and provide inputs for the development of turbulent model equations for fireball flow fields. Direct density fluctuation and velocity fluctuation measurements could be made simultaneously with the addition of two diagnostic instruments. The density fluctuation measurements could be made using a small, fast response probe developed and successfully used at California Institute of Technology by Brown and Rebollo (Reference 12). A dual scatter, laser Doppler velocimeter (LDV) as used by Sullivan, et. al (Reference 13) could be incorporated into

the facility in order to measure two orthogonal velocity components of the vortices simultaneously. With these measured fluctuation quantities, the important turbulent transport terms in the Reynolds averaged momentum and thermal energy (and/or species) conservation equations, namely the turbulent Reynolds stresses and the turbulent heat or species fluxes are known. Thus, a two-dimensional transient solution of these conservation equations may be accomplished.

8. REFERENCES

1. Haigh, W. W. and Mantrom, D. D., "Fireball Entrainment Study," Semi-Annual Report, TRW Report No. 18895-6002-RO-00, DNA 2981Z, August 1972.
2. Haigh, W. W. and Mantrom, D. D., "Fireball Entrainment Study," Semi-Annual Report, TRW Report No. 18895-6003-RU-00, DNA 3139Z, May 1973.
3. Liepmann, H. W. and Roshko, A., Elements of Gasdynamics, New York: John Wiley and Sons, 1957.
4. Witte, A. B., "Three-Dimensional Flow Field Analysis by Holographic Photography and Interferometry," Final Technical Report, TRW Report No. 12414-6003-RO-00, 15 November 1969.
5. Witte, A. B. and Wuerker, R. F., "Laser Holographic Interferometry Study of High-Speed Flow Fields," AIAA Paper No. 69-347, AIAA 4th Aerodynamic Testing Conference, April 1969.
6. Witte, A. B., Fox, J., and Rungaldier, H., "Localized Measurements of Wake Density Fluctuations using Pulsed Laser Holographic Interferometry," AIAA Paper No. 70-727, AIAA Reacting Turbulent Flows Conference, June 1970.
7. Weyl, F. J., "Analytical Methods in Optical Examination of Supersonic Flow," NAVORD Report No. 211-45, Bur. Ordnance, Navy Department, 11 December 1945.
8. Forsythe, W. E., ed., "Smithsonian Physical Tables," 9th Edition, Tables 533-534, pages 532-533, 1954.
9. Lewis, J. E., Unpublished Analysis (Private Communication).
10. Wright, F. H., "The Particle Track Method of Tracing Fluid Streamlines," JPL-PR-3-23, 2 March 1951.
11. Goldstein, S., ed., Modern Developments in Fluid Dynamics, Volume II, New York: Dover Publications, Inc., 1965.
12. Brown, G. L. and Rebollo, M. R., "A Small, Fast-Response Probe to Measure Composition of a Binary Gas Mixture," AIAA Journal, Vol. 10, No. 5, pp. 649-652, May 1972.
13. Sullivan, J. P., Widnell, S. E. and Ezekiel, S., "A Study of Vortex Rings using a Laser Doppler Velocimeter," AIAA Paper No. 73-105.

Table I

Mean Vortex Size/Rise Data

Shadowgraph 2" Bubble 1 Atm. Re = 3000					Shadowgraph 1" Bubble 4 Atm. Re = 5200				
t (sec)	z/D ₀	D/D ₀	x ₀ /D ₀	η (deg)	t (sec)	z/D ₀	D/D ₀	x ₀ /D ₀	η (deg)
.0417	.064	1.130	-.006	.06	.0417	.251	1.385	-.008	-1.35
.0834	.600	1.223	.002	1.79	.0834	.632	1.540	-.020	-1.00
.1251	1.044	1.369	.041	2.75	.1251	1.037	1.606	-.028	-1.37
.1668	1.422	1.525	.056	.23	.1668	1.440	1.729	-.026	-.93
.2085	1.782	1.654	.059	1.52	.2085	1.804	1.831	-.030	-1.19
.2502	2.049	1.712	.050	3.29	.2502	2.217	1.958	-.020	-.20
					.2919	2.543	2.076	-.036	-.04
					.3336	2.915	2.225	-.011	.51
					.3753	3.278	2.275	-.031	.64
					.417	3.593	2.312	-.137	.14

Shadowgraph 1" Bubble 8 Atm. Re = 10,400					Shadowgraph 1" Bubble 10 Atm. Re = 13,000				
t (sec)	z/D ₀	D/D ₀	x ₀ /D ₀	η (deg)	t (sec)	z/D ₀	D/D ₀	x ₀ /D ₀	η (deg)
.0417	.138	1.418	-.001	.20	.0417	.286	1.301	-.002	-.35
.0834	.554	1.622	-.004	.37	.0834	.686	1.489	.008	-.08
.1251	1.038	1.830	-.008	.38	.1251	1.178	1.717	.04	.47
.1668	1.513	2.003	.009	.83	.1668	1.598	1.974	.018	.66
.2085	1.927	2.219	-.003	-.09	.2085	1.967	2.128	-.006	.73
.2502	2.294	2.316	-.061	.34	.2502	2.358	2.305	.005	2.58
.2919	2.683	2.434	-.087	1.41	.2919	2.731	2.483	.008	4.71
.3336	3.022	2.507	-.077	2.11	.3336	3.074	2.577	.030	5.16
.3753	3.347	2.575	-.067	2.12	.3753	3.441	2.639	.022	5.06
.417	3.732	2.722	-.051	1.84	.417	3.794	2.774	.054	4.98
.4587	4.004	2.813	-.047	2.92	.4587	4.142	2.914	.086	4.67
.5	4.182	3.026	0.	1.79	.5	4.426	3.001	.082	4.20
.5417	4.490	3.181	.008	2.2	.5417	4.505	2.959	.020	5.10
.5834	4.600	3.304	.065	3.11	.5834	4.730	3.162	.087	4.72

Table I (CTD)
Mean Vortex Size/Rise Data

Interferometry Data

Gases	P (Atm.)	D_0 (in.)	Re	t (sec)	z/D_0	D/D_0
Air/He	1/2	1.0	650	.48	5.01	2.88
Air/He	1	0.9	1100	.19	3.16	2.22
Air/He	1	1.0	1300	.55	5.92	2.85
Air/He	4	1.0	5200	.80	5.65	3.12
Air/He	8	1.0	10,400	1.44	9.44	4.84
Air/He	10	1.0	13,000	.90	5.76	4.04
SF_6/N_2	10	0.5	27,600	.63	5.99	3.80
SF_6/N_2	10	0.5	27,600	1.18	10.39	5.12
SF_6/N_2	10	0.5	27,600	2.50	16.8	7.26

Table II

Vortex Size/Rise Data - Standard Deviations σ Shadowgraph Data - Various Rise Positions $z/D_0 \sim 2$

Gases	P (Atm.)	D_0 (in.)	Re	z/D_0	σ_z	σ_D/D
Air/He	1	2.0	3000	2.049	.149	.120
Air/He	4	1.0	5200	2.011	.121	.144
Air/He	8	1.0	10,400	1.927	.200	.120
Air/He	10	1.0	13,000	1.967	.139	.120

 $z/D_0 \sim 3$

Air/He	4	1.0	5200	2.915	.131	.121
Air/He	8	1.0	10,400	3.022	.187	.087
Air/He	10	1.0	13,000	3.074	.107	.130

 $z/D_0 \sim 4$

Air/He	8	1.0	10,400	4.004	.170	.124
Air/He	10	1.0	13,000	4.142	.083	.117

Interferometry Data

Air/He	1/2	1.0	650	5.01	.137	.177
Air/He	1	0.9	1100	3.16	.192	.181
Air/He	1	1.0	1300	5.92	.028	.128
Air/He	4	1.0	5200	5.65	.097	.119
Air/He	8	1.0	10,400	9.44	.104	.066
Air/He	10	1.0	13,000	5.76	.083	.101
SF ₆ /N ₂	10	0.5	27,600	5.99	.093	.118
SF ₆ /N ₂	10	0.5	27,600	10.39	.213	.149

APPENDIX A

Characterization of Particle Path Dependence

To be an effective fluid tracer, particles must possess relatively low inertias and high drags to follow the streamlines accurately. At the same time, they must be sufficiently large to become visible under intense illumination. Particle tracking is particularly valuable to describe flow patterns not easily accessible to other, more standard methods of measurement. The utility of this method depends on the accuracy of streamline tracing desired.

Assuming negligible radial velocities and net external forces, and using Oseen's approximation for $C_D(Re)$, results from an analysis by Wright (Reference 10) show that the path dependence of a particle in a vortex may be characterized by a single parameter,

$$\lambda_0 = \frac{R_0}{V_0} \left(\frac{6\pi a \mu D'}{M'} \right)$$

where R_0 = initial position of particle from center of core of vortex

V_0 = initial fluid speed

a = radius of particle

μ = fluid viscosity

$D' = \text{drag parameter} = \frac{C_D Re}{24} = 1 + 0.1875(Re) - 0.0148(Re)^2 + \dots$
(Reference 11)

$M' = \text{apparent mass of particle} = \frac{4}{3} \pi a^3 (\rho_p + \frac{1}{2} \rho)$

ρ_p = density of particle

ρ = fluid density

A plot of this particle path dependence on parameter λ_0 from Reference 10 is presented in Figure A.1. It is evident that large λ_0 is desirable.

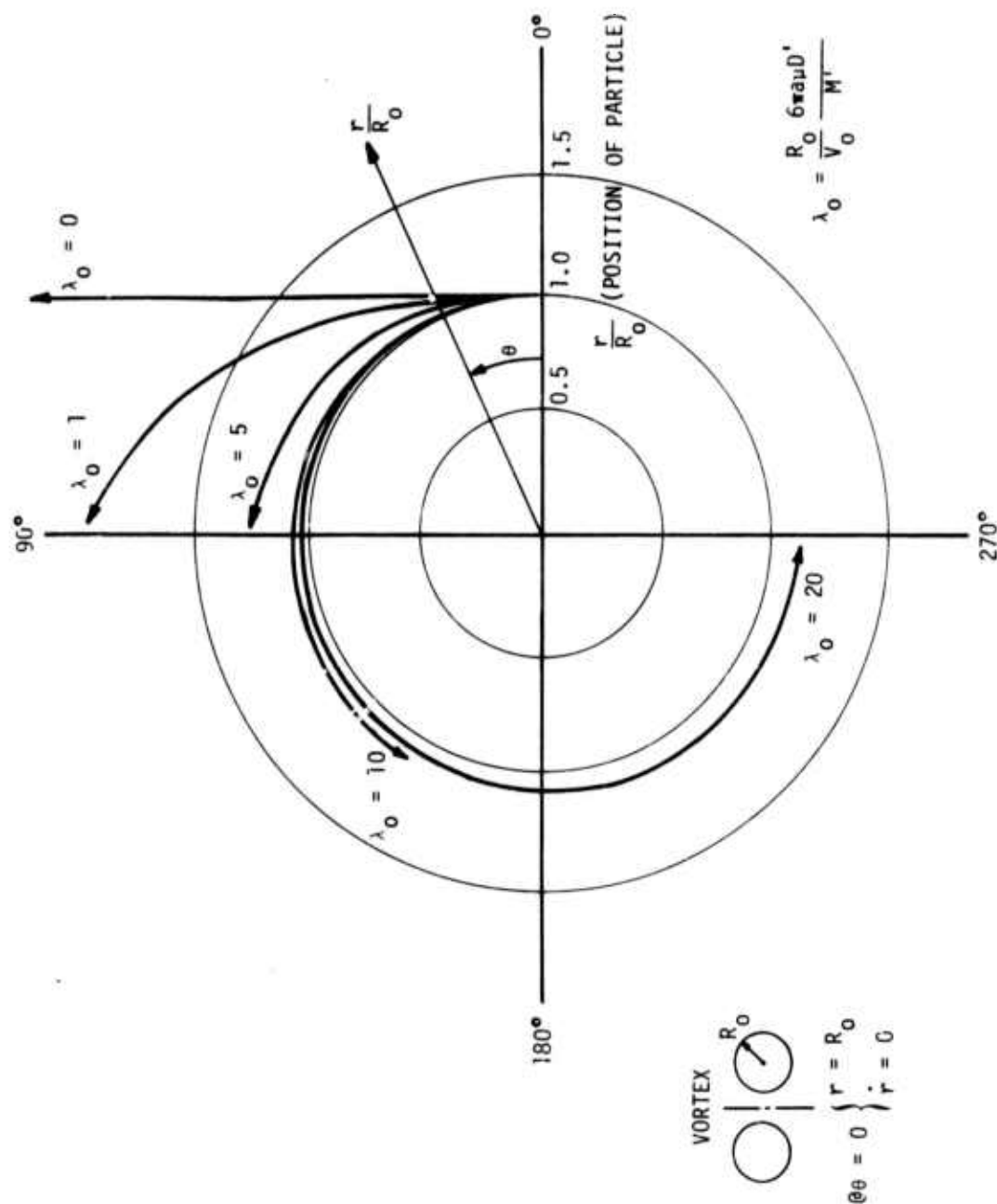


Figure A-1. Particulate Path Dependence on Parameter λ_0

For the particles used in this study, a value of λ_0 may easily be computed. An example is presented to illustrate what happens to a 100 micron diameter particle within a vortex having a core radius of 1 inch, a circumferential velocity of 1 ft/sec, and the fluid predominantly air at 1 atmosphere. The particle Reynolds number for this case is calculated to be 2, thus the drag parameter D' using Oseen's approximation is 1.33. For this particular case, $\lambda_0 \approx 14$ which based upon Figure A-1 is indicative of a very good tracer. Since D' increases strongly with Re whereas M' is very weakly dependent on Re , the particulate becomes a better tracer in the higher pressure regimes.

APPENDIX B

ABEL INVERSION OF THE AXISYMMETRIC FRINGE SHIFT EQUATION

The inversion of the integral equation

$$S(y) = \frac{2}{\lambda} \int_y^{r_0} (n - n_\infty) \frac{r dr}{(r^2 - y^2)^{1/2}} \quad (B-1)$$

for change in index of refraction $(n - n_\infty)$ expressed in terms of fringe shift S is by no means trivial, and the details of this inversion form the scope of this appendix.

Introduce $v = r^2$

$$u = y^2$$

Then,

$$S(u) = \frac{1}{\lambda} \int_u^{v_0} (n - n_\infty) \frac{dv}{\sqrt{v - u}} \quad (B-2)$$

Multiply both sides of (B-2) by $\frac{du}{\sqrt{u - w}}$ and integrate from w to v_0 .

$$\int_w^{v_0} \frac{S(u) du}{\sqrt{u - w}} = \frac{1}{\lambda} \int_w^{v_0} \frac{du}{\sqrt{u - w}} \int_u^{v_0} \frac{(n - n_\infty) dv}{\sqrt{v - u}} \quad (B-3)$$

Interchange the order of integration on the right hand side of (B-3) in the following manner (note the change in limits)

$$\int_w^{v_0} \frac{S(u) du}{\sqrt{u - w}} = \frac{1}{\lambda} \int_w^{v_0} (n - n_\infty) dv \int_w^v \frac{du}{\sqrt{(u - w)(v - u)}} \quad (B-4)$$

The integral $\int_w^{v_0} \frac{du}{\sqrt{(u-w)(v-u)}}$ may be evaluated by introducing a new variable of integration p such that

$$u = v + p(w - v)$$

Then the integral reduces to

$$\int_w^{v_0} \frac{du}{\sqrt{(u-w)(v-u)}} = \int_0^1 \frac{dp}{\sqrt{p(1-p)}} \quad (B-5)$$

Consider the definition of the Beta Function

$$B(m,n) = \int_0^1 u^{m-1} (1-u)^{n-1} du = \frac{\Gamma(m)\Gamma(n)}{\Gamma(m+n)}$$

In this case, from (B-5) it is seen that $m = n = \frac{1}{2}$, and since $\Gamma(\frac{1}{2}) = \sqrt{\pi}$ and $\Gamma(1) = 1$,

$$\int_w^{v_0} \frac{du}{\sqrt{(u-w)(v-u)}} = \pi$$

Thus,

$$\frac{\pi}{\lambda} \int_w^{v_0} (n - n_\infty) dv = \int_w^{v_0} \frac{S(u) du}{\sqrt{u-w}} \quad (B-6)$$

Now, $n - n_\infty$ may be obtained by differentiating both sides with respect to w and then applying the Leibnitz Rule.

$$\frac{d}{dw} \int_w^{v_0} (n - n_\infty) dv = \frac{\lambda}{\pi} \frac{d}{dw} \int_w^{v_0} \frac{S(u) du}{\sqrt{u-w}} \quad (B-7)$$

The left hand side of (B-7) becomes

$$\frac{d}{dw} \int_w^{v_0} (n - n_\infty) dv = -(n - n_\infty)_w \quad (B-8)$$

The right hand integral may be integrated by parts

$$\int_w^{v_0} \frac{S(u)}{\sqrt{u-w}} du = 2 S(u) \sqrt{u-w} \Big|_w^{v_0} - 2 \int_{S(w)}^{S(v_0)} \sqrt{u-w} dS$$

By definition, $S(v_0)$ is identically 0 so the first term is 0, and letting $dS = \frac{dS}{du} du$

$$(n - n_\infty)_w = \frac{2\lambda}{\pi} \frac{d}{dw} \int_w^{v_0} \sqrt{u-w} \frac{dS}{du} du \quad (B-9)$$

To evaluate the derivative of the integral, Leibnitz' Rule is again applied.

$$\frac{d}{dw} \int_w^{v_0} \sqrt{u-w} \frac{dS}{du} du = -\frac{1}{2} \int_w^{v_0} \sqrt{u-w} \frac{dS}{du} du$$

Therefore,

$$(n - n_\infty)_w = \frac{-\lambda}{\pi} \int_w^{v_0} \frac{\frac{dS}{du} du}{\sqrt{u-w}}$$

which may be equivalently written as

$$(n - n_\infty)_{r=y} = \frac{-\lambda}{\pi} \int_y^{r_0} \frac{\frac{dS}{dr} dr}{(r^2 - y^2)^{1/2}}$$

which is Equation (2) in Section 4.1.2.

APPENDIX C

EFFECT OF ERROR IN $\frac{dS}{dr}$ NEAR THE SINGULARITY IN THE ABEL INVERSION OF THE FRINGE SHIFT EQUATION

Motivated by the occasional appearance of slightly negative mass concentrations in the region near $r = 0$ (these were omitted in the plots but included in the tabulated results in Appendix E), an effort was undertaken to ascertain the origin of these physically unrealistic results. Consider Equation (3) in Section 4.1.2.2 with subscripts modified for gases SF_6/N_2 rather than air and helium.

$$C_N = \frac{\frac{-(n - n_\infty)}{\rho_\infty K_\infty}}{\left(\frac{n - n_\infty}{\rho_\infty K_\infty} + 1\right) \left(\frac{M_S}{M_N} - 1\right) - \left(\frac{K_N}{K_S} - 1\right)}$$

From the table at the end of Section 4.1.2.2,

$$\rho_\infty K_\infty = 7.15 \cdot 10^{-3}; \quad \frac{M_S}{M_N} = 5.22; \quad \frac{K_N}{K_S} = 1.98$$

For the 10 atmosphere 10.4 bubble diameter rise data, it was found that

$$8 \cdot 10^{-6} < (n_\infty - n) < 8 \cdot 10^{-5}$$

Thus,
$$10^{-3} < \frac{n_\infty - n}{\rho_\infty K_\infty} < 10^{-2}$$

And the $\frac{n - n_\infty}{\rho_\infty K_\infty}$ term in the denominator becomes negligible compared to 1.

Thus, for this case

$$C_H \sim (n - n_\infty)$$

Consider the equation

$$n - n_{\infty})_{r=y} = \frac{-\lambda}{\pi} \int_y^{r_e} \frac{\frac{dS}{dr} dr}{(r^2 - y^2)^{1/2}}$$

Typical values of $\frac{dS}{dr}$ (which in the data reduction are approximated by $\frac{\Delta S}{\Delta r}$) in the region near the singularity are approximately half a fringe in 0.1 inches; or about 5 fringes/inch. Suppose that locally there may be an error of ± 20 percent from the true $\frac{dS}{dr}$, which may be quite likely when one measures slope off of the reconstructed interferograms.

An error of 20 percent of 5 fringes per inch (i.e., 1 fringe/inch) would modify the original calculation the following way:

$$\begin{aligned} n - n_{\infty})_{r=y} &= \frac{-\lambda}{\pi} \int_y^{r_e} \frac{(\frac{dS}{dr} \pm 1) dr}{(r^2 - y^2)^{1/2}} \\ &= \frac{-\lambda}{\pi} \left[\underbrace{\int_y^{r_e} \frac{\frac{dS}{dr} dr}{(r^2 - y^2)^{1/2}}}_{\text{Original Calculation}} \pm \underbrace{\int_y^{r_e} \frac{dr}{(r^2 - y^2)^{1/2}}}_{\text{Error}} \right] \end{aligned}$$

Once the integral on the right is evaluated, the incurred error in $(n - n_{\infty})$ becomes

$$\mp \frac{\lambda}{\pi} \log \left(\frac{2r_e}{y} \right)$$

This indicates that the error in C_H introduced by an error in $\frac{dS}{dr}$ of 1 fringe/inch is directly proportional to $\log \left(\frac{2r_e}{y} \right)$. A table of this error as a function of r/r_e appears below:

y/r_e	r/r_o		$\log \left(\frac{2r_e}{y} \right)$
0	0	(center)	∞
0.05	.256		3.689
0.1	.512		2.996
0.2	1.024	(~ inner edge)	2.303
0.5	2.56	(~ peak C_M)	1.386
1.0	5.12	(outer edge)	.693

For very small y , that is, for a calculation made for a point near the origin, the error induced by an error in slope becomes large indeed. When the calculation is made at points further away from the origin (larger y), the error is less pronounced. It was found that an error in slope of ± 1 fringe was indeed sufficient to make the calculated negative mass concentration positive. In this report, negative concentrations near the vortex origin are ignored, concentrations in that region are just considered negligible.

APPENDIX D

CALCULATION OF MASS OF A LABORATORY FIREBALL

D-1. MASS OF LOW DENSITY GAS

This calculation was undertaken to compare the amount of nitrogen present in an analyzed toroid to that in the unbroken bubble. It accomplishes two purposes; first, it tests the validity of Figure 23, and second, gives the relative amounts of mass in both the vortex and the wake.

From Dalton's Law of Partial Pressures,

$$p_N + p_S = \frac{\rho_N}{M_N} + \frac{\rho_S}{M_S} = \frac{\rho_\infty}{M_S}$$

where p_N and p_S are the partial pressures of N_2 and SF_6 respectively, and ρ_N and ρ_S are the densities of N_2 and SF_6 in the disturbed region. This equation utilizes the facts that pressure and temperature are constant everywhere and that the ambient medium is composed of pure SF_6 . Multiplying through by M_S , we get

$$\frac{M_S}{M_N} \rho_N + \rho_S = \rho_\infty \quad (D-1)$$

The density in the mixed gas region is equal to the sum of the densities of N_2 and SF_6 since the volume is fixed. Thus,

$$\rho_N + \rho_S = \rho \quad (D-2)$$

Replacing ρ_S in (D-1) with $\rho - \rho_N$ from (D-2) and integrating over the known volume, the mass of nitrogen within the volume becomes

$$m_N = \frac{\rho_\infty}{\frac{M_S}{M_N} - 1} \int \left(1 - \frac{\rho}{\rho_\infty}\right) dV \quad (D-3)$$

The mass of the spherical, initially pure nitrogen bubble is

$$m_{N_0} = \frac{4}{3} \pi r_0^3 \rho_{N_0}$$

where r_0 is the bubble radius and ρ_{N_0} is the density of pure nitrogen. This may be modified to

$$m_{N_0} = \frac{4}{3} \pi r_0^3 \frac{M_N}{M_S} \rho_\infty \quad (D-4)$$

The ratio between the calculated mass and the initial mass becomes

$$\frac{m_N}{m_{N_0}} = \frac{3}{1 - \frac{M_N}{M_S} \frac{4}{3} \pi r_0^3} \int \left(1 - \frac{\rho}{\rho_\infty}\right) dV \quad (D-5)$$

Consider now the integral $\int \left(1 - \frac{\rho}{\rho_\infty}\right) dV$. Break up the volume into M thin cylindrical volumes each having thickness Δy_i . Bearing in mind that the volume of any cylinder may be expressed as $2\pi\Delta y \int_0^{r_e} r dr$, where r_e is the edge radius, the integral in question may be expressed in terms of a sum of integrals each over a cylindrical volume;

$$I = \int \left(1 - \frac{\rho}{\rho_\infty}\right) dV = 2\pi \sum_{i=1}^M \Delta y_i \int_0^{r_e} \left(1 - \frac{\rho}{\rho_\infty}\right) r dr \quad (D-6)$$

or

$$I = 2\pi \sum_{i=1}^M \Delta y_i r_{e_i}^2 \int_0^1 \left(1 - \frac{\rho}{\rho_\infty}\right) \left(\frac{r}{r_e}\right) d\left(\frac{r}{r_e}\right)$$

Now, break the integral over r/r_e into N equal zones (each j^{th} volume having the same number of zones),

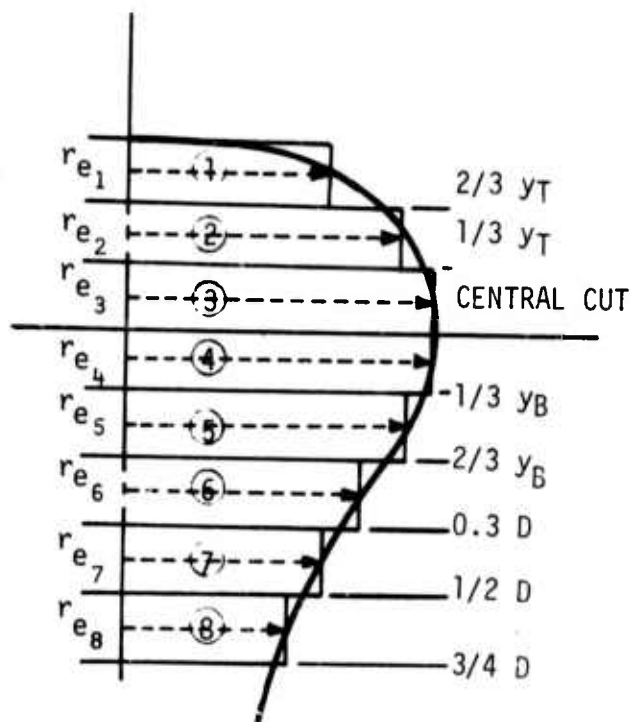
$$I = 2\pi \sum_{i=1}^M \Delta y_i r_{e_i}^2 \sum_{j=1}^N \left(1 - \frac{\rho}{\rho_{\infty}}\right)_j \left(\frac{j}{N}\right) \left(\frac{1}{N}\right)$$

$$I = \frac{2\pi}{N^2} \sum_{i=1}^M \Delta y_i r_{e_i}^2 \sum_{j=1}^N j \left(1 - \frac{\rho}{\rho_{\infty}}\right)_j \quad (D-7)$$

Finally, from (D-5) and (D-7),

$$\frac{m_N}{m_{N_0}} = \frac{3}{2N^2 \left(1 - \frac{M_N}{M_S}\right) r_0^3} \sum_{i=1}^M \Delta y_i r_{e_i}^2 \sum_{j=1}^N j \left(1 - \frac{\rho}{\rho_{\infty}}\right)_j \quad (D-8)$$

The 10.4 diameter rise SF_6/N_2 data were used for this example. A total of eight cuts (at $y = 2/3 y_T$, $1/3 y_T$, central, $1/3 y_B$, $2/3 y_B$ and wake cuts at $3/10 D$, $1/2 D$, and $3/4 D$) along which $\frac{\rho}{\rho_{\infty}}$ were known were used in the calculation. The following geometry was used:



The values of r_{e_i} and Δy_i are given below:

$$r_{e_1} = \frac{4}{5} r(2/3 y_T) \quad \Delta y_1 = 1/3 y_T$$

$$r_{e_2} = \frac{r(2/3 y_T) + r(1/3 y_T)}{2} \quad \Delta y_2 = 1/3 y_T$$

$$r_{e_3} = \frac{r(1/3 y_T) + r(CC)}{2} \quad \Delta y_3 = 1/3 y_T$$

$$r_4 = \frac{r(CC) + r(1/3 y_B)}{2} \quad \Delta y_4 = 1/3 y_B$$

$$r_5 = \frac{r(1/3 y_B) + r(2/3 y_B)}{2} \quad \Delta y_5 = 1/3 y_B$$

$$r_6 = \frac{r(2/3 y_B) + r(0.3 D)}{2} \quad \Delta y_6 = 0.3 D - 2/3 y_B$$

$$r_7 = \frac{r(0.3 D) + r(1/2 D)}{2} \quad \Delta y_7 = 0.2 D$$

$$r_8 = \frac{r(3/4 D) + r(1/2 D)}{2} \quad \Delta y_8 = .25 D$$

also, $r(CC) = 1/2 D$.

The density field at the middle of each zone is approximated by the average of the known density field along its upper and lower boundaries of each zone (see Appendix E). The density in the top zone is approximated as 4/5 of the density along the $2/3 y_T$ cut.

The total mass was calculated to be 86.4 percent of the initial mass which, taking into account the approximations made for this calculation, augments the credibility of Figure 23. Furthermore, the relative amounts of mass within each zone were:

Zone 1	.0498	
Zone 2	.1318	
Zone 3	.2009	
Zone 4	.1986	
Zone 5	.1564	
Zone 6	.1695	
Zone 7	.0535	} Fireball Wake
Zone 8	.0395	

These results indicate that only 9.3 percent of the total mass calculated within the cloud is present in the wake.

D-2. MASS OF ENTRAINED AMBIENT GAS IN FIREBALL

Having the mass of nitrogen in the mixed gas region, it was a simple matter to calculate the mass of entrained SF_6 .

The mass of entrained SF_6 in the flow field is just the total mass less the mass of nitrogen;

$$m_S = m_T - m_N \quad (\text{D-9})$$

The total mass is the density, ρ , integrated over the volume,

$$m_T = \int \rho dV = \rho_\infty \int \frac{\rho}{\rho_\infty} dV = \rho_\infty \left\{ \int dV - \int \left(1 - \frac{\rho}{\rho_\infty}\right) dV \right\} \quad (\text{D-10})$$

The integral $\int \left(1 - \frac{\rho}{\rho_\infty}\right) dV$ was calculated in Appendix D.

The volume is simply

$$\int dV = \pi \sum_{i=1}^M r_{e_i}^2 \Delta y_i \quad (\text{D-11})$$

Thus, m_T is known. Knowing m_N and m_{N_0} from D-1, the ratio of the entrained mass to the initial low density mass may be calculated.

The result was that approximately 600 times the initial mass was entrained at the time the center of the event rose to 10.4 initial bubble diameters.

APPENDIX E

TABULATED MEAN CONCENTRATION DATA

P (Atm)	Gases	t (sec)	D ₀ (in.)	z/D ₀	D/D ₀	Re	Cut	Page
1/2	Air/He	0.48	1.0	5.01	2.88	650	Central	83
1	Air/He	0.19	0.9	3.16	2.22	1100	Central	84
1	Air/He	0.19	0.9	3.16	2.22	1100	1/2 D Wake	85
1	Air/He	0.19	0.9	3.16	2.22	1100	3/4 D Wake	86
1	Air/He	0.19	0.9	3.16	2.22	1100	D Wake	87
1	Air/He	0.55	1.0	5.92	2.85	1300	Central	88
4	Air/He	0.80	1.0	5.65	3.12	5200	Central	89
8	Air/He	1.44	1.0	9.44	4.84	10,400	Central	90
10	Air/He	0.90	1.0	5.76	4.04	13,000	Central	91
10	SF ₆ /N ₂	0.68	0.5	5.99	3.80	27,600	Central	92
10	SF ₆ /N ₂	1.18	0.5	10.39	5.12	27,600	Central	93
10	SF ₆ /N ₂	1.18	0.5	10.39	5.12	27,600	2/3 y _T	94
10	SF ₆ /N ₂	1.18	0.5	10.39	5.12	27,600	1/3 y _T	95
10	SF ₆ /N ₂	1.18	0.5	10.39	5.12	27,600	1/3 y _B	96
10	SF ₆ /N ₂	1.18	0.5	10.39	5.12	27,600	2/3 y _B	97
10	SF ₆ /N ₂	1.18	0.5	10.39	5.12	27,600	0.3 D Wake	98
10	SF ₆ /N ₂	1.18	0.5	10.39	5.12	27,600	1/2 D Wake	99
10	SF ₆ /N ₂	1.18	0.5	10.39	5.12	27,600	3/4 D Wake	100
10	SF ₆ /N ₂	2.50	0.5	16.9	7.26	27,600	Central	101

$P = 1/2 \text{ Atm}$

$t = 0.48 \text{ Sec}$

$z/D_0 = 5.01$

$Re \sim 650$

Air/He

$D_0 = 1.0 \text{ In.}$

$D/D_0 = 2.88$

Central Cut

$r \text{ (in.)}$	r/r_{edge}	C_M	ρ/ρ_∞	$r \text{ (in.)}$	r/r_{edge}	C_M	ρ/ρ_∞
2.88E-2	.02	-1.87E-3	1.012E+0	7.50E-1	.52	6.82E-3	9.591E-1
5.77	.04	-1.54	1.010	7.79	.54	6.96	9.583
8.65	.06	-1.43	1.009	8.08	.56	7.08	9.576
1.15E-1	.08	-1.20	1.008	8.36	.58	7.12	9.574
1.44	.1	-9.60E-4	1.005	8.65	.6	7.10	9.575
1.73	.12	-7.42	1.005	8.94	.62	7.07	9.577
2.02	.14	-6.22	1.004	9.23	.64	7.00	9.581
2.31	.16	-3.81	1.002	9.52	.66	6.89	9.587
2.6	.18	-1.02	1.001	9.81	.68	6.77	9.594
2.88	.2	2.57	9.984E-1	1.010E+0	.7	6.63	9.602
3.17	.22	6.25	9.961	1.038	.72	6.47	9.612
3.46	.24	1.09E-3	9.932	1.067	.74	6.29	9.622
3.75	.26	1.59	9.902	1.096	.76	6.24	9.625
4.04	.28	2.16	9.867	1.125	.78	5.60	9.662
4.33	.3	2.69	9.835	1.154	.8	5.36	9.676
4.61	.32	3.15	9.807	1.183	.82	5.04	9.694
4.90	.34	3.61	9.780	1.211	.84	4.71	9.714
5.19	.36	4.10	9.750	1.240	.86	4.32	9.737
5.48	.38	4.56	9.723	1.269	.88	3.93	9.760
5.77	.4	5.18	9.687	1.298	.9	3.53	9.784
6.06	.42	5.91	9.644	1.327	.92	3.10	9.810
6.35	.44	6.16	9.630	1.356	.94	2.64	9.837
6.63	.46	6.31	9.621	1.384	.96	2.13	9.868
6.92	.48	6.51	9.609	1.413	.98	1.49	9.908
7.21	.5	6.68	9.599	1.442	1.00	0.	1.0E+0

$P = 1 \text{ Atm}$ $t = 0.19 \text{ Sec}$ $z/D_0 = 3.16$ $Re \sim 1100$
 Air/He $D_0 = 0.9 \text{ In.}$ $D/D_0 = 2.22$ Central Cut

$r \text{ (in.)}$	r/r_{edge}	C_M	ρ/ρ_∞	$r \text{ (in.)}$	r/r_{edge}	C_M	ρ/ρ_∞
0.	0.	4.79E-3	9.709E-1	.5	.5	4.007E-2	7.997E-1
.02	.02	5.69	9.656	.52	.52	3.960	8.016
.04	.04	6.86	9.589	.54	.54	3.884	8.046
.06	.06	6.44	9.613	.56	.56	3.844	8.063
.08	.08	6.37	9.617	.58	.58	3.827	8.070
.10	.1	7.11	9.574	.6	.6	3.798	8.082
.12	.12	7.87	9.531	.62	.62	3.682	8.129
.14	.14	8.49	9.496	.64	.64	3.674	8.144
.16	.16	9.94	9.415	.66	.66	3.565	8.178
.18	.18	1.075E-2	9.370	.68	.68	3.456	8.224
.20	.2	1.248	9.276	.7	.7	3.335	8.275
.22	.22	1.368	9.212	.72	.72	3.191	8.337
.24	.24	1.558	9.113	.74	.74	3.061	8.394
.26	.26	1.730	9.204	.76	.76	2.913	8.460
.28	.28	1.916	8.331	.78	.78	2.727	8.544
.30	.3	2.143	8.819	.8	.8	2.620	8.593
.32	.32	2.345	8.722	.82	.82	2.485	8.655
.34	.34	2.561	8.620	.84	.84	2.264	8.760
.36	.36	3.036	8.405	.86	.86	2.085	8.847
.38	.38	3.383	8.254	.88	.88	1.829	8.974
.40	.4	3.778	8.090	.9	.9	1.619	9.081
.42	.42	4.087	7.965	.92	.92	1.414	9.188
.44	.44	4.033	7.987	.94	.94	1.220	9.292
.46	.46	4.087	7.965	.96	.96	9.73E-3	9.427
.48	.48	4.078	7.969	.98	.98	6.69	9.599

P = 1 Atm

t = 0.19 Sec

$z/D_0 = 3.16$

Re ~ 1100

Air/He

$D_0 = 0.9$ In.

$D/D_0 = 2.22$

1/2 D Wake Cut

r (in.)	r/r _{edge}	C _M	ρ/ρ_∞	r (in.)	r/r _{edge}	C _M	ρ/ρ_∞
0.	0.	2.75E-2	8.53E-1	3.33E-1	5.09E-1	1.54E-2	9.12E-1
1.19E-2	1.82E-2	2.62	8.59	3.45	5.27	1.53	9.13
2.38	3.64	2.58	8.61	3.57	5.45	1.52	9.13
3.57	5.45	2.63	8.59	3.68	5.64	1.54	9.12
4.75	7.27	2.50	8.65	3.80	5.82	1.48	9.15
5.94	9.09	2.47	8.66	3.92	6.0	1.50	9.14
7.13	1.09E-1	2.51	8.64	4.04	6.18	1.48	9.15
8.32	1.27	2.38	8.70	4.16	6.36	1.49	9.15
9.51	1.45	2.31	8.74	4.28	6.55	1.48	9.15
1.07E-1	1.64	2.25	8.77	4.40	6.73	1.46	9.16
1.19	1.82	2.25	8.77	4.52	6.91	1.47	9.16
1.31	2.0	2.04	8.87	4.63	7.09	1.46	9.16
1.43	2.18	2.11	8.83	4.75	7.27	1.41	9.19
1.55	2.36	2.03	8.87	4.87	7.45	1.43	9.18
1.66	2.55	1.98	8.90	4.99	7.64	1.39	9.20
1.78	2.73	1.93	8.92	5.11	7.82	1.33	9.23
1.90	2.91	1.93	8.92	5.23	8.0	1.28	9.26
2.02	3.09	1.86	8.96	5.35	8.18	1.24	9.28
2.14	3.27	1.86	8.96	5.47	8.36	1.20	9.30
2.26	3.45	1.77	9.00	5.59	8.55	1.14	9.33
2.38	3.64	1.80	8.99	5.70	8.73	1.04	9.39
2.50	3.82	1.72	9.03	5.82	8.91	9.28E-3	9.45
2.61	4.0	1.73	9.03	5.94	9.09	8.24	9.51
2.73	4.18	1.68	9.05	6.06	9.27	7.27	9.57
2.85	4.36	1.69	9.04	6.18	9.45	6.12	9.63
2.97	4.55	1.63	9.08	6.30	9.64	4.37	9.73
3.09	4.73	1.61	9.09	6.42	9.82	2.86	9.82
3.21	4.91	1.64	9.07				

P = 1 Atm

t = 0.19 Sec

z/D₀ = 3.16

Re ~ 1100

Air/He

D₀ = 0.9 In.

D/D₀ = 2.22

3/4 D Wake Cut

r (in.)	r/r _{edge}	C _M	ρ/ρ _∞	r (in.)	r/r _{edge}	C _M	ρ/ρ _∞
0.	0.	2.85E-2	8.49E-1				
9.74E-3	1.75E-2	2.47	8.66	2.82E-1	5.09E-1	1.86E-2	8.96E-1
1.95E-2	3.51	2.46	8.67	2.92	5.26	1.84	8.98
2.92	5.26	2.56	8.62	3.02	5.44	1.80	8.99
3.90	7.02	2.51	8.64	3.12	5.61	1.79	8.99
4.87	8.77	2.53	8.64	3.21	5.79	1.77	9.00
5.84	1.05E-1	2.46	8.67	3.31	5.96	1.73	9.03
6.82	1.23	2.51	8.64	3.41	6.14	1.73	9.02
7.79	1.40	2.44	8.68	3.50	6.32	1.69	9.04
8.77	1.58	2.48	8.66	3.60	6.49	1.67	9.06
9.74	1.75	2.43	8.68	3.70	6.67	1.65	9.07
1.07E-1	1.93	2.44	8.68	3.80	6.84	1.59	9.10
1.17	2.11	2.35	8.72	3.90	7.02	1.63	9.08
1.27	2.28	2.28	8.75	3.99	7.19	1.52	9.13
1.36	2.46	2.29	8.75	4.09	7.37	1.44	9.17
1.46	2.63	2.23	8.78	4.19	7.54	1.41	9.19
1.56	2.81	2.17	8.80	4.29	7.72	1.36	9.22
1.66	2.98	2.12	8.83	4.38	7.89	1.29	9.36
1.75	3.16	2.06	8.86	4.48	8.07	1.19	9.31
1.85	3.33	2.05	8.87	4.58	8.25	1.08	9.37
1.95	3.51	1.97	8.90	4.68	8.42	1.01	9.41
2.05	3.68	1.95	8.91	4.77	8.60	9.08E-3	9.46
2.14	3.86	1.89	8.94	4.87	8.77	8.97	9.47
2.24	4.04	1.89	8.95	4.97	8.95	7.44	9.56
2.34	4.21	1.91	8.93	5.06	9.12	6.72	9.60
2.44	4.39	1.88	8.95	5.16	9.30	5.82	9.65
2.53	4.56	1.88	8.95	5.26	9.47	4.74	9.71
2.63	4.74	1.86	8.96	5.36	9.65	3.30	9.80
2.73	4.91	1.84	8.97	5.45	9.82	2.30	9.86

$P = 1 \text{ Atm}$ $t = 0.19 \text{ Sec}$ $z/D_0 = 3.16$ $Re \sim 1100$
 Air/He $D_0 = 0.9 \text{ In.}$ $D/D_0 = 2.22$ $D \text{ Wake Cut}$

$r \text{ (in.)}$	r/r_{edge}	C_M	ρ/ρ_∞	$r \text{ (in.)}$	r/r_{edge}	C_M	ρ/ρ_∞
0.	0.	2.13E-2	8.83E-1	2.36E-1	4.92E-1	1.84E-2	8.97E-1
8.14E-3	1.69E-2	2.18	8.80	2.44	5.08	1.80	8.99
1.63E-2	3.39	2.18	8.80	2.52	5.25	1.80	8.99
2.44	5.08	2.12	8.83	2.61	5.42	1.75	9.02
3.26	6.78	2.04	8.87	2.69	5.59	1.79	9.00
4.07	8.47	2.17	8.81	2.77	5.76	1.72	9.03
4.88	1.02E-1	2.15	8.82	2.85	5.93	1.68	9.05
5.70	1.19	2.16	8.81	2.93	6.10	1.69	9.04
6.51	1.36	2.12	8.83	3.01	6.27	1.62	9.08
7.33	1.53	2.15	8.81	3.09	6.44	1.57	9.11
8.14	1.69	2.22	8.78	3.18	6.61	1.55	9.12
8.96	1.86	2.16	8.81	3.26	6.78	1.51	9.14
9.77	2.03	2.19	8.80	3.34	6.95	1.47	9.16
1.06E-1	2.20	2.14	8.82	3.42	7.12	1.40	9.19
1.14	2.37	2.18	8.80	3.50	7.29	1.35	9.22
1.22	2.54	2.13	8.82	3.58	7.46	1.26	9.27
1.30	2.71	2.08	8.85	3.66	7.63	1.23	9.28
1.38	2.88	2.03	8.88	3.75	7.80	1.15	9.33
1.47	3.05	2.01	8.89	3.83	7.97	1.08	9.37
1.55	3.22	2.00	8.89	3.91	8.14	1.03	9.40
1.63	3.39	1.97	8.90	3.99	8.31	9.84E-3	9.42
1.71	3.56	1.99	8.89	4.07	8.47	9.03	9.47
1.79	3.73	1.98	8.90	4.15	8.64	8.32	9.51
1.87	3.90	1.96	8.91	4.23	8.81	7.46	9.55
1.95	4.07	1.95	8.91	4.32	8.98	6.97	9.58
2.04	4.24	1.94	8.92	4.40	9.15	6.02	9.64
2.12	4.41	1.90	8.94	4.48	9.32	5.22	9.68
2.20	4.58	1.87	8.95	4.56	9.49	4.60	9.72
2.28	4.75	1.86	8.96	4.64	9.66	3.40	9.79
				4.72	9.83	2.37	9.85

P = 1 Atm

t = 0.55 Sec

 $z/D_0 = 5.92$

Re ~ 1300

Air/He

 $D_0 = 1.0$ In. $D/D_0 = 2.85$

Central Cut

r (in.)	r/r _{edge}	C _M	ρ/ρ_∞	r (in.)	r/r _{edge}	C _M	ρ/ρ_∞
2.85E-2	.02	1.12E-3	9.931E-1	7.40E-1	.52	9.54E-3	9.437E-1
5.70	.04	1.65	9.898	7.69	.54	9.42	9.444
8.54	.06	1.82	9.887	7.97	.56	9.26	9.453
1.14E-1	.08	2.01	9.876	8.26	.58	9.10	9.462
1.42	.1	2.24	9.862	8.54	.6	8.97	9.469
1.71	.12	2.57	9.842	8.83	.62	8.62	9.489
1.99	.14	2.98	9.817	9.11	.64	8.35	9.504
2.28	.16	3.54	9.783	9.40	.66	8.05	9.521
2.56	.18	4.15	9.747	9.68	.68	7.73	9.539
2.85	.2	4.58	9.722	9.97	.7	7.45	9.555
3.13	.22	5.26	9.682	1.025E+0	.72	7.13	9.573
3.42	.24	6.04	9.636	1.054	.74	6.76	9.595
3.70	.26	6.72	9.597	1.082	.76	6.35	9.618
3.99	.28	7.52	9.551	1.111	.78	5.91	9.644
4.27	.3	8.25	9.509	1.139	.8	5.42	9.673
4.56	.32	8.40	9.501	1.168	.82	4.98	9.698
4.84	.34	8.58	9.491	1.196	.84	4.63	9.719
5.13	.36	8.85	9.476	1.225	.86	4.19	9.745
5.41	.38	9.19	9.457	1.253	.88	3.65	9.777
5.70	.4	9.35	9.448	1.281	.9	3.19	9.804
5.98	.42	9.39	9.445	1.310	.92	2.81	9.828
6.27	.44	9.49	9.440	1.339	.94	2.55	9.843
6.55	.46	9.57	9.436	1.367	.96	2.25	9.861
6.83	.48	9.55	9.437	1.395	.98	1.87	9.884
7.12	.5	9.59	9.435	1.424	1.00	0.	1.0E+0

P = 4 Atm

t = 0.80 Sec

 $z/D_0 = 5.65$

Re ~ 5200

Air/He

 $D_0 = 1.0$ In. $D/D_0 = 3.12$

Central Cut

r (in.)	r/r _{edge}	C _M	ρ/ρ_∞	r (in.)	r/r _{edge}	C _M	ρ/ρ_∞
3.12E-2	.02	-1.18E-2	1.080E+0	8.11E-1	.52	1.880E-2	8.949E-1
6.24	.04	-8.34E-3	1.055	8.43	.54	2.060	8.859
9.36	.06	-6.16	1.040	8.74	.56	2.052	8.863
1.25E-1	.08	-4.57	1.029	9.05	.58	2.025	8.876
1.56	.1	-3.48	1.022	9.36	.6	1.962	8.908
1.87	.12	-2.47	1.016	9.67	.62	1.898	8.940
2.18	.14	-1.47	1.009	9.99	.64	1.834	8.971
2.50	.16	-4.40E-4	1.003	1.030	.66	1.733	9.023
2.81	.18	2.09	9.987E-1	1.061	.68	1.630	9.075
3.12	.2	8.76	9.946	1.092	.7	1.541	9.121
3.43	.22	1.58E-3	9.902	1.123	.72	1.370	9.211
3.74	.24	2.08	9.872	1.155	.74	1.199	9.303
4.06	.26	2.51	9.846	1.186	.76	1.079	9.369
4.37	.28	3.08	9.811	1.217	.78	9.73E-3	9.427
4.68	.3	3.55	9.783	1.248	.8	8.92	9.472
4.99	.32	4.02	9.755	1.279	.82	8.23	9.511
5.30	.34	4.36	9.735	1.311	.84	6.96	9.583
5.62	.36	4.63	9.719	1.342	.86	5.59	9.662
5.93	.38	5.04	9.695	1.373	.88	4.66	9.717
6.24	.4	5.60	9.662	1.404	.9	4.15	9.747
6.55	.42	6.48	9.61	1.435	.92	3.56	9.782
6.87	.44	7.72	9.539	1.467	.94	2.90	9.822
7.18	.46	9.32	9.450	1.498	.96	2.24	9.862
7.49	.48	1.131E-2	9.340	1.529	.98	1.54	9.905
7.80	.5	1.442	9.173	1.560	1.0	0.	1.0E+0

P = 8 Atm

t = 1.44 Sec

$z/D_0 = 9.44$

Re ~ 10,400

Air/He

$D_0 = 1.0$ In.

$D/D_0 = 4.84$

Central Cut

r (in.)	r/r _{edge}	C _M	ρ/ρ_∞	r (in.)	r/r _{edge}	C _M	ρ/ρ_∞
0.	0.	3.71E-4	9.977E-1	1.209E+0	.5	2.18E-3	9.865E-1
4.84E-2	.02	4.61	9.971	1.258	.52	2.86	9.825
9.68	.04	2.21	9.986	1.307	.54	3.41	9.791
1.45E-1	.06	-1.83E-5	1.000E+0	1.356	.56	3.59	9.780
1.94	.08	6.26	9.996E-1	1.405	.58	3.61	9.779
2.42	.1	1.01E-4	9.994	1.454	.6	3.57	9.782
2.90	.12	1.83	9.989	1.503	.62	3.55	9.783
3.39	.14	1.61	9.990	1.552	.64	3.47	9.788
3.88	.16	2.75	9.983	1.600	.66	3.42	9.791
4.36	.18	3.38	9.979	1.648	.68	3.26	9.800
4.84	.2	2.88	9.982	1.696	.7	3.13	9.808
5.32	.22	2.40	9.985	1.744	.72	3.01	9.816
5.80	.24	2.28	9.986	1.792	.74	2.82	9.827
6.29	.26	3.12	9.981	1.840	.76	2.76	9.830
6.78	.28	2.76	9.983	1.888	.78	2.55	9.843
7.27	.3	3.07	9.981	1.936	.8	2.45	9.849
7.76	.32	3.72	9.977	1.984	.82	2.25	9.861
8.24	.34	3.61	9.977	2.032	.84	2.21	9.864
8.72	.36	4.03	9.975	2.080	.86	1.62	9.900
9.20	.38	5.53	9.966	2.128	.88	1.71	9.894
9.68	.4	6.47	9.960	2.176	.9	1.56	9.904
1.016E+0	.42	8.45	9.947	2.224	.92	1.36	9.915
1.064	.44	1.05E-3	9.935	2.272	.94	1.17	9.927
1.112	.46	1.35	9.916	2.320	.96	9.53E-4	9.941
1.160	.48	1.64	9.898	2.369	.98	6.47E-4	9.960

P = 10 Atm

t = 0.90 Sec

 $z/D_0 = 5.76$

Re ~ 13,000

Air/He

 $D_0 = 1.0$ In. $D/D_0 = 4.04$

Central Cut

r (in.)	r/r _{edge}	C _M	ρ/ρ_∞	r (in.)	r/r _{edge}	C _M	ρ/ρ_∞
4.04E-2	.02	-1.05E-2	1.071E+0	1.051E+0	.52	5.55E-3	9.665E-1
8.08	.04	-6.96E-3	1.046	1.091	.54	5.27	9.681
1.21E-1	.06	-4.83	1.031	1.131	.56	4.99	9.698
1.62	.08	-3.25	1.021	1.172	.58	4.75	9.711
2.02	.1	-2.12	1.013	1.212	.6	4.49	9.727
2.42	.12	-1.42	1.009	1.253	.62	4.31	9.737
2.83	.14	-1.25	1.008	1.293	.64	4.09	9.751
3.23	.16	-1.02	1.007	1.333	.66	3.95	9.759
3.64	.18	-7.62E-4	1.005	1.374	.68	3.96	9.759
4.04	.2	-5.06	1.003	1.414	.7	3.84	9.766
4.44	.22	-3.39	1.002	1.455	.72	3.74	9.771
4.85	.24	8.86E-6	9.999E-1	1.495	.74	3.80	9.768
5.25	.26	2.70E-4	9.983	1.535	.76	3.69	9.775
5.66	.28	4.52	9.972	1.576	.78	3.27	9.800
6.06	.3	6.27	9.961	1.616	.8	2.91	9.822
6.46	.32	8.20	9.949	1.657	.82	2.84	9.826
6.87	.34	1.25E-3	9.922	1.697	.84	2.79	9.829
7.27	.36	1.69	9.896	1.737	.86	2.60	9.840
7.68	.38	2.00	9.876	1.778	.88	2.36	9.855
8.08	.4	2.44	9.850	1.818	.9	2.01	9.876
8.48	.42	2.93	9.820	1.859	.92	1.67	9.897
8.89	.44	3.80	9.768	1.899	.94	1.37	9.915
9.29	.46	5.39	9.674	1.939	.96	1.15	9.929
9.70	.48	6.28	9.622	1.980	.98	8.66E-4	9.946
1.010E+0	.5	5.98	9.640	2.020	1.0	0.	1.0E+0

P = 10 Atm

t = 0.68 Sec

$z/D_0 = 5.99$

Re ~ 27,600

SF₆/N₂

D₀ = 0.5 In.

D/D₀ = 3.80

Central Cut

r (in.)	r/r _{edge}	C _M	ρ/ρ _∞	r (in.)	r/r _{edge}	C _M	ρ/ρ _∞
1.81E-2	.02	-5.17E-3	1.022E+0	4.71E-1	.52	6.71E-3	9.725E-1
3.62	.04	-4.03	1.017	4.89	.54	5.75	9.763
5.43	.06	-3.51	1.015	5.07	.56	5.44	9.776
7.24	.08	-3.13	1.013	5.25	.58	5.23	9.784
9.05	.1	-2.99	1.013	5.43	.6	4.99	9.794
1.09E-1	.12	-4.11	1.018	5.61	.62	4.79	9.802
1.27	.14	-1.65	1.007	5.79	.64	4.59	9.810
1.45	.16	-1.06	1.005	5.97	.66	4.44	9.816
1.63	.18	-6.22E-4	1.003	6.15	.68	4.28	9.823
1.81	.2	-2.60	1.001	6.34	.7	4.13	9.829
1.99	.22	2.35	9.990E-1	6.52	.72	3.94	9.837
2.17	.24	8.22	9.966	6.70	.74	3.77	9.843
2.35	.26	1.35E-3	9.944	6.88	.76	3.58	9.851
2.53	.28	1.88	9.921	7.06	.78	3.37	9.860
2.72	.3	2.42	9.899	7.24	.8	3.16	9.868
2.90	.32	2.94	9.878	7.42	.82	2.96	9.877
3.08	.34	3.45	9.856	7.60	.84	2.70	9.888
3.26	.36	4.08	9.831	7.78	.86	2.46	9.897
3.44	.38	5.07	9.791	7.96	.88	2.24	9.906
3.62	.4	6.27	9.742	8.15	.9	1.98	9.917
3.80	.42	6.25	9.743	8.33	.92	1.74	9.927
3.98	.44	6.17	9.747	8.51	.94	1.48	9.938
4.16	.46	6.13	9.748	8.69	.96	1.19	9.950
4.34	.48	6.10	9.749	8.87	.98	8.34E-4	9.965
4.53	.5	6.21	9.745	9.05	1.0	0.	1.0E+1

P = 10 Atm

t = 1.18 Sec

 $z/D_0 = 10.39$

Re ~ 27,600

SF₆/N₂D₀ = 0.5 In.D/D₀ = 5.12

Central Cut

r (in.)	r/r _{edge}	C _M	ρ/ρ_∞	r (in.)	r/r _{edge}	C _M	ρ/ρ_∞
2.56E-2	.02	-2.69E-3	1.012E+0	6.66E-1	.52	3.65E-3	9.848E-1
5.12	.04	-2.06	1.009	6.92	.54	3.70	9.846
7.68	.06	-1.68	1.007	7.17	.56	3.70	9.846
1.02E-1	.08	-1.29	1.005	7.43	.58	3.63	9.849
1.28	.1	-9.57E-4	1.004	7.68	.6	3.55	9.853
1.54	.12	-7.18	1.003	7.94	.62	3.46	9.856
1.79	.14	-4.22	1.002	8.20	.64	3.33	9.861
2.05	.16	-2.26	1.001	8.45	.66	3.22	9.866
2.31	.18	-6.38E-5	1.000	8.71	.68	3.11	9.871
2.56	.2	1.20E-4	9.995E-1	8.97	.7	3.01	9.875
2.82	.22	2.63	9.989	9.22	.72	2.88	9.880
3.07	.24	3.61	9.985	9.48	.74	2.70	9.887
3.33	.26	4.96	9.974	9.73	.76	2.54	9.894
3.59	.28	6.00	9.975	9.99	.78	2.39	9.900
3.84	.3	6.68	9.972	1.025E+0	.8	2.21	9.908
4.10	.32	7.77	9.967	1.050	.82	2.08	9.913
4.35	.34	8.99	9.962	1.076	.84	1.94	9.919
4.61	.36	9.83	9.959	1.101	.86	1.79	9.925
4.87	.38	1.14E-3	9.952	1.127	.88	1.64	9.932
5.12	.4	1.37	9.943	1.153	.9	1.49	9.938
5.38	.42	1.75	9.927	1.178	.92	1.30	9.945
5.64	.44	2.17	9.909	1.204	.94	1.13	9.953
5.89	.46	2.79	9.884	1.230	.96	9.26E-4	9.961
6.15	.48	3.51	9.854	1.255	.98	6.71	9.972
6.40	.5	3.63	9.849	1.281	1.0	0.	1.0E+0

P = 10 Atm

t = 1.18 Sec

z/D₀ = 10.39

Re ~ 27,600

SF₆/N₂

D₀ = 0.5 In.

D/D₀ = 5.12

2/3 y_T Cut

r (in.)	r/r _{edge}	C _M	ρ/ρ _∞	r (in.)	r/r _{edge}	C _M	ρ/ρ _∞
2.16E-2	.02	-1.63E-3	1.007E+0	5.62E-1	.52	1.55E-3	9.935E-1
4.32	.04	-1.01	1.004	5.83	.54	1.59	9.933
6.48	.06	-6.13E-4	1.003	6.04	.56	1.62	9.932
8.64	.08	-2.48	1.001	6.27	.58	1.65	9.931
1.08E-1	.1	-2.80E-5	1.000	6.48	.6	1.65	9.931
1.30	.12	2.09E-4	9.991E-1	6.70	.62	1.63	9.932
1.51	.14	3.36	9.986	6.91	.64	1.60	9.933
1.73	.16	5.07	9.979	7.13	.66	1.60	9.933
1.94	.18	6.02	9.975	7.35	.68	1.59	9.933
2.16	.2	6.79	9.971	7.56	.7	1.58	9.934
2.38	.22	7.42	9.969	7.78	.72	1.56	9.935
2.59	.24	8.17	9.966	7.99	.74	1.54	9.936
2.81	.26	9.37	9.961	8.20	.76	1.52	9.936
3.02	.28	1.06E-3	9.956	8.43	.78	1.47	9.938
3.24	.3	1.15	9.952	8.64	.8	1.41	9.941
3.46	.32	1.20	9.950	8.86	.82	1.30	9.946
3.67	.34	1.26	9.947	9.07	.84	1.22	9.949
3.89	.36	1.32	9.945	9.29	.86	1.11	9.953
4.10	.38	1.38	9.942	9.51	.88	1.02	9.957
4.32	.4	1.41	9.941	9.72	.9	9.12E-4	9.962
4.54	.42	1.44	9.940	9.94	.92	7.75	9.967
4.75	.44	1.48	9.938	1.015E+0	.94	7.00	9.971
4.96	.46	1.52	9.936	1.037	.96	5.63	9.976
5.19	.48	1.53	9.936	1.059	.98	3.43	9.986
5.40	.5	1.54	9.936	1.080	1.0	0.	1.0E+0

P = 10 Atm

t = 1.18 Sec

 $z/D_0 = 10.39$

Re ~ 27,600

SF₆/N₂D₀ = 0.5 In.D/D₀ = 5.121/3 y_T Cut

r (in.)	r/r _{edge}	C _M	ρ/ρ _∞	r (in.)	r/r _{edge}	C _M	ρ/ρ _∞
2.47E-2	.02	-2.05E-3	1.009E+0	6.42E-1	.52	2.72E-3	9.887E-1
4.94	.04	-1.53	1.007	6.67	.54	2.66	9.889
7.41	.06	-1.19	1.005	6.92	.56	2.58	9.892
9.88	.08	-9.24E-4	1.004	7.16	.58	2.47	9.897
1.24E-1	.1	-6.45	1.003	7.41	.6	2.35	9.902
1.48	.12	-4.26	1.002	7.66	.62	2.26	9.906
1.73	.14	-2.76	1.001	7.90	.64	2.20	9.908
1.98	.16	-1.49	1.001	8.15	.66	2.12	9.912
2.22	.18	-7.26E-5	1.000	8.40	.68	2.06	9.914
2.47	.2	1.88	9.999E-1	8.64	.7	2.03	9.915
2.72	.22	1.30E-4	9.995	8.89	.72	1.97	9.918
2.96	.24	2.30	9.990	9.14	.74	1.92	9.920
3.21	.26	3.20	9.987	9.39	.76	1.88	9.921
3.46	.28	4.65	9.980	9.63	.78	1.83	9.924
3.70	.3	6.37	9.973	9.88	.8	1.77	9.926
3.95	.32	8.08	9.966	1.013E+0	.82	1.72	9.928
4.20	.34	1.02E-3	9.957	1.037	.84	1.67	9.930
4.45	.36	1.28	9.946	1.062	.86	1.55	9.935
4.69	.38	1.56	9.935	1.087	.88	1.41	9.941
4.94	.4	1.92	9.920	1.112	.9	1.27	9.947
5.19	.42	2.57	9.893	1.136	.92	1.15	9.952
5.43	.44	2.95	9.877	1.161	.94	1.02	9.957
5.68	.46	2.88	9.880	1.186	.96	9.35E-4	9.961
5.93	.48	2.82	9.882	1.210	.98	7.32	9.969
6.17	.5	2.77	9.885	1.235	1.0	0.	1.0E+1

P = 10 Atm

t = 1.18 Sec

z/D₀ = 10.39

Re ~ 27,600

SF₆/N₂

D₀ = 0.5 In.

D/D₀ = 5.12

1/3 y_B Cut

r (in.)	r/r _{edge}	C _M	ρ/ρ _∞	r (in.)	r/r _{edge}	C _M	ρ/ρ _∞
2.55E-2	.02	-2.87E-3	1.012E+0	6.63E-1	.52	3.25E-3	9.865E-1
5.10	.04	-2.05	1.009	6.89	.54	3.29	9.863
7.65	.06	-1.48	1.006	7.14	.56	3.47	9.858
1.02E-1	.08	-1.18	1.005	7.40	.58	2.96	9.877
1.28	.1	-1.05	1.004	7.65	.6	2.78	9.884
1.53	.12	-6.14E-4	1.003	7.91	.62	2.77	9.885
1.79	.14	-3.13	1.001	8.16	.64	2.75	9.885
2.04	.16	-4.04	1.002	8.42	.66	2.75	9.885
2.30	.18	2.63E-5	9.999E-1	8.67	.68	2.61	9.891
2.55	.2	5.87E-4	9.975	8.93	.7	2.43	9.899
2.81	.22	6.81	9.971	9.18	.72	2.32	9.903
3.06	.24	6.64	9.972	9.44	.74	2.21	9.908
3.32	.26	7.46	9.969	9.69	.76	2.09	9.913
3.57	.28	8.43	9.965	9.95	.78	1.96	9.918
3.83	.3	8.96	9.962	1.020E+0	.8	1.82	9.924
4.08	.32	9.36	9.961	1.046	.82	1.68	9.930
4.34	.34	9.89	9.959	1.071	.84	1.57	9.934
4.59	.36	1.17E-3	9.951	1.097	.86	1.46	9.939
4.85	.38	1.43	9.940	1.122	.88	1.34	9.944
5.10	.4	1.73	9.928	1.148	.9	1.22	9.949
5.36	.42	2.08	9.913	1.173	.92	1.08	9.955
5.61	.44	2.62	9.891	1.199	.94	9.20E-4	9.961
5.87	.46	3.17	9.868	1.224	.96	7.63	9.968
6.12	.48	3.27	9.864	1.250	.98	6.38	9.973
6.38	.5	3.26	9.864	1.275	1.0	0.	1.0E+0

P = 10 Atm

t = 1.18 Sec

z/D₀ = 10.39

Re ~ 27,600

SF₆/N₂

D₀ = 0.5 In.

D/D₀ = 5.12

2/3 y_B Cut

r (in.)	r/r _{edge}	C _M	ρ/ρ _∞	r (in.)	r/r _{edge}	C _M	ρ/ρ _∞
2.61E-2	.02	-1.99E-3	1.008E+1	6.78E-1	.52	1.57E-3	9.934E-1
5.22	.04	-1.15	1.005	7.04	.54	1.63	9.932
7.83	.06	-6.81E-4	1.001	7.30	.56	1.63	9.932
1.04E-1	.08	-2.11	1.000	7.56	.58	1.65	9.931
1.30	.1	1.11	9.995E-1	7.83	.6	1.69	9.929
1.57	.12	2.32	9.990	8.09	.62	1.75	9.927
1.83	.14	3.54	9.985	8.35	.64	1.81	9.924
2.09	.16	4.84	9.980	8.61	.66	1.84	9.923
2.35	.18	6.78	9.972	8.87	.68	1.82	9.924
2.61	.2	8.11	9.966	9.13	.7	1.74	9.927
2.87	.22	8.62	9.964	9.39	.72	1.65	9.931
3.13	.24	9.25	9.961	9.65	.74	1.56	9.935
3.39	.26	1.03E-3	9.957	9.91	.76	1.42	9.941
3.65	.28	1.10	9.954	1.017E+0	.78	1.31	9.945
3.91	.3	1.18	9.951	1.043	.8	1.25	9.948
4.17	.32	1.19	9.950	1.070	.82	1.16	9.951
4.43	.34	1.20	9.950	1.096	.84	1.09	9.954
4.70	.36	1.20	9.950	1.122	.86	1.04	9.956
4.96	.38	1.24	9.948	1.148	.88	9.80E-4	9.959
5.22	.4	1.29	9.946	1.174	.9	8.83	9.963
5.48	.42	1.37	9.943	1.200	.92	7.81	9.967
5.74	.44	1.46	9.939	1.226	.94	6.96	9.971
6.00	.46	1.50	9.937	1.252	.96	5.50	9.977
6.26	.48	1.50	9.937	1.278	.98	2.45	9.985
6.52	.5	1.52	9.936	1.304	1.00	0.	1.0E+0

P = 10 Atm

t = 1.18 Sec

 $z/D_0 = 10.39$

Re ~ 27,600

SF₆/N₂D₀ = 0.5 In.D/D₀ = 5.12

0.3 D Wake Cut

r (in.)	r/r _{edge}	C _M	ρ/ρ_∞	r (in.)	r/r _{edge}	C _M	ρ/ρ_∞
2.21E-2	.02	1.11E-4	9.995E-1	5.76E-1	.52	9.87E-4	9.957E-1
4.43	.04	3.56	9.985	5.98	.54	1.023E-3	9.957
6.64	.06	4.55	9.981	6.20	.56	1.022	9.956
8.86	.08	5.12	9.979	6.42	.58	1.033	9.957
1.11E-1	.1	5.77	9.976	6.65	.6	1.039	9.956
1.33	.12	5.18	9.978	6.87	.62	1.031	9.957
1.55	.14	5.70	9.976	7.09	.64	9.80E-4	9.959
1.77	.16	6.16	9.974	7.31	.66	9.44	9.960
1.99	.18	5.80	9.975	7.53	.68	9.38	9.961
2.21	.2	5.94	9.975	7.75	.7	9.21	9.961
2.44	.22	6.35	9.973	7.97	.72	9.12	9.962
2.66	.24	7.08	9.970	8.19	.74	8.97	9.962
2.88	.26	7.59	9.968	8.42	.76	8.74	9.963
3.1	.28	7.99	9.966	8.64	.78	8.53	9.964
3.32	.3	8.29	9.965	8.86	.8	8.33	9.965
3.54	.32	8.31	9.964	9.08	.82	8.19	9.966
3.76	.34	8.48	9.963	9.30	.84	7.87	9.967
3.99	.36	8.88	9.961	9.52	.86	7.32	9.969
4.21	.38	9.18	9.961	9.74	.88	6.79	9.971
4.43	.4	9.34	9.960	9.97	.9	6.11	9.974
4.65	.42	9.63	9.959	1.019E+0	.92	5.30	9.978
4.87	.44	9.81	9.960	1.041	.94	4.49	9.981
5.09	.46	9.56	9.960	1.063	.96	3.63	9.985
5.32	.48	9.44	9.959	1.085	.98	2.55	9.989
5.54	.5	9.66	9.957	1.107	1.0	0.	1.0E+1

P = 10 Atm

t = 1.18 Sec

z/D₀ = 10.39

Re ~ 27,600

SF₆/N₂

D₀ = 0.5 In.

D/D₀ = 5.12

1/2 D Wake Cut

r (in.)	r/r _{edge}	C _M	ρ/ρ _∞	r (in.)	r/r _{edge}	C _M	ρ/ρ _∞
1.81E-2	.02	2.13E-4	9.991E-1	4.71E-1	.52	7.11E-4	9.970E-1
3.63	.04	4.17	9.983	4.89	.54	7.07	9.970
5.44	.06	4.91	9.979	5.08	.56	7.07	9.970
7.25	.08	5.87	9.975	5.26	.58	7.17	9.970
9.06	.1	6.32	9.973	5.44	.6	7.35	9.969
1.09E-1	.12	6.25	9.974	5.62	.62	7.22	9.970
1.27	.14	6.29	9.974	5.80	.64	7.12	9.970
1.45	.16	5.62	9.976	5.98	.66	6.86	9.971
1.63	.18	5.38	9.977	6.16	.68	6.70	9.972
1.81	.2	5.32	9.978	6.34	.7	6.64	9.972
1.99	.22	4.66	9.980	6.53	.72	6.44	9.973
2.18	.24	4.53	9.981	6.71	.74	6.16	9.974
2.36	.26	4.70	9.980	6.89	.76	5.78	9.976
2.54	.28	4.96	9.979	7.07	.78	5.42	9.977
2.72	.3	5.28	9.978	7.25	.8	5.45	9.977
2.90	.32	5.31	9.978	7.43	.82	5.26	9.978
3.08	.34	5.17	9.978	7.61	.84	4.90	9.979
3.26	.36	5.03	9.979	7.79	.86	4.59	9.981
3.44	.38	5.13	9.978	7.98	.88	4.27	9.982
3.63	.4	5.47	9.977	8.16	.9	3.86	9.984
3.81	.42	5.98	9.975	8.34	.92	3.38	9.986
3.99	.44	6.28	9.974	8.52	.94	2.84	9.988
4.17	.46	6.62	9.972	8.70	.96	2.30	9.990
4.35	.48	6.71	9.972	8.88	.98	1.61	9.993
4.53	.5	7.17	9.970	9.06	1.0	0.	1.0E+0

P = 10 Atm

t = 1.18 Sec

z/D₀ = 10.39

Re ~ 27,600

SF₆/N₂

D₀ = 0.5 In.

D/D₀ = 5.12

3/4 D Wake Cut

r (in.)	r/r _{edge}	C _M	ρ/ρ _∞	r (in.)	r/r _{edge}	C _M	ρ/ρ _∞
1.75E-2	.02	4.28E-4	9.982E-1	4.54E-1	.52	6.54E-4	9.973E-1
3.49	.04	4.15	9.983	4.72	.54	6.47	9.973
5.24	.06	1.96	9.992	4.89	.56	6.38	9.973
6.99	.08	6.20	9.974	5.07	.58	6.35	9.973
8.74	.1	6.31	9.973	5.24	.6	6.09	9.974
1.05E-1	.12	6.41	9.973	5.42	.62	5.96	9.975
1.22	.14	6.67	9.972	5.59	.64	5.69	9.976
1.40	.16	6.75	9.972	5.77	.66	5.56	9.977
1.57	.18	7.16	9.970	5.94	.68	5.42	9.977
1.75	.2	7.78	9.967	6.12	.7	5.29	9.978
1.92	.22	9.09	9.962	6.29	.72	5.26	9.978
2.10	.24	6.61	9.972	6.46	.74	5.16	9.978
2.27	.26	6.74	9.972	6.64	.76	5.03	9.979
2.45	.28	7.10	9.970	6.81	.78	4.88	9.980
2.62	.3	7.49	9.969	6.99	.8	4.72	9.980
2.80	.32	8.24	9.965	7.16	.82	4.47	9.981
2.97	.34	8.50	9.964	7.34	.84	4.16	9.983
3.14	.36	8.67	9.964	7.51	.86	3.88	9.984
3.32	.38	8.39	9.965	7.69	.88	3.60	9.985
3.49	.4	8.00	9.966	7.86	.9	3.26	9.986
3.67	.42	7.70	9.968	8.04	.92	2.89	9.988
3.84	.44	7.25	9.970	8.21	.94	2.48	9.990
4.02	.46	7.16	9.970	8.39	.96	2.00	9.992
4.19	.48	6.91	9.971	8.56	.98	1.41	9.994
4.37	.5	6.71	9.972	8.74	1.0	0.	1.0E+0

$P = 10 \text{ Atm}$ $t = 2.5 \text{ Sec}$ $z/D_0 = 16.9$ $Re \sim 27,600$
 SF_6/N_2 $D_0 = 0.5 \text{ In.}$ $D/D_0 = 7.26$ Central Cut

$r \text{ (in.)}$	r/r_{edge}	C_M	ρ/ρ_∞	$r \text{ (in.)}$	r/r_{edge}	C_M	ρ/ρ_∞
3.58E-2	.02	-1.48E-3	1.006E+0	9.32E-1	.52	1.66E-3	9.931E-1
7.17	.04	-1.19	1.005	9.68	.54	2.07	9.914
1.08E-1	.06	-9.94E-4	1.004	1.004E+0	.56	2.08	9.913
1.43	.08	-7.45	1.003	1.040	.58	2.03	9.915
1.79	.1	-5.14	1.002	1.075	.6	1.97	9.917
2.15	.12	-3.24	1.001	1.111	.62	1.93	9.919
2.51	.14	-1.92	1.001	1.147	.64	1.88	9.921
2.87	.16	-5.14E-5	1.000	1.183	.66	1.83	9.924
3.23	.18	5.48E-6	1.000	1.219	.68	1.76	9.926
3.58	.2	1.20E-5	1.000	1.255	.7	1.71	9.929
3.94	.22	5.68	9.998E-1	1.291	.72	1.62	9.932
4.30	.24	1.17E-4	9.995	1.326	.74	1.46	9.939
4.66	.26	1.58	9.993	1.362	.76	1.28	9.946
5.02	.28	1.96	9.992	1.398	.78	1.14	9.952
5.38	.3	2.64	9.989	1.434	.8	1.05	9.956
5.74	.32	3.06	9.987	1.470	.82	9.67E-4	9.959
6.09	.34	3.38	9.986	1.506	.84	8.67	9.964
6.45	.36	3.39	9.986	1.542	.86	7.86	9.967
6.81	.38	3.07	9.987	1.577	.88	7.11	9.970
7.17	.4	3.94	9.983	1.613	.9	6.40	9.973
7.53	.42	5.47	9.977	1.649	.92	5.67	9.976
7.29	.44	6.94	9.971	1.685	.94	4.87	9.980
8.25	.46	8.71	9.963	1.721	.96	3.94	9.983
8.60	.48	1.03E-3	9.957	1.757	.98	2.76	9.988
8.96	.5	1.22	9.949	1.792	1.0	0.	1.0E+1